Multidimensional Modulation Formats for Optical Transmission Systems

vorgelegt von
Master of Science
Saleem Alreesh
geb. Homs, Syrien

Von der Fakultät IV – Elektrotechnik und Informatik
der TECHNISCHEN UNIVERSITÄT BERLIN
zur Erlangung des akademischen Grades

Doktor der Ingenieurwissenschaften
Dr.-Ing.

genehmigte Dissertation

Promotionsausschuss:

Vorsitzender:	Prof. Dr.-Ing. Giuseppe Caire
Gutachter:	Prof. Dr.-Ing. Hans-Joachim Grallert
Gutachter:	Prof. Dr.-Ing. Norbert Hanik
Gutachter:	Dr.-Ing. Henning Bülow

Tag der wissenschaftlichen Aussprache: 19.02.2018

Berlin 2018

Acknowledgment

First of all, I would like to express my sincere appreciation to my supervisor Prof. Hans-Joachim Grallert for the continuous encouragement and invaluable guidance throughout my Ph.D study.

My sincere thanks goes to my group leader Dr. Johannes Fischer at the Fraunhofer Heinrich-Hertz Institute (HHI) for his precious support and advice during these years. His knowledge and technical expertises have been always of great value for me. I will be always grateful for the trust he has given me during my work at HHI.

I wish to express my deep thanks and appreciation to Dr. Colja Schubert for his assistance and valuable opinions. It was a privilege for me to have had the chance to discuss with him different topics during the lunch breaks.

I would also like to extend my sincere gratitude to all of my former and present colleagues at HHI for their constant support during my work. In particular, Pablo Wilke-Berenguer, Felix Frey, Dr. Carsten Schmidt-Langhorst, Dr. Robert Elschner, Lutz Molle, Dr. Isaac Sackey, Robert Emmerich, Dirk-Daniel Groß, Dr. Christian Meuer, Dr. Markus Nölle and Dr. Thomas Richter. I am very glad and blessed to have met you all.

I wish to thank my great friends, Dr. Thomas W. O'Donnell and Andreas Koher for proof-reading parts of the dissertation.

I am also thankful to the Deutsche Forschungsgemeinschaft (DFG) for providing the financial support to conduct the necessary research for this dissertation.

Finally, I would like to dedicate these few words to my lovely son Rafi. You are indeed the greatest thing ever happened to me. I couldn't have come this far without seeing your smile every morning.

Saleem Alreesh
Berlin, August 2017

Abstract

The ever-increasing demand for bandwidth is constantly driving deployment of new strategies to enable the upgrading of current optical transmission systems. Therefore, next generation optical networks are required to be elastic and more efficiently utilize the available optical spectrum; this in turn increases spectral efficiency and overall network capacity. To this end, future optical transceivers need to be able to adapt the bit rate and reach in a flexible manner based on actual network demand. Moreover, the cost and complexity of these transceivers should be kept as low as possible for practical implementation. In this thesis, multidimensional (multi-D) optical modulation formats are studied as a promising approach to realize flexible and cost-efficient optical transceivers.

The first part of the thesis discusses the coding gain that can be obtained by designing a signal constellation based on a dense lattice of arbitrary dimension. In particular, four-dimensional (4-D) signal constellations are considered for coherent optical communication systems. Various optimized 4-D modulation formats are studied showing their potential coding gain advantage over conventional 2-D modulation formats. In addition, novel digital signal processing (DSP) algorithms for some 4-D modulation formats are proposed and tested by numerical simulation and in transmission experiments.

In the second part of the thesis, the advantages of combining advanced modulation formats and forward error correction (FEC) codes, so-called coded modulation, are explored. The idea of 2-D trellis coded modulation (TCM) is first reviewed. Afterwards, the benefits of extending the dimensionality to multi-D space are explained. Following this, different partitioning schemes for multi-D signal sets are reviewed, and from this the Multilevel coding (MLC) scheme is described in detail. Moreover, the principle of operation of the turbo TCM (TTCM) scheme is discussed as a means to enhance the coding gain and close the gap to the channel capacity.

The last part of the thesis presents two experimental realizations concerning multi-D modulation formats. In the first experimental study, an optimized 4-D modulation format, namely 128-SP-QAM, is implemented and tested in a Nyquist-wavelength division multiplexing (NWDM) system. The performance of 128-SP-QAM is first compared with PDM-16QAM in back-to-back (b2b) setup and after transmission. In addition, two different soft-decision (SD-) FEC codes are experimentally evaluated for the 128-SP-QAM modulation format.

In the second experiment, 4-D TCM based on PDM-*M*QAM formats are experimentally realized. The coding gain advantages of 4-D TCM over conventional PDM-*M*QAM are demonstrated in the b2b configuration and in WDM transmission system. In addition, the impact of burst error events, induced by the fiber nonlinearities, on the performance of 4-D TCM is experimentally analyzed. A multi-rate optical transceiver with a bitrate granularity of 25 Gb/s is realized by a single encoder/decoder structure. Furthermore, tolerance toward cycle-slip events is enabled by the rotational invariant feature of the 4-D TCM scheme. Moreover, the performance of 4-D TTCM schemes is experimentally evaluated and their superior coding gains over 4-D TCM are validated. Finally, the performance of 4-D TCM and TTCM is compared with standard PDM-*M*QAM formats in presence FEC codes. Here it is shown that 4-D TCM concatenated with a low complexity HD-FEC could be an alternative approach to SD-FE codes for complexity-performance tradeoff.

Zusammenfassung

Die stetig ansteigende Nachfrage für zusätzliche Übertragungsbandbreite drängt nach dem Einsatz neuer Strategien, die Erweiterungen existierender optischer Übertragungssysteme ermöglichen. An die kommende Generation optischer Netzwerke wird folglich der Anspruch von Elastizität und einer effizienteren Nutzung des verfügbaren Spektrums gestellt, was zu einer Erhöhung der Gesamtnetzwerkkapazität führt. Künftige optische Transceiver werden daher ihre Datenraten und Reichweiten flexibel an vorliegende Netzwerke anpassen müssen, wobei in deren Implementierungen ein besonderes Augenmerk auf geringe Kosten und Komplexität gerichtet werden muss. In dieser Dissertation werden mehrdimensionale (multi-dimensional, multi-D) optische Modulationsformate als vielversprechende Ansätze für flexible und kosteneffizienten Transceiverentwürfe untersucht.

Der erste Teil dieser Arbeit untersucht den Codierungsgewinn, der sich durch das Design von Signalkonstellationen auf dichten mehrdimensionalen Gittern ergibt. Besondere Beachtung finden hier vier dimensionale (4-D) Signalkonstellationen für kohärent optische Übertragungssysteme. Zuerst wird der Kodierungsgewinn einer Vielzahl von 4-D Modulationsformaten gegenüber herkömmlichen 2-D Modulationsformaten untersucht. Zusätzlich werden neue Algorithmen der digitalen Signalverarbeitung (digital signal processing, DSP) einiger 4-D Modulationsformate vorgeschlagen und sowohl numerisch, als auch experimentell getestet.

Im zweiten Teil dieser Arbeit werden die Vorteile von codierte Modulation, d.h. einer Kombination fortschrittlicher Modulationsformate mit Vorwärtsfehlerkorrektur (forward error correction, FEC) Codes, erforscht. Nach einer Einführung des Ansatzes von 2-D trellis codierter Modulation (TCM), werden die Vorteile der Erweiterung des Signalraums zu einem multi-D Raum erläutert. Es folgt eine Übersicht zu verschiedenen Partinionierungsschemata für multi-D Signalmengen, von aus denen Multilevel coding (MLC) im Detail diskutiert wird. Zusätzlich wird das Verfahren von turbo TCM (TTCM) als Mittel zur Verbesserung des Codiergewinns und somit zur Schließung der Lücke zur Kanalkapazität betrachtet.

Der letzte Teil der Arbeit präsentiert zwei experimentelle Realisierungen, die sich mit mutli-D Modulationsformaten beschäftigen. In der ersten experimentellen untersuchung wird ein optimiertes 4-D Modulationsformat namens 128-SP-QAM implementiert und in einem Nyquist Wellenlaengenmultiplex (Nyquist wavelength division multiplexing, NWDM) System getestet. Die Performanz von 128-SP-QAM wird zuerst mit PDM-16QAM in einem Rücken-an-Rücken (back-to-back, b2b) und nach einer optischen Übertragungsstrecke verglichen. Zusaetzlich werden zwei unterschiedliche soft-decision (SD-) FEC Codes experimentell für 128-SP-QAM evaluiert.

Das zweite Experiment beschäftigt sich mit der Realisierung von 4-D TCM, welches auf PDM-*M*QAM basiert. Der Vorteil im Codiergewinn von 4-D TCM über herkömmlichem PDM-*M*QAM werden in einer b2b Konfiguration und einer WDM Übertragung demonstriert. Der Einfluss durch Fasernichtlinearitäten hervorgerufenen, gebündelten Bitfehlerereignissen auf die Performanz von 4-D TCM wird zusätzlich experimentell untersucht. Es wird ein mehrratiger optischer Transceiver mit einer einzigen Codier-/Decodierstruktur, einer Bitraten Granularität von 25 Gb/s und einer Toleranz gegenüber Zyklusschlupfereignissen durch die Rotationsinvarianz des 4-D TCM Schemas vorgestellt. Zusätzlich wird die Performanz von 4-D TTCM experimentell evaluiert und deren Vorteil erhöhter Codiergewinne im Vergleich zu 4-D TCM validiert. Abschliessend wird die Performanz von 4-D TCM und TTCM mit den herkömmlichen PDM-*M*QAM Formaten mit FEC

Kodierung verglichen. Es wird gezeigt, dass das Zusammenspiel von 4-D TCM mit einer einfachen HD-FEC ein alternativer Ansatz zu SD-FEC Codes darstellen.

Table of Contents

CHAPTER 1

Introduction

An important observation was made by Graham Bell in 1880, when he recognized that some characteristics of a light signal can be modulated to convey information. With his invention, the so-called Photophone, he demonstrated that a voice signal can be transmitted through the variation of sunlight intensity. This has formed a basic model for unguided optical transmission systems, using light as a carrier of information and the atmosphere as a transmission channel.

In 1917, Albert Einstein found a quantum mechanical explanation for the stimulated emission phenomena [1], that later formed the theoretical basis for discovery of the laser. The first laser, based on a ruby crystal, was introduced in 1960 [2]. Thereafter, a semiconductor laser based on gallium arsenide (GaAs) was developed in 1962 [3]. The invention of the laser was the first step in the progress of constructing lightwave transmission systems. The second breakthrough was achieved in 1966, when glass fiber was introduced as an efficient medium for guiding a light beam [4]. Attention was then directed to fabricating a fiber with low loss. As a result, much effort was expended a number of research groups, enabling a reduction of fiber losses from more than1000 dB/km in 1966 to only 0.2 dB/km in 1979 [5].

The availability of a narrowband optical source, i.e. a laser, and a practical optical transmission channel, i.e. a low-loss fiber, led to an increasing interest in developing a fiber optical transmission system. A series of laboratory experiments and field trials were carried out showing the potential advantages of lightwave systems over coaxial systems. The first commercial deployment of a lightwave system was accomplished in 1980, operating at a bit rate of 45 Mb/s. Later on, fiber cables across the Atlantic and Pacific Oceans were installed and operated at a maximum bit rate of 280 Mb/s [6, 7]. An important advancement was achieved by the invention of the erbium-doped fiber amplifier (EDFA) together with wavelength division multiplexing (WDM) technology. This has allowed the independent modulation of many wavelengths, sent over a single fiber link. EDFAs are then used to compensate for fiber losses and amplify all transmitted wavelengths simultaneously. This has led to a significant boost of the optical channel capacity.

Further major progress in the development of lightwave systems came with the advent of coherent detection techniques in the mid-2000s, which made full use of the optical field and allowed modulation of information in all available degrees of freedom, i.e. amplitude, phase and polarization. Since 2010, optical coherent transmission systems operating at a bit rate of 100 Gb/s per channel are commercially available [9].

Nowadays, optical transmission systems carry out the vast majority of global data traffic and millions of kilometers of optical fiber have already been deployed worldwide. The demand for bandwidth continues to increase exponentially every year [10], according to which, the available data rate per wavelength channel needs to be extended beyond 100 Gb/s (e.g. 400 Gb/s or 1 Tb/s).

Fig. 1.1 outlines some recent capacity × distance experimental records which were reported in the last few years [11-29]. It can be observed that research laboratories were able to enhance the capacity × distance product every year by employing sophisticated digital signal processing, advanced modulation formats and enhanced forward error correction (FEC) codes. Nevertheless, the complexity and the power consumption of such systems are still relatively high. In the

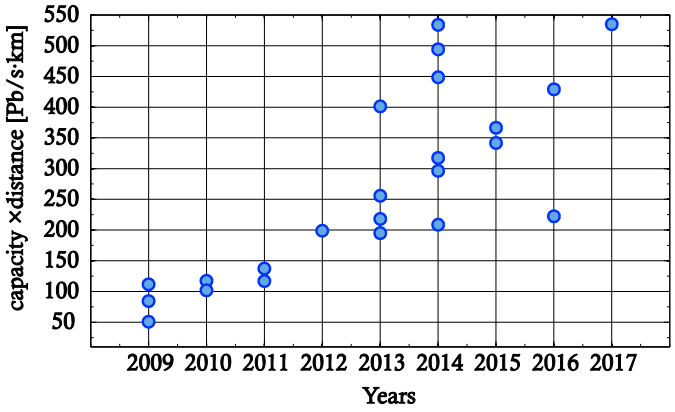

Fig. 1.1: Recently demonstrated capacity × distance experimental records.

meantime, cost-efficient, low complexity approaches are much needed to provide practical solutions taking into account current technological limitations. Research efforts in the optical community seek practical approaches to cope with growing data traffic, and several have already been proposed [30]. An interesting option is to upgrade the present 50 GHz fixed-grid network by moving to the flexible grid paradigm of elastic optical networks (EONs) [30, 31]. To this end, bandwidth variable transceivers (BVT) are considered key elements for the future EON. These types of transceivers should support various modulation formats with different spectral efficiencies; thus they should have the ability to adapt the bit rate and the reach based on the actual traffic demand [32]. This would allow optimum utilization of the available optical spectrum and enhance the overall system capacity.

Realizing the aforesaid requirements for future EON is the objective of this thesis. In this context, multi-dimensional (multi-D) modulation formats will be discussed as a viable option to realize flexible and cost-efficient transceivers.

The thesis is organized as follows: Chapter 2 reviews the main components of an optical transmission system. It starts by describing the optical transmitter and its basic elements. Then, it gives a short overview of the optical fiber link. Following, it discusses the coherent detection technique and the digital signal processing (DSP) unit. Chapter 3 introduces the basics of lattices and discusses the coding gain that can be realized by constructing signal constellation based on dense lattices. Later, it introduces some optimized signal constellations in the 4-D space and describes some related DSP algorithms. Chapter 4 starts with introducing the fundamentals of trellis coded modulation (TCM). Then, it focuses on the multi-D TCM and analyses the different partitioning schemes. Afterwards, it demonstrates the concept of Turbo TCM and reviews its encoder and decoder blocks. In Chapter 5, two experimental works are described. The first experiment presents an investigation of an interesting 4-D modulation format in presence of two soft-decision FEC codes. The second experiment introduces an evaluation of 4-D TCM and TTCM for optical transmission system. Chapter 6 concludes the main findings of this thesis and presents a short future outlook.

CHAPTER 2

Digital Coherent Optical Communication Systems

This chapter gives a general overview of optical communication systems. It explains the main elements of optical transceivers and briefly discusses the optical fiber channel.

A basic optical communication system consists of three building blocks: the transmitter, the channel and the receiver. At the transmitter side, the information bits are generated and modulated into an optical carrier to make it suitable for transmission over the channel. At the other side of the channel, the receiver is used to demodulate the incoming optical signal and extract the information bits. In the subsequent sections, the fundamental parts of an optical communication system will be discussed.

2.1 The Optical Transmitter

The main purpose of an optical transmitter is to prepare the information signal and put it in an appropriate form for transmission over the optical channel. To this end, modern optical transmitters are composed of three functional blocks, the first is the DSP unit, which operates in the electrical domain, the second is the modulator unit, which runs in the electro-optic domain, and the third is the digital to analogue converter (DAC) unit, which works like an interface that takes the digital output signal from the DSP unit, transfers it into analog form, and feeds it to the modulator unit. It is worth mentioning that in the modern optical transmitters the DAC unit and the DSP unit are actually integrated in a single ship.

In the DSP unit, the information bit sequence is first processed by a channel encoder, which introduces some controlled redundancy that will then be exploited to correct wrongly detected information bits after transmission over a noisy channel. The encoded bit stream is then mapped into a sequence of symbols employing a proper modulation scheme. Next, a custom training sequence is inserted, which can be used to estimate the channel transfer function and compensate for some channel impairments at the receiver. As a next step, pulse shaping can be applied in digital domain followed by a predistortion block. The latter is used to compensate for imperfect transfer characteristics of the transmitter components. It should be emphasized that different structures of the DSP unit are also possible depending on the system scenario. However, the aforementioned structure is one that has been adopted for the system experiments presented in Chapter 5.

The output signal samples from the DSP unit are then passed into the DAC, which generates the electrical signal waveforms. These waveforms are amplified by modulator driver amplifiers before being used to drive the modulator unit. The modulator unit consists of two main components, the optical modulator and the optical source. The optical modulator is used to impress the electrical signal waveform onto an optical carrier which is generated by the optical source.

In the following subsections, only some transmitter parts, which are needed to understand the subsequent chapters, will be described. Section 2.1.1 introduces the principle digital modulation schemes, Section 2.1.2 presents a brief discussion of optical carrier source and Section 2.1.3 describes the optical modulator.

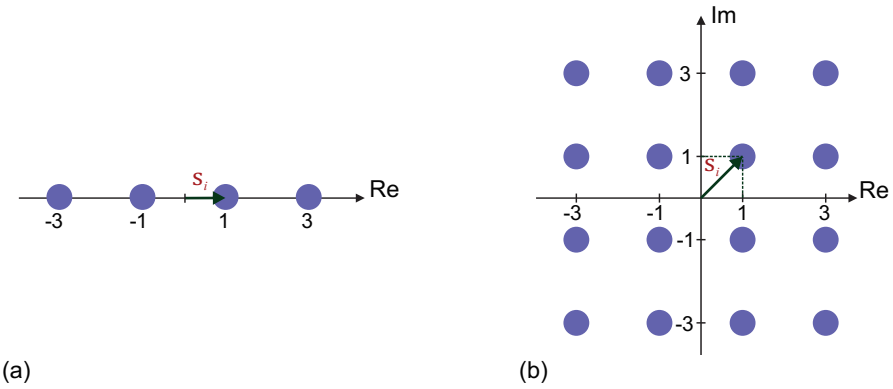

Fig. 2.1: Geometrical representation of (a) 4-ASK and (b) 16-QAM

2.1.1 Digital Modulation Schemes

In digital modulation schemes, the information source emits information bits with rate R_b, called the bit rate, where $R_b = 1/T_b$ and T_b is the bit duration. The information bit sequence is divided into subsequences, each of which contains η bits. Each of these blocks is used to select one symbol $\boldsymbol{s}_i$ from a finite alphabet set Ω, denoted as *signal constellation*, where $1 < i < M$ and $M = 2^\eta$ is the number of different symbols in Ω. The symbol duration T_s is then calculated by $T_s = \eta \cdot T_b$. Accordingly, we can define the symbol rate $R_s = 1/T_s$ as the number of symbols transmitted per second, which has units of symbols per second or baud (Bd).

In general, the symbol $\boldsymbol{s}_i$ is an N-dimensional (N-D) vector, which can be represented by a set of coefficients $\{s_{ik}, 1 \leq k \leq N\}$. Each symbol $\boldsymbol{s}_i$ can thus be written as $\boldsymbol{s}_i = [s_{i1}, s_{i2}, \dots, s_{iN}]^T$, where T stands for vector transpose. Accordingly, each block of η information bits is mapped to an N-tuple of coefficients, such that the information is encoded by these coefficients.

It is beneficial now to visualize the set of symbols Ω in an N-D Euclidian space. As an example of a simple 1-D modulation scheme we take the M-ary amplitude shift keying (M-ASK), in which the symbol is defined by a single coefficient. Here, each set of information bits is assigned to a respective amplitude level. For instance, assume $M = 4$, then there are four different amplitude levels. Fig. 2.1 (a) shows the geometric representation of 4-ASK in the 1-D Euclidian space.

For N=2, each symbol is described by two coefficients. A common 2-D modulation scheme is the M-ary quadrature amplitude modulation (M-QAM). The signal constellation for M=16 in the 2-D Euclidian space is depicted in Fig. 2.1 (b). Here, the two axes are labeled with *Re* and *Im*, i.e. the real and imaginary part of the carrier wave, respectively. This notation will be discussed in section 2.1.3. The 16-QAM modulation scheme can be seen as a combination of two 4-ASK, one in each in dimension, such that each of two signal coefficients takes one of four different values. As a result, 16 possible 2-tuples symbols are obtained.

Of course, the choice of the set of coefficients that constitutes the signal constellation is not arbitrary. Actually, there are design parameters that should be considered to construct a good signal constellation in a given dimension, N. This will be discussed in detail in Chapter 3.

Now, it is important to define a typical figure of merit for a modulation scheme, which is called the spectral efficiency (SE). It is defined as the number of transmitted bits per 2-D symbol [33, p.219]:

$$\mathrm{SE} = \frac{log_2 M}{N/2} \tag{2-1}$$

Equation (2-1) assumes a pure uncoded scenario and that all symbols are equally probable.
The next step is to impress the information symbols on the optical carrier, which will be then transmitted over the channel. To this end, a technique called *modulation* is employed, in which one or more characteristics of the carrier wave will be adapted in accordance with the information symbols. This technique will be discussed in the next sections.

2.1.2 Optical Carrier Source

As described in the previous section, the generated digital symbols need to be converted into a waveform that is suitable for propagating over the channel. To that end, many communication systems employ a carrier wave to convey the information. The carrier wave operates in a frequency range higher than the frequency range of the information signal. This is considered a fundamental step for many communication systems in order to meet the requirements imposed by the channel or by some hardware specifications.
For optical communication, the carrier wave is light, which can be generated by two main types of optical sources, namely laser diodes (LD) and light-emitting diodes (LED). These are designed to radiate light in a specific frequency range where the optical fiber has some desirable properties, e.g. low loss.
The optical source emits light within a range of frequencies, called the source linewidth. The broader the linewidth, the less coherent is the radiation. Non-coherent light is a consequence of the spontaneous emission phenomena, which manifests itself as a phase fluctuation (phase noise) $\Delta\varphi$ in the generated lightwave. The variance of the phase fluctuation $\sigma_{\Delta\varphi}^2$ is related to the linewidth of the source $\Delta\nu$ within the time interval Δt as follows [34, p.17]:

$$\sigma_{\Delta\varphi}^2 = 2\pi \cdot \Delta\nu \cdot |\Delta t| \tag{2-2}$$

It is apparent from equation (2-2) that phase changes become more severe as the linewidth of the source increases. Accordingly, if the receiver is sensitive to the phase of the incoming signal, the phase fluctuation of the optical source will become a main source of noise and thus performance degradation. This will become evident when we discuss coherent detection in Section 2.3.1.

2.1.3 Optical Modulator

The optical modulators are devices used to transform the electrical signal waveform into the optical domain in such a way that the information is encoded in some characteristics of the optical carrier, i.e. the light wave.
Light can be described an electromagnetic wave. Assuming a linearly polarized light wave propagating in the z-direction, then the electrical field component of this wave can be expressed as [35, p. 30]:

$$E(x,y,z,t) = \left\{F(x,y) \cdot A(z,t) \cdot e^{(\omega_c t - \beta_0 z)}\right\} \cdot \vec{p}(z,t) \tag{2-3}$$

In equation (2-3), x, y and z represent the Cartesian coordinates and t denotes the time. $F(x,y)$ is the transverse distribution of the field and $A(z,t) = \sqrt{P} \cdot a(z,t) \cdot e^{j\varphi(z,t)}$ is the complex envelop of the field, where P refers to the power of the field. Furthermore, $a(z,t)$ and $\varphi(z,t)$ represent the time and location dependent amplitude and phase, respectively. [34, p.143]. The parameteres ω_c and β_0 specify the angular frequency and the propagation constant, respectively and finally, $\vec{p}(z,t)$ refers to the polarization unit vector.

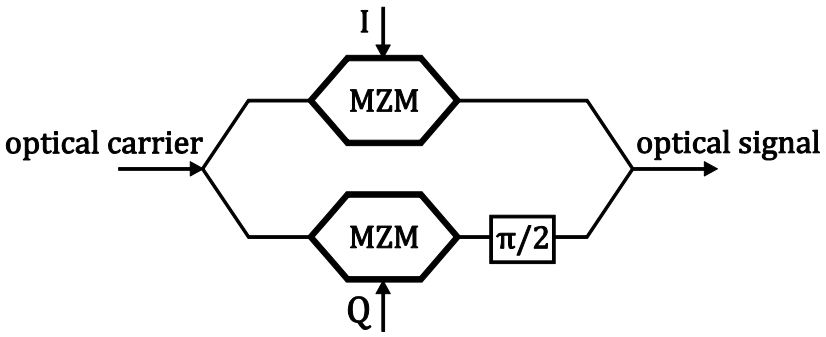

Fig. 2.2: Schematic of an optical IQ modulator

By inspection of equation (2-3) at the transmitter side (i.e. z= 0), it can be seen that there are different characteristics of the optical field which can be exploited to convey the information signal. These characteristics are:

- The amplitude $a(t)$: In this case the amplitude of the optical field varies in accordance with the information symbols such that the information to be transmitted is carried by the amplitude variation. This type of modulation is referred to as amplitude shift keying (ASK).
- The phase $\varphi(t)$: Here, the phase of the optical field is modulated by the information symbols such that a distinct phase level is assigned to each information symbol. This kind of modulation is called phase shift keying (PSK). A related parameter is the frequency of the optical carrier, w_c, which can also be made to change in accordance to the information signal; this is so called frequency shift keying (FSK). However, FSK can be treated as a PSK format in which the phase of the carrier varies during the bit duration [36, p.485].
- The polarization $\vec{p}(t)$: an optical field has two orthogonal polarization components which can be used for transmission. These two components can be used to carry independent information. Such an approach is referred to as polarization division multiplexing (PDM). Alternatively, the information can be encoded into the different polarization states. Such a scheme is called polarization shift keying (PolSK), which will be discussed in Chapter 3.

It should be noted that, one or any combination of the aforementioned carrier characteristics can be used to modulate the information signal. The modulated signal $s(t)$ on each polarization component can be mathematically expressed as:

$$s(t) = Re\left[\tilde{s}(t)e^{j\omega_c t}\right] = s_I(t)\cos(\omega_c t) - s_Q(t)\sin(\omega_c t) \tag{2-4}$$

Here, $\tilde{s}(t)$ represents the complex envelope of the baseband signal where $s_I(t)$ and $s_Q(t)$, (in short, I and Q) are the in-phase (real) and quadrature (imaginary) components of $\tilde{s}(t)$, Thus, the complex envelope $\tilde{s}(t)$ can be written as:

$$\tilde{s}(t) = s_I(t) + js_Q(t) \tag{2-5}$$

It should be noted that both terms (i.e., I and Q) can be employed to carry information independently. Since there are two polarization components of an optical carrier, there are in total four degrees of freedom that are available for data transmission.

An electro-optic in-phase and quadrature (I/Q-) modulator is used to independently modulate the I and Q components of the optical carrier (see Fig. 2.2 for a schematic representation). The device is

composed of two arms, each of which contains a Mach-Zehnder modulator (MZM) used to modulate the amplitude of the carrier. In addition, an optical phase shifter is employed in one arm to introduce relative phase shift of $\pi/2$ between the two arms. As a result, the two signals become orthogonal and can be combined to generate arbitrary modulation formats in the IQ-space (i.e. in two dimensions). The approach can be extended to modulate four degrees of freedom simultaneously, i.e. the I and Q components of the two states of polarization. This requires two I/Q-modulators, with one for each polarization component. Nowadays, integrated dual polarization (DP) I/Q modulators are commercially available [37].

2.2 The Optical Fiber Link

The optical fiber represents the transmission channel for optical communication systems. Fiber is a dielectric waveguide, which is a lossy, dispersive and nonlinear medium. A lossy property means that the optical signal propagating inside a fiber will be attenuated, (i.e. its intensity will be reduced gradually with the transmission distance). As a result, the transmission reach is limited by the power that can be transferred to the receiver. Therefore, attenuation is considered a major design parameter for optical fibers and significant effort has been made to fabricate low-loss fibers [38]. Fiber attenuation becomes a critical limiting factor for long transmission links as the intensity can drop to a level where reliable detection is no longer possible. It is apparent that it is mandatory to compensate for such losses in-line to extend the transmission distance. In early lightwave systems this was accomplished by using optoelectronic repeaters, so-called *regenerators*. Such a device is composed of an optical receiver followed by a transmitter. It detects the attenuated and distorted optical signal from the fiber and converts it to the electrical domain, where the signal amplitude and shape are reconstructed. Afterwards, the regenerated digital signal is converted back to the optical domain before it is injected into the fiber. Beginning in the 1990s, regenerators were rapidly replaced by optical amplifiers [39, 40]. In comparison to regenerators, optical amplifiers have lower cost, less power consumption and most importantly, boost the power of many wavelengths simultaneously. For these reasons, optical amplifiers were considered a key component for wavelength division multiplexing (WDM) optical transmission systems. In some special ultra-long distance scenarios, a combination of many optical amplifiers with only few regenerators can be employed.

Another class of important fiber properties are dispersive effects. This includes mainly chromatic dispersion (CD) and polarization mode dispersion (PMD). Basically, dispersion phenomena lead to a broadening of the optical pulse with distance travelled. Thus, adjacent optical pulses will eventually overlap and become indistinguishable. Moreover, PMD causes random alterations of the polarization state of the propagating optical wave, which is an issue for coherent receivers as will be discussed in Section 2.3.1. Fortunately, nowadays CD and PMD can be effectively compensated for by using a digital linear equalizer at the receiver [41, 42].

Other impairments result from the nonlinear properties of the optical fiber. These effects can be classified, based on their origins, into two types: elastic and inelastic. In elastic effects, also referred to as Kerr-nonlinearity, the refractive index of the fiber varies with the applied optical power. This results in some major nonlinear effects including: Self-phase modulation (SPM), Cross-phase Modulation (XPM) and Four-wave mixing (FWM). In a different manner, inelastic effects are induced by stimulated inelastic scattering, which is responsible for two effects, i.e. stimulated Brillouin scattering (SBS) and stimulated Raman scattering (SRS) [43, 64-65]. Nonlinearity compensation (NLC) technique is an active research topic in optical community, and

major efforts are being directed toward reducing the complexity of such techniques to make them more practical [44]. Moreover, it was suggested in [45, 46] that nonlinear impairments in a dispersion uncompensated fiber link can be approximated with Gaussian noise. Accordingly, the fiber link can be modeled as an additive white Gaussian noise (AWGN) channel in the simplest scenario.

2.3 The Optical Receiver

The optical communication systems can be classified into two categories based on the modulator/demodulator techniques. In the first category, electrical data is directly modulated in the intensity of the optical carrier at the transmitter. Then, an optical detector is used to convert the incident light intensity into electrical current at the receiver; such a system is referred to as *intensity modulation with direct detection* (IM/DD) [47]. On the other hand, the second category is called *coherent detection*, which detects the optical field rather than the optical intensity. Here, an external modulator is usually required at the transmitter and a coherent detection technique is employed at the receiver.

One of the important advantages of the coherent detection over the IM/DD technique is the improved receiver sensitivity However, this advantage becomes insignificant in the presence of EDFAs chain. In addition, the realization of systems based on coherent detection imposes some technical complications with the hardware. Therefore, the vast majority of early deployed optical transmission systems were based on IM/DD technique. Nevertheless, the upward progress in high speed digital signal processing (DSP) integrated circuits has paved the way for increased interest in coherent detection since the mid-2000´s [48, 49]. The motivation behind this was the benefits that can be gained by employing a coherent detection method, which includes: (1) the possibility to extract the amplitude and phase information in the two states of polarization of the received optical field, opening the door for advanced high order modulation formats to be applied in optical communication systems. (2) The phase of the optical carrier can be tracked using DSP functions, which relaxes the hardware requirement for the coherent receiver. (3) Many fiber transmission impairments, such as chromatic dispersion (CD) and polarization mode dispersion (PMD), can be compensated for at the receiver, in the electrical domain using a DSP core [50, 51].

2.3.1 Coherent Detection Technique

The schematic representation of a coherent receiver is depicted in Fig. 2.3, its principle of operation is based on the idea of mixing the received optical wave $E_s(t)$ with the light of a local-oscillator (LO) laser $E_{LO}(t)$ using a 3-dB optical coupler. The output signals from the two ports of the coupler are then detected by a balanced detector (BD), which consists of two photodetectors [52]. Thereafter, the resultant currents from the two ports, $I_1(t)$ and $I_2(t)$, are subtracted to give the

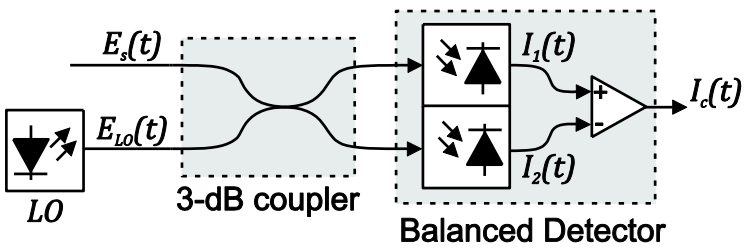

Fig. 2.3: Schematic diagram of coherent receiver

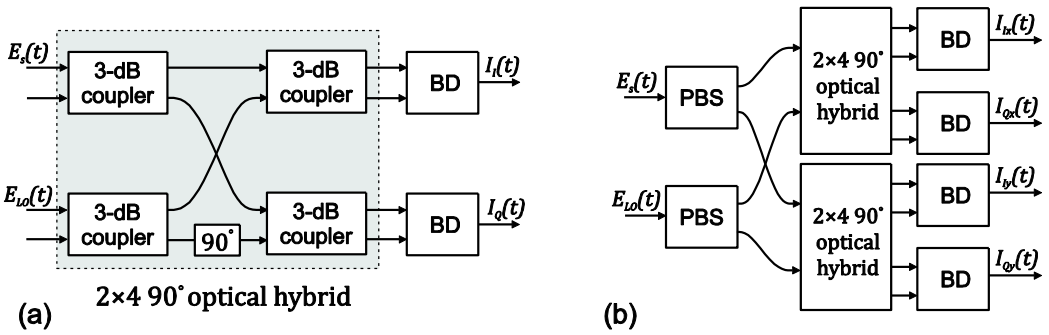

Fig. 2.4: Schematic diagram of (a) the phase-diversity receiver and (b) the polarization- and phase-diversity receiver

output current $I(t)$. Under the assumption that both the signal and LO are identically polarized, the current $I_c(t)$ can be expressed as [53]:

$$I_c(t) = I_1(t) - I_2(t) = 2R\sqrt{P_s(t)P_{LO}} \cdot cos\big(w_{IF}t + \phi_s(t) + \phi_n(t)\big) \tag{2-6}$$

Where R is the responsivity of the photodiode and $w_{IF} = |w_s - w_{LO}|$ is the intermediate frequency (IF), which is the angular frequency offset between the signal and LO. Moreover, $P_s(t)$ and P_{Lo} represent the power of the signal and LO respectively. Note that while P_{Lo} is constant, $P_s(t)$ can be time dependent in the case of amplitude modulation formats. $\phi_s(t)$, the signal phase modulation, is the difference between the phase of the received signal, $\phi_{sig}(t)$, and the phase noise of the transmitter, $\phi_{sn}(t)$. That is, $\phi_s(t) = \phi_{sig}(t) - \phi_{sn}(t)$. Finally, $\phi_n(t) = \phi_{sn}(t) - \phi_{LO}(t)$ represents the combined phase noise where $\phi_{LO}(t)$ refers to the LO phase.

In short, there are two distinct coherent detection methods that can be used, namely *heterodyne* and *homodyne* detection [54].

In the heterodyne detection, the frequencies of the optical carrier and the LO are selected to be different such that the intermediate frequency (IF), w_{IF}, is larger than the bandwidth of the modulated signal. In this way, the incoming optical signal is down-converted to an IF signal [53]. On the other hand, the frequencies of the optical carrier and the LO can be chosen to be identical, for homodyne detection (i.e. $w_{IF} = 0$). Hence, the baseband signal is directly recovered. It can be readily seen in equation (2-6) that the amplitude of output photocurrent $I_c(t)$ depends on w_{IF} and $\phi_n(t)$. Therefore, both parameters should be tracked in order to restore the amplitude and the phase of the modulated signal. The main advantage of heterodyne detection is that frequency and phase locking is much simpler to implement in hardware as compared to the homodyne case. Nevertheless, thanks to DSP technology, it is possible to estimate the frequency offset and the phase noise in the digital domain by means of a DSP unit. Obviously, homodyne detection would then be the preferred option since it requires smaller electrical bandwidth at the receiver [55].

It should be noted that in the context of optical communication, the coherent detection technique is commonly referred to as *intradyne* detection [56]. In this kind of system, a frequency mismatch between the transmitter and LO lasers is permitted. However, this frequency difference should be much smaller than the signal bandwidth [54] and it will be compensated by a DSP unit after detection [51].

By inspection of equation (2-6), it is evident that the phase noise fluctuation leads to variations in the current amplitude and thus to sensitivity degradation [36, p.498]. Therefore, it would be beneficial to find a scheme which enables us to recover the signal amplitude independently from

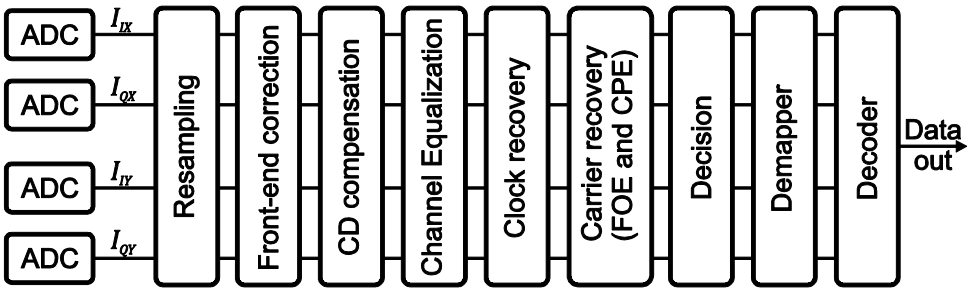

Fig. 2.5: A structure of a conventional DSP unit at the receiver side.

phase noise. In addition, it is apparent that only the inphase component can be detected at a time. To overcome these limitations, a scheme called *phase-diversity* was suggested [57]. It allows the detection of both the inphase and quadrature components of the received optical signal simultaneously and allows extraction of the signal amplitude independent of the phase noise.

One possible realization of the phase-diversity homodyne receiver is depicted in Fig. 2.4 (a). The main component in such a receiver is the 2×4 90° optical hybrid. It consists of four 3-dB couplers and a 90° phase shift. Note that there are other possible structures for this component [58]. It is used to combine the optical lightwaves of the incoming signal and the LO, where a 90° phase shift is introduced to allow separate detection of the inphase and quadrature components of the received signal [58]. The four outputs of the 2×4 90° optical hybrid are then detected by two balanced detectors. The resultant photocurrents, $I_I(t)$ and $I_Q(t)$, represent the in-phase (real) and quadrature (imaginary) component of the complex optical signal, respectively. They can be expressed as [53]:

$$\begin{aligned} I_I(t) &= R\sqrt{P_s(t)P_{LO}} \cdot cos\left(\phi_{sig}(t) - \phi_{LO}(t)\right) \\ I_Q(t) &= R\sqrt{P_s(t)P_{LO}} \cdot sin\left(\phi_{sig}(t) - \phi_{LO}(t)\right) \end{aligned} \tag{2-7}$$

Assuming a perfect IQ balance (i.e., an exactly 90° phase shift between the inphase and quadrature components), the two output currents in equation (2-7) can be squared and added. Accordingly, the amplitude of the optical signal can be detected independent of phase fluctuations [36, p. 498-499].

Up to this point, it was assumed that the state of polarization (SOP) of the incoming optical signal is perfectly aligned with the LO. However, in practice, the SOP of the optical wave travelling along a fibre changes randomly because of the fiber birefringence phenomena [35, 11-12]. This leads to a mismatch problem between the SOP of the signal and LO. As a consequence, the performance of the coherent receiver will degrade since the amplitude of the photocurrents will be affected by polarization fluctuations. Therefore, a mechanism should be introduced to make the receiver insensitive to the SOP of the incoming signal [36, 502-504]. The most popular scheme to handle this limitation is to employ a *polarization-diversity* technique [59].

A fruitful approach to implementing an optical coherent receiver is to combine the two techniques, i.e. polarization- and phase-diversity [60]. In this way, the complex amplitude of the two orthogonal polarizations of the optical signal can be recovered at the receiver. A schematic representation of such a receiver is depicted in Fig. 2.4 (b), in which two polarization beam splitters (PBS) are used to split the incoming and the LO signal into their linear polarization components (i.e., their x- and y- polarizations). Each polarization component is then processed separately by a phase-diversity receiver. This generates the inphase and quadrature photocurrents of the x- and y-polarization at the output.

2.4 Digital signal processing

With the availability of high speed integrated digital circuits, it is possible to perform many functions at the receiver side in the digital domain, such as phase and polarization tracking for coherent detection. This has eliminated the need for complex optical hardware implementation, such as an optical phase-locked loop (OPLL) circuit. Moreover, it has enabled development of DSP algorithms to mitigate various fiber impairments in a very effective way.

As was discussed in Section 2.3.1, a phase- and polarization-diverse optical frontend can be employed to recover all information in the optical field (i.e., the four analog photocurrents I_{Ix}, I_{Qx}, I_{Iy} and I_{Qy}). Afterwards, an analog to digital converter (ADC) unit is used to convert these electrical current into the digital domain. Following this, the digital samples are fed into a DSP unit, in which many algorithms are performed aiming to recover the information data from the distorted received samples.

Fig. 2.5 shows the structure of a conventional DSP unit. The incoming digital signal is first oversampled into an appropriate sampling rate. Typically, it is twice the symbol rate. Following this, frontend correction is performed, which compensate for the non-ideal characteristics of the 90° optical hybrid, which in turn leads to imbalance between the I and Q components [61]. Subsequently, the accumulated CD along the fiber is estimated using one of the various available techniques [62, 63], and then compensated for using a digital equalizer, which is implemented either in the frequency domain or in the time domain [64]. The signal is then forwarded into a channel equalizer, which is used to track the random polarization rotation and to mitigate the PMD. After clock recovery, carrier recovery is carried out, which performs two tasks. The first is a frequency offset estimation (FOE), where the frequency offset between the incoming signal and the LO is estimated and compensated for. The second is a carrier phase estimation (CPE), where the phase noise of the transmitter and LO lasers are estimated and corrected. The recovered signal values are then fed into a decision unit, which decides the most likely transmitted symbols. After the decision is made, symbol-to-bit demapping is applied and the output bits are sent into hard-decision FEC decoder. Finally, an estimation of the transmitted information bits is produced at the output of the decoder. It should be noted, however, that for systems based on soft-decision FEC, it is necessary to provide the FEC decoder with soft metrics (i.e., bit likelihood or reliabilities). Such soft information is calculated based on the estimated signal after the carrier recovery unit.

The following subsections present a brief discussion of the two main functions of the DSP unit, namely the channel equalization and carrier phase estimation.

2.4.1 Channel Equalization

The digital coherent receiver enables compensation of linear transmission impairments, such as time varying polarization rotation and PMD in digital domain using an equalizer. The equalizer can be implemented either in the time-domain or in the frequency-domain. Furthermore, channel equalization can be performed either with the assistance of training sequences, referred to as data-aided (DA) equalization, or without training symbol, referred to as blind equalization.

The time-domain equalizer (TDE) is normally implemented using four digital finite impulse response (FIR) filters, which are configured in a butterfly structure. The taps weights of each FIR filter are updated using an appropriate adaptation algorithm, depending mainly on the employed modulation format.

A very common algorithm is the constant modulus algorithm (CMA), which was proposed for a 2-D QPSK format [65]. This algorithm was then widely studied and employed for the dual polarization case in optical communication systems [42, 66, 67]. The CMA tries to minimize the error signal between the equalizer output and a reference amplitude level. Hence, it is particularly suited for a QPSK signal which has a constant amplitude level. Nevertheless, it was also found that the CMA can be effectively applied for modulation formats with many amplitude levels (e.g., 16-QAM), but with suboptimal performance [68, 69]. Alternatively, a multiple modulus algorithm (MMA) [70-72] can be applied for modulation formats with non-constant modulus. MMA is based on minimizing the error signal between the received symbols and the closest modulus level.

Another important algorithm is the decision-directed least mean square (DD-LMS) [73], in which the equalizer output is fed into a decision unit. Following this, the error signal is computed as the difference between the equalizer output and the decided symbols positions. That means the algorithm is sensitive to the carrier phase fluctuation and it is maybe necessary to add a phase estimator unit within the equalizer loop to remove the phase noise and improve the stability of the algorithm [74]. Typically, a blind adaptive algorithm is used for pre-convergence before switching to DD mode.

It can be deduced from the discussion above that the principle of operation of the blind and DD adaptation algorithms are based on the modulation format used. However, flexible optical transceivers should be able to support various modulation formats. Accordingly, an equalization algorithm which works independently from the employed modulation format is of great interest. In this respect, DA equalization algorithms offer the possibility to perform channel equalization regardless of the utilized modulation format [75].

2.4.2 Carrier Phase Estimation

Phase noise associated with the transmitter and LO laser is considered as one of the main impairments in a coherent optical communication system. The origin of this noise comes from the spontaneous emissions phenomena within the laser, which leads to a random phase fluctuation and broadens the laser linewidth. The laser phase noise can be modeled as a Wiener process [76] with variance given by Equation (2-2). An example of a phase noise process with two different linewidths $\Delta\nu$=100 kHz and 1 MHz is presented in Fig. 2.6 (a). It can be clearly seen that the phase fluctuation becomes more severe as the linewidth increases.

The phase noise causes the transmitted signal points to rotate by an arbitrary phase. This is illustrated in Fig. 2.6 (b) for a 16-QAM constellation case. Therefore, a CPE algorithm is required to estimate the phase noise and recover the phase of the information signal, as shown in Fig. 2.6(c).

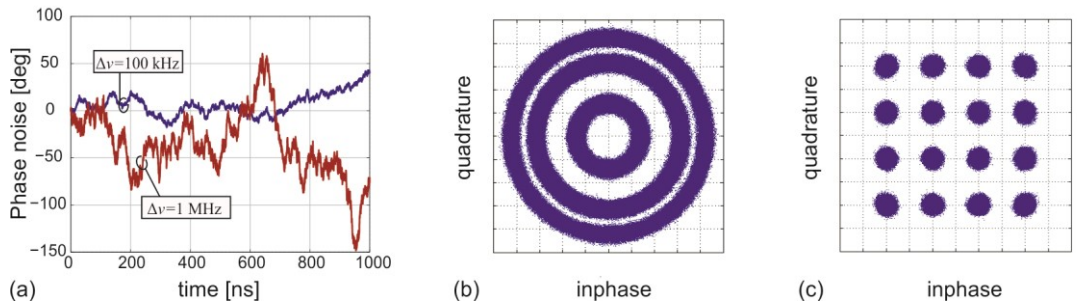

Fig. 2.6: (a) Numerical example of laser phase noise for two different linewidths (b) A simulation result showing the impact of phase noise on the 16-QAM constellation diagram (c) the recovered 16-QAM constellation diagram after applying a CPE algorithm

The Viterbi-Viterbi algorithm is a very common CPE scheme for M-PSK modulation format [77]; the phase noise is estimated by raising each block of received complex symbols to the M-th power; hence, the phase modulation information is removed. Following this, an averaging function is performed over the block of symbols to mitigate the influence of AWGN [76, 78]. The principle of the Viterbi-Viterbi algorithm can be also applied for 16-QAM format after performing a QPSK partitioning [79-81].

Another interesting CPE scheme is the blind phase search (BPS) algorithm [82], which works independently from the utilized modulation format. BPS is based on the idea of rotating each block of received symbols by some test angles. Then, for each test angle, the Euclidian distances (ED) between the rotated symbols and reference constellation points are calculated and the closest constellation points are found, that is, the points with minimum Euclidian distances (MEDs). Afterwards, the MEDs within each block are averaged to minimize the effect of AWGN. Upon doing so, an averaged MED is calculated for each test angle. Finally, the test angle corresponding to the minimum average MED is selected to derotate the symbols within the block in the process. Although BPS shows good performance for various modulation formats [75], its computational complexity is still very high, despite efforts made to make it more practical [83, 84]. The aforementioned CPE algorithms are liable to cycle slip (CS) events, especially for large phase noise and low optical signal-to-noise ratio (OSNR). The CS event causes the estimated carrier phase to slip by an integer multiple of the constellation symmetry angle (i.e. 90° for QPSK and QAM signals), which can lead to a long burst of errors.

One possible option to provide immunity against CS events is to employ differential encoding/decoding together with suitable bit-to-symbol mapping; however, this comes at the expense of some sensitivity degradation [76]. Another option is to send pilot symbols periodically to identify and correct the CS events, which results in an extra overhead [85, 86]. Another interesting option is to exploit the rotationally invariant feature of Trellis coded modulation [87, 88]; the later approach will be discussed in Chapter 4.

2.5 Forward Error Correction

In modern digital communication systems, it is required to reduce the number of decoding bit errors to a level at which the transmission is considered highly reliable. For a given SNR and

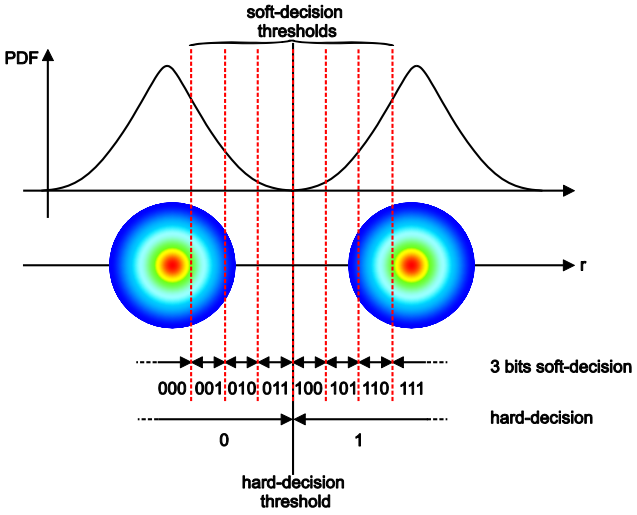

Fig. 2.7: Hard decision and 3-bits soft-decision for BPSK signal

channel bandwidth, Shannon [89] has shown that this is possible providing the information rate stays below a specific threshold called the channel capacity. To this end, forward error correction (FEC) codes are employed.

FEC codes are based on the concept of adding some redundancy to the information at the transmitter side which will then be exploited at the receiver side to correct errors detected after transmission. A commonly used figure of merit for FEC codes is the coding gain (CG), which is defined as the reduction in the required SNR (in dB), obtained by coding, to achieve a certain BER. However, the coded system uses an additional overhead for FEC compared with an uncoded system. Therefore, the net coding gain (NCG) is used to take into account the increased bandwidth of the coded system. The NCG can be calculated as $NCG = CG + 10log_{10}(R)$ where R is the code rate.

FEC codes can be classified based on the decoding scheme into two classes, hard-decision (HD) and soft-decision (SD) decoding. For the HD decoding, the demodulated signal is quantized to two levels, 0 and 1, before being forwarded to the HD decoder. On the other hand, for the SD decoding, the demodulator output is quantized into more than two levels. To illustrate this, Fig. 2.7 shows an example of HD and SD for BPSK signals, where three quantization bits are used for the SD case, resulting in eight distinct levels. The obvious advantage of SD decoding comes from the fact that the multilevel quantized signals carry more information than two level signals. This added information indicates the reliability of the decision. For example, the level 000 in Fig. 2.7 suggests that the coded bit with high reliability is zero, while the level 011 suggests that it is zero but with low reliability. This soft information can be exploited by the SD decoder to improve the decoding performance over the HD decoder. Typically, SD decoding offers 2 to 3 dB gain over HD decoding [90].

FEC schemes that have been proposed for optical transmission systems can be classified into various generations. The first generation FEC codes have used a single HD code, such as Bose-Chaudhuri-Hocquenghem (BCH) or Reed-Solomon (RS) codes. The most common code was the RS(255,239), which has an overhead of ~7% and offers a NCG of ~6 dB at BER of 10^{-12}. This code has been proposed for long haul optical transmission systems as specified by the ITU-T G.975 [91] and G.709 [92] recommendations. In order to go beyond the NCG of a single HD FEC, concatenated code schemes [93] together with interleaving and iterative HD decoding were employed for 10 Gb/s and 40 Gb/s WDM systems. These types of FEC codes are referred to as "second generation". Nine different code concatenation schemes were defined in the ITU-T G.975.1 recommendation [94], having an overhead of ~7% and show NCG of ~8-9 dB at BER of 10^{-15}. It is worth mentioning that some of these codes have the potential to deliver higher coding gain, up to ~10 dB, by increasing the OH to 25% or by employing a SD decoding scheme. The third generation FEC codes were based on the SD and iterative decoding. There are two main SD-FEC options suitable for optical communication. The first option is based on turbo product codes (TPCs) [95], which are constructed by a serial concatenation of two or more block codes with a block interleaver in between. This class of codes tends to have a very low error floor owing to their large minimum distance [96]. In addition, such codes provide a very good performance at high code rates and permit a high degree of parallelization of the encoder and decoder [96]. TPCs have already been implemented successfully on application-specific integrated circuit (ASIC) platform for optical communications [97].

The second common option is based on low-density parity-check (LDPC) codes [98]. They have been studied intensively and adopted by various communication standards because of their superior

performance. In optical communications systems, several LDPC codes have been evaluated [99, 100]. Typically, these codes have an overhead of 15% to 25% and give a NCG > 10 dB at BER of 10^{-15}. A comprehensive overview of FEC codes in optical communication can be found in [96, 101-104].

Fig. 2.8 shows the ultimate NCG that can be obtained at BER= 10^{-15} as a function of code OHs in a binary input AWGN channel using HD or unquantized SD techniques [105, 106]. In addition, the NCGs of some modern HD- and SD-FEC codes reported for optical communication systems are shown as open and filled symbols, respectively. Triangles refer to the codes which have been implemented on ASICs, squares refer to codes which have been verified on field-programmable gate arrays (FPGA), and circles indicate codes which have been evaluated by numerical simulations.

Most of the FEC schemes proposed for digital coherent systems at 100 Gb/s and beyond have an OH of ~7% to ~20%. For FEC codes with ~7% OH, out of the code options defined by the ITU-T standard G.975.1, the best code in terms of delivered NCG is described in Appendix I.3 [94]. It has an OH of 6.69% and gives a NCG= 8.99 dB at BER= 10^{-15} after three HD iterative decoding and it is already implemented on an intellectual property (IP) core [107]. Another two interesting HD-FEC codes are proposed and implemented in [108] and [109, 110]. These have 7% OH and provide NCGs of 9.3 dB and 9.4 dB at BER= 10^{-15}, respectively. Larger coding gain of 9.55 dB, which is only 0.42 dB from HD capacity, is provided using the HD-FEC code described in [111]. The NCG can be further improved by using SD decoding. ViaSat demonstrated a SD-FEC with 7% OH based on TPC which delivers a NCG of 10.3 dB [108].

For FEC codes with ~20% OH, a NCG of 10.5 dB can be obtained using a HD-FEC [111]. However, the NCG can be improved by ~1 dB by utilizing SD-FEC based on TPC [108] and LDPC [112] codes. Furthermore, by increasing the OH to 25%, it is possible to achieve a NCG of 12.14 dB [113], which is 0.83 dB from the SD capacity limit.

It can be concluded that SD decoding normally reaps the benefits of the extra reliability information provided by the ADC unit, which results in a better performance compared with the HD decoding. However, this comes at the expense of higher implementation complexity. For practical systems, there are many factors that contribute to the choice of the FEC scheme, such as latency, complexity, power consumption, flexibility, NCG, etc. Therefore, the systems designer

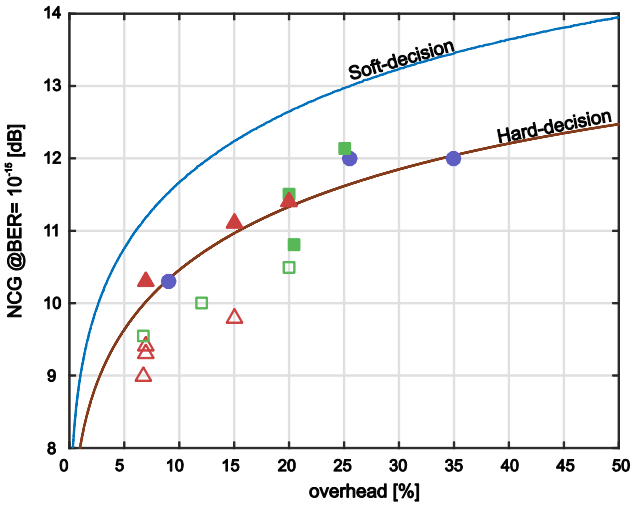

Fig. 2.8: The ultimate NCG that can be achieved at BER= 10^{-15} using HD and SD decoding (solid lines). Also, the NCG for some modern FEC codes are shown as symbols.

should take into account these parameters and select the code, whether it is HD- or SD-FEC, to satisfy the application requirement.

CHAPTER 3

Four-Dimensional Modulation Formats Based on Lattice

This chapter starts with a brief overview of lattices and their properties. Then, it shows how dense *N*-dimensional (*N*-D) lattices can be utilized to construct a power efficient signal constellation. In particular, the densest lattice in the 4-D space will be studied. Following, some important 4-D signal constellations will be discussed. Finally, the digital signal processing functions for some 4-D modulation formats will be described in detail.

3.1 The Lattices and their properties

A lattice Λ is an infinite array of discrete points in the *N*-dimensional (*N*-D) space. It can be generated by a set of *N* orthogonal basis vectors, called generator matrix $\boldsymbol{G}$, with:

$$G = [v_1, v_2, \dots, v_N]^T \tag{3-1}$$

Where $v_1, v_2, \dots, v_N$ are the basis vectors and T denotes matrix transpose. The lattice points (vectors) are obtained as an integer linear combination of basis vectors, i.e. $\Lambda = iG$, where $i = (i_1, i_2, \dots, i_N)$ is a vector with elements $i_N \in \mathbb{Z}$. Thus, the lattice Λ comprises infinite set of vectors which is closed under addition and subtraction, i.e. form an additive group.

A subset of Λ is called a sublattice Λ', which also form an additive group. A coset of Λ' in Λ is obtained by translation of Λ' by an element $u \in \Lambda$. Thereby, a lattice Λ can be partitioned by a set of cosets of Λ' as following:

$$\Lambda = \bigcup_{i=0}^{t-1} (u_i + \Lambda') \tag{3-2}$$

i.e. the lattice Λ can be formed by a union of the sublattice Λ' and its coset. This partitioning is denoted by Λ/Λ', where *t* is number of cosets of Λ' in Λ, which is called the *index* of Λ' in Λ.

A modified version of a given lattice Λ, which maintains the lattice properties, can be obtained by two different operations: (1) *Scaling*, a lattice Λ can be scaled by a real number q, such that $q\Lambda$ is a scaled version of Λ. (2) *Orthogonal transformation*, a lattice Λ can be transformed by a real valued orthogonal matrix R (i.e $RR^T = I$ where I is the identity matrix), that results in a transformed (rotated) version $R\Lambda$ of Λ.

In 2-dimensional space, the integer lattice $\Lambda = \mathbb{Z}^2$ is generated by the generator matrix $G_{\mathbb{Z}^2}$:

$$G_{\mathbb{Z}^2} = \begin{bmatrix} 1 & 0 \\ 0 & 1 \end{bmatrix} \tag{3-3}$$

It consists of an infinite set of 2-tuples of integer numbers as shown in Fig. 3.1 (a). A scaled and rotated version of $\mathbb{Z}^2$ can be obtained by applying following transformation:

$$R = \begin{bmatrix} 1 & 1 \\ 1 & -1 \end{bmatrix} \tag{3-4}$$

This transformation is equivalent to a $\pi/4$ rotation of $\mathbb{Z}^2$ and scaling it by $\sqrt{2}$. It can be noted that $R\mathbb{Z}^2$ forms a sublattice of $\mathbb{Z}^2$. The $\mathbb{Z}^2$ can be then represented as a disjoint union of $R\mathbb{Z}^2$ and its coset:

$$\mathbb{Z}^2 = R\mathbb{Z}^2 \cup \{(1,0) + R\mathbb{Z}^2\} \tag{3-5}$$

Since the number of cosets is two, then the partitioning $\mathbb{Z}^2/R\mathbb{Z}^2$ has an index of two. Fig. 3.1(a) shows the cosets of this partitioning as filled and empty circles.

Another lattice in the 2-dimensional space is the hexagonal lattice, referred to as A_2. It is shown in Fig. 3.1 (c). It can be generated by the following generator G_{A_2} [114, p. 110]:

$$G_{A_2} = \begin{bmatrix} 1 & 0 \\ 1/2 & \sqrt{3}/2 \end{bmatrix} \tag{3-6}$$

For each lattice's point $\xi_q \in \Lambda$, there is a region which encloses all points that are closer to ξ_q than any other lattice point $\xi_p \in \Lambda$, where q and p are integer numbers where $q \neq p$. This sphere is called *Voronoi cell* or *fundamental region* [114]. The fundamental region for $\mathbb{Z}^2$ and A_2 are shown in Fig. 3.1 (a) and (b) as dashed squares and dashed regular hexagons, respectively. The volume of the fundamental region $V(\Lambda)$ is given as [114, p. 4]:

$$V(\Lambda) = \sqrt{|\det(B)|} \tag{3-7}$$

Where B is the Gram matrix, which is equal to the generator matrix of Λ times its transpose. i.e. $\mathrm{B} = \mathrm{GG}^{\mathrm{T}}$. One important property of a lattice is its *density*, which determines the efficiency of packing non-overlapping N-dimensional spheres with identical size in a given region of space. The density of a N-D lattice can be calculated as [114, p. 7]:

$$\Delta = \frac{volume\ of\ one\ N\text{-dimensional}\ sphere}{V(\Lambda)} \tag{3-8}$$

Fig. 3.1 (c) and (d) show an enlargement of $\mathbb{Z}^2$ and A_2 lattices with 2-dimensional equal spheres (circles) centered at lattice points and the fundamental regions, which are square and regular hexagonal, respectively. The density of these lattices can be easily found from (3-8) as:

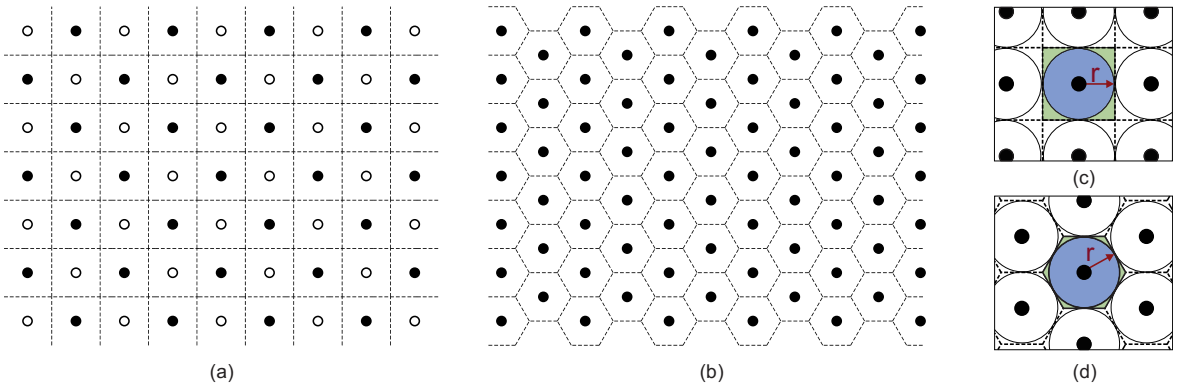

Fig. 3.1: (a) $\mathbb{Z}^2$ lattice, where the filled and empty circles represent the two cosets for $\mathbb{Z}^2/R\mathbb{Z}^2$ partitioning (b) A_2 lattice (c) An enlargement of (a) showing the fundamental region (green square) and packing spheres around lattice points. (d) An enlargement of (b) showing the fundamental region (green regular hexagonal) and packing spheres around lattice points.

$$\Delta_{\mathbb{Z}^2} = \frac{\pi r^2}{4r^2} = 0.7854$$
$$\Delta_{A_2} = \frac{\pi r^2}{2\sqrt{3}\, r^2} = 0.9069 \tag{3-9}$$

Therefore, A_2 is denser than $\mathbb{Z}^2$ by a factor of 0.62 dB. Actually, the A_2 lattice is the densest lattice in the 2-D space[114]. That is, larger number of lattice points can be packed into a given area using A_2 lattice while keeping the *minimum Euclidean distance* ($d_{min} = 2r$) between lattice points constant. Equivalently, smaller area is occupied by packing *x* number of spheres using A_2 rather than packing the same number of spheres with $\mathbb{Z}^2$. This technique is of practical interests in digital communication systems in many aspects [114, p. 11]. One of these aspects is to construct optimum signal constellation for uncoded modulation systems in the *N*-D space, which will be discussed in the reminder of this chapter. Special attention will be paid for finding the optimum signal constellations in the 4-D space, which is particularly interesting for coherent optical communication as we have discussed in Chapter 2. Another aspect is to use lattice partitioning to achieve coding gain as we will discuss in Chapter 4.

3.2 Lattice coding gain

The signal constellation $\mathcal{C}$ can be obtained by cutting a region $\mathcal{R}$ form an (possibly translated and/or scaled) *N*-D lattice, the lattice points enclosed by the region boundaries forms the signal constellation. Therefore, signal constellations can be considered as a finite set of points selected from the *N*-D lattice [115, 116]. Fig. 3.2 (a) shows the square QAM constellation with *M*=16 signal points, referred to as *square* 16QAM. It is obtained by cutting a square region form a scaled 2-D integer lattice $\mathbb{Z}^2$. Fig. 3.2 (b) shows another signal constellation, with the same number of points *M*=16, based on a scaled hexagonal A_2 lattice [116-118], referred to as *hexagonal* 16QAM. This signal constellation is bounded by a regular hexagon rather than a square as in the square QAM constellation.

When a lattice-based constellation is used for digital communication, each block of *b* information bits is assigned to one of the $M = 2^b$ possible signal points. At the receiver side, the decision unit maps the received noisy signal points into an estimate of the transmitted signal points. Assuming a uniform distribution of the transmitted signal points, the decision unit uses the maximum likelihood decision (MLD) rule. Therefore, it assigns all received signal points that fall within a voronoi cell to the center of this voronoi cell (the signal constellation point). Thus, a voronoi cell is also called the decision region. Nevertheless, a decision error occurs when the received signal point fall outside the decision region of its corresponding transmitted signal. These errors can happen with some probability. For sufficiently high signal-to-noise ratio (SNR) and for equally probable symbols, the probability of symbol error on an AWGN channel can be approximated by [106]:

$$P_s \approx K\, \mathrm{Q}\left(\sqrt{\frac{d_{min}^2}{2N_0}}\right) \tag{3-10}$$

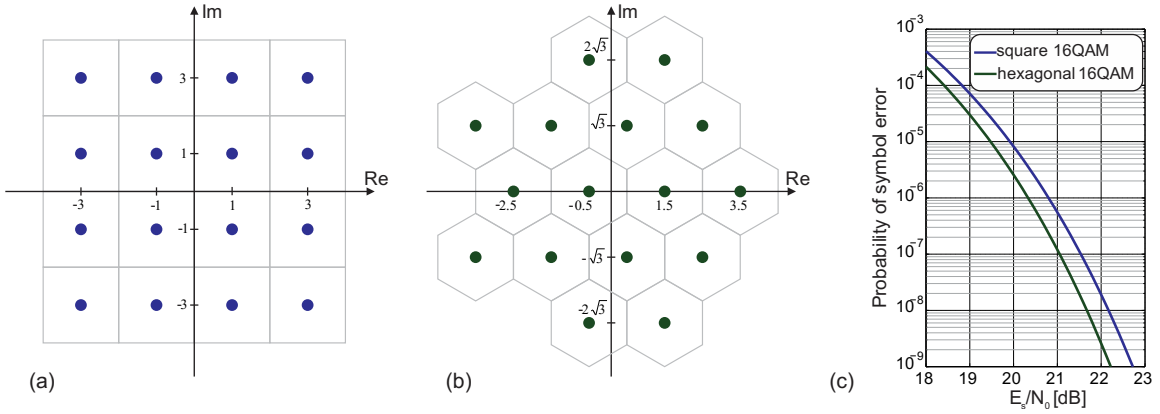

Fig. 3.2: (a) square 16QAM signal constellation (b) hexagonal 16QAM signal constellation (c) probability of symbol error as a function of signal to noise ratio E_s/N_0 for square and hexagonal 16QAM signals.

where d_{min} is the minimum Euclidean distance between signal (lattice) points and N_0 is the power spectral density of the additive noise. K is the number of nearest neighbors. That is, the number of signal points at distance d_{min} from a given signal point. Geometrically, K is called *kissing number*, which is the maximum number of non-overlapping N-D spheres that touch a given sphere centered at a lattice point. For example, from Fig. 3.1(c) and (d), it can be easily seen that the kissing number for $\mathbb{Z}^2$ and A_2 are $K_{\mathbb{Z}^2} = 4$ and $K_{A_2} = 6$, respectively.

The Gaussian Q-function is defined as:

$$\mathrm{Q}(x) \approx \frac{1}{2}\,\mathrm{erfc}\left(\frac{x}{\sqrt{2}}\right) \tag{3-11}$$

Where

$$\mathrm{erfc}(x) = \frac{2}{\sqrt{\pi}}\int_x^{\infty} e^{-l^2} dl \tag{3-12}$$

is the complementary error function for $x > 0$. Clearly, the probability of error P_s decreases as d_{min} increases at a given average energy. Accordingly, a metric is defined to determine the efficiency of a given signal constellation $\mathcal{C}$. It is called the *asymptotic power efficiency* $\gamma(\mathcal{C})$ [119]:

$$\gamma(\mathcal{C}) = \frac{\beta \cdot d_{min}^2}{E_b} = \frac{\beta \cdot d_{min}^2 \cdot log_2(M)}{E_s} \tag{3-13}$$

Where $E_b = E_s/log_2(M)$ is the average energy per bit and E_s is the average energy of the constellation points $\xi_i \in \mathcal{C}$, where ξ_i are equiprobable:

$$E_s = \frac{1}{M}\sum_{i=1}^{m} \|\xi_i\|^2 \tag{3-14}$$

β is a normalization factor, which is normally set to $\frac{1}{4}$ thus $\gamma(\mathcal{C})$ for BPSK and QPSK formats is equal to one. Accordingly, the $\gamma(\mathcal{C})$ can be understood as the power efficiency improvement over BPSK/QPSK formats operating at the same bit rate [33, 120].

The asymptotic power efficiency $\gamma(\mathcal{C})$ describes how much effectively a signal constellation exploits the available signal energy to maximize the d_{min} between constellation points. Therefore,

when designing a modulation scheme, one should try to maximize $\gamma(\mathcal{C})$, which subsequently minimizes the probability of symbol error. That can be attained by increasing the d_{min} while keeping the average energy constant or minimizing the average energy and retain the d_{min} unchanged. This condition can be actually directly achieved by finding a densest lattice in a given *N*-dimensions which was discussed in Section 3.2. For a given *N*-D signal space, the nominal lattice coding gain of a lattice Λ denoted by $\gamma_c(\Lambda)$ [121, 122]:

$$\gamma_c(\Lambda) = \frac{d_{min}^2}{V(\Lambda)^{\frac{2}{N}}} \tag{3-15}$$

This represents the reduction in average signal energy that can be attained using dense *N*-D Λ lattice. For the 2-D lattice, A_2 is the densest lattice and the nominal lattice coding gain is $\gamma_c(A_2) = 2/\mathrm{sqrt}(3)$ or 0.62 dB. For $\mathbb{Z}^2$ the nominal lattice coding gain is $\gamma_c(\mathbb{Z}^2) = 1$ or 0 dB. That means, up to 0.62 dB coding gain can be attained by implementing a signal constellation based on A_2 compared with $\mathbb{Z}^2$ lattice with the same boundary. Note that the coding gain remains unchanged for the scaled version of a given lattice, since it will scale $V(\Lambda)$ and d_{min} such that the ratio stays constant [121].

In addition to the reduction in average energy obtained by the densest lattice, there is another factor that influences the average energy of a signal constellation, which is the shape of the boundary that encloses the signal constellation points, denoted by $\mathcal{R}$. Of course, the optimum boundary would be in general the *N*-D sphere. This energy saving introduced by *N*-D sphere boundary over *N*-D cube boundary is called shaping gain $\gamma_s(\mathcal{R})$. The shaping gain of the *N*-D cube boundary is then $\gamma_s(\mathcal{R}_{cube}) = 0$ dB. The maximum shaping gain of *N*-D sphere when $N \to \infty$ is 1.53 dB. For 2D-sphere (circle) boundary $\gamma_s(\mathcal{R}_{circle}) = 0.2$ dB and for 4D-sphere boundary $\gamma_s(\mathcal{R}_{4-D\ sphere}) = 0.46$ dB [121].

The total nominal coding gain, denoted by γ_t, is equal to $\gamma_t = \gamma_c(\Lambda) \cdot \gamma_s(\mathcal{R})$, which can be approximated as [114, p.73]:

$$\gamma_t = \frac{(N+2)}{3} \cdot \Delta^{2/N} \tag{3-16}$$

For the example presented in Fig. 3.2, two constellations were used, square 16QAM based on scaled $\mathbb{Z}^2$ with square boundary and hexagonal 16QAM based on scaled A_2 with hexagonal boundary. The potential total coding gain in the 2-D signal space is equal to $\gamma_t = \gamma_c(A_2) + \gamma_s(\mathcal{R}_{circle}) = 0.82$ dB. Note, that the same value can be directly calculated from Equation (3-16). Both signal constellations have the same $d_{min}^2 = 4$. However, the average signal energies for square and hexagonal 16QAM are 10 and 8.76, respectively. Hence, hexagonal 16QAM offers an energy reduction compared with square 16QAM. On the other hand, the average number of nearest neighbors K_{min} for square and hexagonal 16QAM are 3 and 4.125, respectively. The increase in number of nearest neighbors will limit the achievable coding gain, especially for higher dimensional *N* when K_{min} becomes very large [123].

Fig. 3.2 (c) shows the probability of symbol error P_s for the two signal constellations as a function of E_s/N_0. It can be seen that the hexagonal 16QAM offers 0.5 dB sensitivity improvement at $P_s = 10^{-9}$. This improvement is attributed on one hand to the higher density of the hexagonal lattice compared with integer lattice (coding gain) and onn the other hand to the hexagonal boundary over

the square boundary (shaping gain). The hexagonal 16QAM is considered the optimum 2-D signal constellation for *M*= 16 [116].

3.3 Four-dimensional Lattices

In the 4-D space, the basic lattice is the 4-D integer lattice (cubic lattice), denoted by $\mathbb{Z}^4$. It can be simply constructed by a Cartesian product of $\mathbb{Z}^2$ with itself, i.e. $\mathbb{Z}^4 = \mathbb{Z}^2 \times \mathbb{Z}^2$. That would mean that both lattices, $\mathbb{Z}^4$ and $\mathbb{Z}^2$, have the same minimum squared distance and the same fundamental volume. Subsequently, the nominal lattice coding gain is $\gamma_c(\mathbb{Z}^4) = 0$ dB. Therefore, the nominal lattice coding gain $\gamma_c(\Lambda)$ can be interpreted as the sensitivity gain that can be achieved by implementing a signal constellation based on a *N*-D Λ lattice with density Δ over a signal constellation based on the $\mathbb{Z}^N$ lattice.

The densest lattice in 4-D space is the Schläfli lattice D_4, which can be described by the following generator matrix [114, p. 9]:

$$G_{D_4} = \begin{bmatrix} 2 & 0 & 0 & 0 \\ 1 & 1 & 0 & 0 \\ 1 & 0 & 1 & 0 \\ 1 & 0 & 0 & 1 \end{bmatrix} \tag{3-17}$$

D_4 can be obtained from $\mathbb{Z}^4$ by selecting all 4-tubles signal points $\xi \in \mathbb{Z}^4$ whose coordinates sum to an even integer:

$$D_4 = \left\{ \xi = (\xi_1, \xi_2, \xi_3, \xi_4) \in \mathbb{Z}^4 : \sum_{i=1}^{4} \xi_i \; is \; even \right\} \tag{3-18}$$

Therefore, D_4 is a sublattice of $\mathbb{Z}^4$, and the partitioning $\mathbb{Z}^4/D_4$ consists of two cosets, one being D_4 itself which comprises points with even norm and another is its translate $D_4 + (1,0,0,0)$ which comprises points with odd norm [121].

The minimum distance between D_4 lattice points $d_{min}$is $\sqrt{2}$ and the fundamental region is $V(D_4) = \sqrt{det\left(G_{D_4} \cdot G_{D_4}^T\right)} = 2$. From Equation (3-15), the nominal lattice coding gain for D_4 over $\mathbb{Z}^4$ is $\gamma_c(\mathrm{D}_4) = 2/\sqrt{2} = 1.4142$ or 1.51 dB. The total nominal coding gain can be calculated from Equation (3-16) as $\gamma_t = 1.57$ or 1.96 dB, where the density of the D_4 is $\Delta_{D_4} = \pi^2/16$ [114, p. 10]. However, the kissing number of D_4 (K_{D_4}= 24) is increased by a factor of three compared with $\mathbb{Z}^4$ ($K_{\mathbb{Z}^4}$= 8). It can be seen from Equation (3-10), that the increase of *K* will have an impact on the performance of the modulation format based on high dimensional dense lattice, especially in the low SNR regime. As discussed in [123], each increase in *K* by a factor of 2 will be translated to a loss of 0.2 dB from nominal lattice coding gain. Accordingly, when the effect of *K* is considered, then the *effective* lattice coding gain for D_4 over $\mathbb{Z}^4$ will be reduced to approximately 1.6 dB.

3.4 Four dimensional modulation formats

The problem of finding the optimal signal constellation for a given number of points M in the 4-D space was already discussed in literature [119, 124-129]. A good starting point would be to select a subset with M points from the D_4 , the densest lattice in the 4-D space. However, this would not necessarily gives the optimal signal constellation.

Within the framework of optical communication systems, Agrell and Karlsson in 2009 [120, 130], have discussed the sensitivity gains attained by optimizing the signal constellation in 4-D over 2-D space. Additionally, they described in detail some important 4-D modulation formats.

Using a numerical optimization technique, a table of best 4-D signal constellations is presented in [131]. Some of these constellations are based on the D_4 lattice and some are not, as discussed in [132, 133]. The results of this optimization are plotted in Fig. 3.3, where the spectral efficiency for optimized 4-D signal constellations is plotted as a function of asymptotic power efficiency. Fig. 3.3 also shows the baseline performance of the conventional MQAM formats. The asymptotic power efficiency for MQAM formats is [33, p. 234]:

$$\gamma_{M-QAM} = \frac{3}{2} \cdot \frac{log_2 M}{M-1} \tag{3-19}$$

Where the constellation size M is power of 4. It should be noted that the power efficiency for M-QAM formats remains unchanged when they are used in PDM configuration. Since the polarization tributaries carry two *independent* MQAM signal. For even values of spectral efficiency, particularly for M= 4, 16 and 64, the corresponding formats are marked on the baseline performance. Two other formats with odd values of spectral efficiency are also plotted, namely star-8QAM and cross-32QAM [134]. It is noted that the constellation with M= 32 is slightly more power efficient than the baseline. That is because the cross shaped constellation offers 0.14 dB reduction in average power over square shaped constellation for the same constellation size M [116].

It should be noticed that a coding gain of 1.89 dB can be already obtained for $M = 4096$ [131], that is very close to the total nominal coding gain of 1.96 in the 4-D space when $M \to \infty$.

Some interesting D_4 based signal constellations are shown in Fig. 3.3, which will form the subject of the next sub-sections.

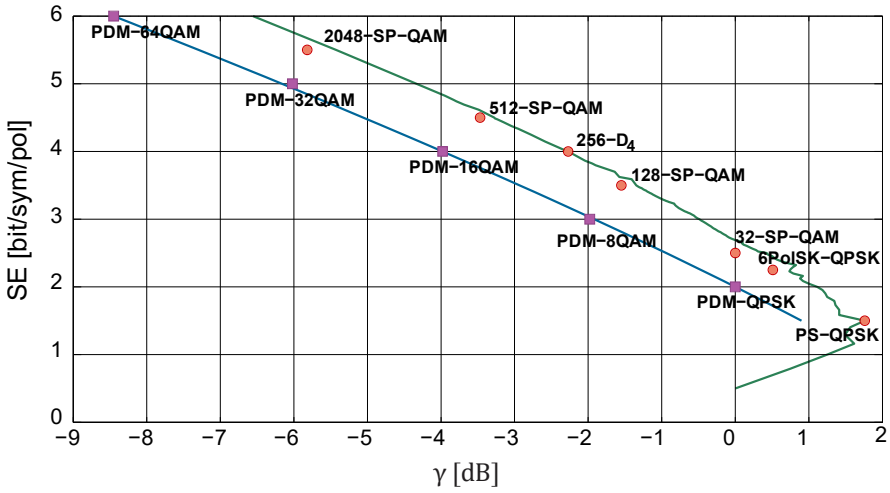

Fig. 3.3: Spectral efficiency as a function of asymptotic power efficiency γ for optimum 4-D signals (green) [131] and for M-QAM signals (blue). Some 4-D modulation formats (circles) and PDM-MQAM formats (squares) are also marked.

3.4.1 PS-QPSK

Polarization-switched (PS-) QPSK is recognized as the most power efficient signal constellation in the 4-D space. In an optical coherent system, it can be considered as transmitting one QPSK signal in either state of polarizations, hence the name. It has *M*= 8 points and thus SE= 1.5 bit/sym/pol. Its coordinates are [120]:

$$\mathcal{C}_{PS-QPSK} = \{(\pm 1, \pm 1, 0, 0), (0, 0, \pm 1, \pm 1)\} \tag{3-20}$$

This signal representation is shown in Fig. 3.4 (a). The PS-QPSK symbol carries three information bits, two of which are used to encode the QPSK signal and the third is used to choose whether x-polarization or y-polarization is used for transmission. Using the signal representation defined in Equation (3-20), it would require three modulation levels to drive the modulators at the transmitter. Alternatively, applying a 45° polarization rotation and scaling it by $\sqrt{2}$ would lead to a more appropriate representation with two levels only [120]:

$$\hat{\mathcal{C}}_{PS-QPSK} = \{\pm(1, 1, 1, 1), (1, 1, -1, -1), (1, -1, 1, -1), (1, -1, -1, 1)\} \tag{3-21}$$

This signal constellation is actually equivalent to a rate 3/4 single parity check code [135], where each PS-QPSK symbol consists of three information bits and the forth redundant bit is a modulo-2 sum of the three information bits. This signal representation is depicted in Fig. 3.4 (b). In this representation, PS-QPSK forms a subset of the PDM-QPSK constellation, where only symbols combinations with the same color in both polarizations are permitted. This results in an increase of d_{min} by a factor of $\sqrt{2}$ for the PS-QPSK format, and thus a nominal coding gain of 1.76 dB.

Fig. 3.4 (c) shows the BER as a function of OSNR for PS-QPSK and PDM-QPSK at 112 Gb/s, the results are obtained by a Monte Carlo simulations in an AWGN channel. It can be seen that the PS-QPSK offers approximately 1 dB sensitivity improvement at BER of 10^{-3}. Nevertheless, this sensitivity gain is obtained at the expense of a spectral efficiency reduction of 0.5 bit/sym/pol. That would mean the PS-QPSK need 25% increases in symbol rate in order to operate at the same bit rate as PDM-QPSK.

The PS-QPSK format was already discussed in communication community [119, 128, 129, 136] including optical coherent systems [137]. Since 2009, a series of simulation studies and experimental works have been conducted to evaluate the performance of this format. Bit-to-symbol mapping rules and the exact expression to calculate SER and BER for PS-QPSK were presented in

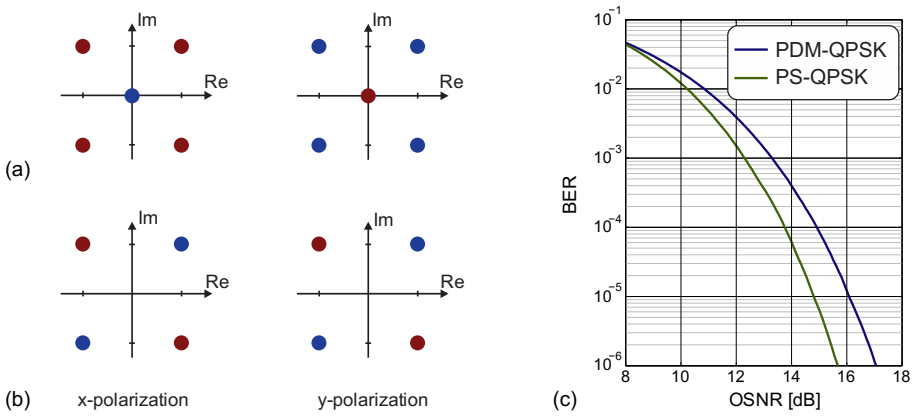

Fig. 3.4: (a) The PS-QPSK constellation as defined in Eq. (3-20) (b) Another representation for PS-QPSK constellation as defined in (3-21) (c) The BER as a function of OSNR for PS-QPSK and PDM-QPSK in AWGN channel at 112 Gb/s.

[120, 130]. The sensitivity improvement of PS-QPSK over PDM-QPSK was demonstrated experimentally for bit rates of 30 Gb/s [138] 40.5 Gb/s [139] 42.5Gb/s [140] 112 Gb/s [141-143]. The sensitivity advantage of PS-QPSK is translated to 10% to 30% increase in maximum reach compared at the same bit rate with PDM-QPSK at a BER of 10^{-3} [140, 142, 143]. Numerical simulations show that PS-QPSK has better tolerance against nonlinear impairments compared to PDM-QPSK in WDM nonlinear transmission scenario [144-146], this result was also verified experimentally [139, 142, 143]. FPGAs implementation of the PS-QPSK receiver was reported in [147], it was shown that the DSP resources required for PS-QPSK is only 1% higher than for PDM-QPSK. Moreover, PS-QPSK format operating at 100 Gb/s over transcontinental distances is now supported by a newly released transponder product [148].

3.4.2 24-cell and 6PolSK-QPSK

An attractive 4-D signal constellation for *M*= 24 is named *24-cell.* It was studied in the context of communication systems in [119, 128, 129, 149]. Later, it was proposed for coherent optical systems [130, 150]. The signal constellation for 24-cell [130]:

$$\mathcal{C}_{24-cell} = \{(\pm 1, \pm 1, 0, 0)\} \tag{3-22}$$

with arbitrary sign and permutations. This constellation can be described as a union of two constellations, namely, the PS-QPSK constellation given in Equation (3-20) and the PDM-QPSK constellation:

$$\mathcal{C}_{PDM-QPSK} = \{(\pm 1, 0, \pm 1, 0), (\pm 1, 0, 0, \pm 1), (0, \pm 1, \pm 1, 0), (0, \pm 1, 0, \pm 1)\} \tag{3-23}$$

That is, $\mathcal{C}_{24-cell} = \mathcal{C}_{PDM-QPSK} \cup \mathcal{C}_{PS-QPSK}$. Fig. 3.5 (a) shows the $\mathcal{C}_{24-cell}$ constellation composed of PS-QPSK (red and blue circles) and PDM-QPSK (green circles). The corresponding time-resolved state of polarization (SOP) on the Poincaré sphere is plotted in Fig. 3.5 (b). It can be seen that $\mathcal{C}_{24-cell}$ employs six different SOPs, where PDM-QPSK employs four SOPs (linear ±45°, right/left-hand circular) and PS-QPSK employs two SOPs (linear horizontal/vertical).

It can be noted that $\mathcal{C}_{24-cell}$ has the same d_{min} and average energy as $\mathcal{C}_{PDM-QPSK}$, but comprises eight additional signal points. Therefore, $\mathcal{C}_{24-cell}$ offers an asymptotic coding gain of $\frac{log_2(24)}{log_2(16)} = 1.1462 = 0.59\ dB$ over $\mathcal{C}_{PDM-QPSK}$. One thing that should be considered for $\mathcal{C}_{24-cell}$, is the fact that the constellation size is a non-power of two, which leads to a fractional number of bits per symbol. Some techniques to overcome this issue were briefly discussed in [151]. In addition, shell mapping techniques can be utilized to map a noninteger number of bits per symbol [152].

An interesting way to form a signal constellation based on $\mathcal{C}_{24-cell}$ was proposed in [130, 150]. The Cartesian product of $\mathcal{C}_{24-cell}$ with itself gives an 8-D set $\mathbb{C} = \mathcal{C}_{24-cell} \times \mathcal{C}_{24-cell}$ which has $24^2 = 576$ points. The proposed signal constellation, denoted by 6-ary polarization-shift keying quadrature phase-shift keying (6PolSK-QPSK), is then obtained by selecting a subset from $\mathbb{C}$:

$$\mathcal{C}_{6PolSK-QPSK} = \begin{Bmatrix} \mathcal{C}_{PDM-QPSK} \times \mathcal{C}_{PDM-QPSK}, \\ \mathcal{C}_{PDM-QPSK} \times \mathcal{C}_{Ps-QPSK}, \\ \mathcal{C}_{Ps-QPSK} \times \mathcal{C}_{PDM-QPSK} \end{Bmatrix}. \tag{3-24}$$

Hence, the subset $\mathcal{C}_{Ps-QPSK} \times \mathcal{C}_{PS-QPSK}$ was excluded from $\mathbb{C}$ and the 6PolSK-QPSK signal constellation contains 512 points. Each 8-D 6PolSK-QPSK symbol is transmitted in two consecutive time-slots. It carries 9 information bits and so it has a SE= 2.25 bits/sym/pol. The

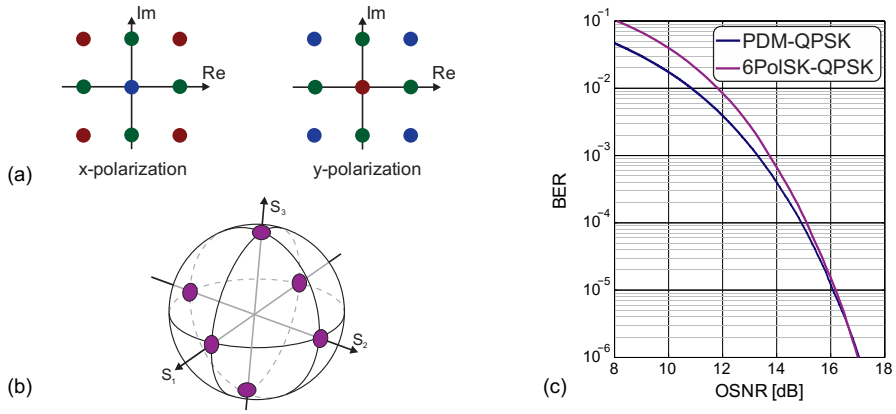

Fig. 3.5: (a) $\mathcal{C}_{24-cell}$ signal constellation (b) The corresponding time-resolved SOP on the Poincaré sphere (c) The BER as a function of OSNR for 6PolSK-QPSK and PDM-QPSK in AWGN channel at 112 Gb/s.

6PolSK-QPSK format gives a coding gain of 0.51 dB, which is a slightly less than for $\mathcal{C}_{24-cell}$ [130].

Fig. 3.5 (c) shows the BER obtained from Monte Carlo simulations as a function of OSNR for 6PolSK-QPSK and PDM-QPSK for an AWGN and at the same data rate of 112 Gb/s, where the bit-to-symbol mapping is discussed in [130]. As seen the 6PolSK-QPSK does not offer a sensitivity advantage over PDM-QPSK for BER> 10^{-6}, the coding gain can be rather realized only at very low BER. This can be attributed to the fact that the 6PolSK-QPSK is anti-Gray mapping format. That is, no gray mapping is possible and a single symbol error won't necessarily lead to a single bit error. In addition, the average number of nearest neighbors for 6PolSK-QPSK is 14 in the 8-D space, while it is only 4 for PDM-QPSK in the 4-D space. As the result, the BER performance is degraded specially in the low OSNR regime where the number of nearest neighbors plays an important rule.

The 6PolSK-QPSK format was realized experimentally and compared with PDM-QPSK at the same symbol rate of 28 GBd in the b2b configuration [153] and in WDM transmission system [154]. It was proposed in [150], that the 12.5% increase in SE of 6PolSK-QPSK compared with PDM-QPSK at the same symbol rate can be exploited to implement an outer Reed-Solomon RS(511,455) FEC code. The simulation result for this scheme suggests a 1.7 dB sensitivity improvement at BER= 10^{-3}. However, the experimental results show that the potential advantage of 6PolSK-QPSK combined with RS(511,455) was dissipated after all due to the extra implementation penalty compared with PDM-QPSK [155, 156], only a slight advantage of 0.2 dB was measured [155]. Furthermore, It was shown in [157, 158], that the anti-Gray mapping problem for 6PolSK-QPSK can be mitigated by employing an iterative demapping (ID) technique with soft-decision based FEC code. The later approach was demonstrated experimentally in [155]. The degree profile of an LDPC code was optimized for 6PolSK-QPSK format. The b2b experimental results show, that the 6PolSK-QPSK combined with optimized LDPC code with ID and bit interleaver techniques, offer a sensitivities advantage of 1.7 dB and 0.5 dB compared with PDM-QPSK at BER= 3.8×10^{-3} at data rate of 105 Gb/s and 91 Gb/s, respectively. Moreover, the nonlinear tolerance of 6PolSK-QPSK format was investigated in [155] and the interaction between the FEC code and nonlinear compensation (NLC) technique was discussed in [159].

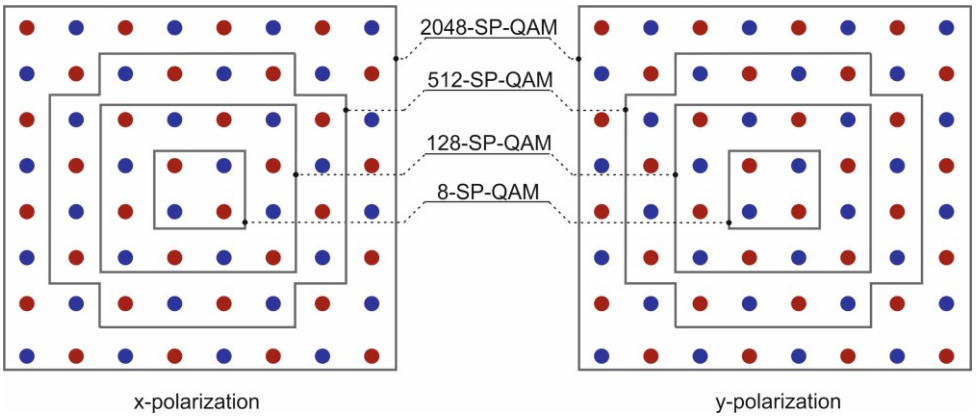

Fig. 3.6: *M*-SP-QAM signal constellation diagrams for *M*= 8, 128, 512 and 2048. Note that, only combinations of points with the same color between the two polarizations are allowed.

3.4.3 *M*-SP-QAM

The conventional PDM-*M*QAM formats can be considered either as two independent 2-D *M*QAM signals based on $\mathbb{Z}^2$ or as a 4-D signal based on $\mathbb{Z}^4$. As discussed in Section 3.3, the two-way partition of $\mathbb{Z}^4$ lattice gives the D_4 lattice with its coset. In other words, the D_4 lattice is formed by selecting every second point from the $\mathbb{Z}^4$ lattice. Therefore, a set of 4-D modulation formats based on D_4 can be constructed by applying a set-partitioning technique on the PDM-*M*QAM formats [160]. This approach was suggested for optical coherent system in [161] and it is referred to as *M*-ary set-partitioned QAM (*M*-SP-QAM). It should be emphasized that the constellation size *M* for PDM-*M*QAM is normally refers to the number of signal points in the 2-D space, while for *M*-SP-QAM it is defined as the number of signal points in the 4-D space.

Fig. 3.6 shows some *M*-SP-QAM signal constellation diagrams with $M= 2^n$ where *n* is an even number greater than or equal to four. It can be noted that a 2-way partition of the PDM-*M*QAM signal constellation gives a *M*-SP-QAM signal constellation comprising only half of the points in the 4-D space. As example, 128-SP-QAM format has 128 signal points in the 4-D space and it can be obtained by 2-way partition of the PDM-16QAM, which has 256 points in the 4-D space. Note that, a 2-way partition of *M*-SP-QAM signal constellation brings us back to the signal constellation

Table 3-1: The ROSNR for selected *M*-SP-QAM and PDM-*M*QAM formats at BER= 3.8×10^{-3}. All modulation formats are operating at fixed symbol rate of 28 GBd. The information bit rates are calculated assuming a total overhead of 12% for the protocol and HD-FEC

Modulation format	SE [bit/sym/pol]	Information bit rate [Gb/s]	ROSNR [dB]
8-SP-QAM	1.5	75	10
PDM-4QAM	2.0	100	12.1
32-SP-QAM	2.5	125	14
PDM-8QAM	3.0	150	16.1
128-SP-QAM	3.5	175	17
PDM-16QAM	4.0	200	18.7
512-SP-QAM	4.5	225	20.1
PDM-32QAM	5.0	250	21.8
2048-SP-QAM	5.5	275	23.1
PDM-64QAM	6.0	300	24.7

based on $\mathbb{Z}^4$, i.e. PDM-*M*QAM. Therefore, with such a 2-way partitions chain, it is possible to construct signal constellations based alternately on $\mathbb{Z}^4$ and D_4. Monte Carlo simulations are performed to estimate the BER performance of some *M*-SP-QAM formats with their counterpart PDM-*M*QAM in AWGN channel at the same symbol rate of 28 GBd. The results are shown in Fig. 3.7. It can be seen that the sensitivity improvement of *M*-SP-QAM formats over corresponding higher order PDM-*M*QAM increases gradually as the OSNR increases. For example, 128-SP-QAM, 512-SP-QAM and 2048-SP-QAM offer a ~2.5 dB sensitivity gain at BER= 10^{-6} compared with PDM-16QAM, PDM-32QAM and PDM-64QAM, at the expense of 0.5 bit/sym/pol in SE , respectively. The sensitivity gain, however, is reduced to ~1.5 dB at BER= 10^{-2}.

The ROSNR for selected *M*-SP-QAM and the corresponding PDM-*M*QAM formats at HD-FEC limit of BER= 3.8×10^{-3} is given in Table 3-1. All modulation formats are operating at fixed symbol rate of 28 GBd and the information bit rates are calculated assuming a total overhead of 12% for the protocol and HD-FEC. It can be noted that for PDM-*M*QAM formats, it is only possible to increase the SE by a step of 1 bit/sym/pol, where each step requires ~2.5 – 4 dB additional OSNR. Nevertheless, finer granularity of 0.5 bit/sym/pol in SE can be provided if the *M*-SP-QAM formats are also considered. The *M*-SP-QAM serves as an intermediate step between PDM-*M*QAM formats. This enables a smooth transition in information bit rate with a step of 25 Gb/s, where each increment takes ~1 – 2 dB extra OSNR.

An important aspect of the *M*-SP-QAM formats is that they can be implemented using the same hardware as conventional PDM-*M*QAM formats with some minor modifications for the DSP part. Accordingly, transceiver which supports standard PDM-*M*QAM in addition to *M*-SP-QAM formats provides wide range of possible spectral efficiencies. Thus, it enables a very good tradeoff between bit rate and transmission reach [32]. The latter feature is essential for designing cost-efficient flexible optical transceivers, which is considered as a key building block of the software defined optical networks (SDON) [162, 163].

A bit-to-symbol mapping rule for 32-SP-QAM and 128-SPQAM was described in [164] and for 512-SP-QAM and 2048-SP-QAM in [165, 166]. It was shown that this function can be realized using only few XOR logical gates. The symbol decision function can be efficiently implemented as

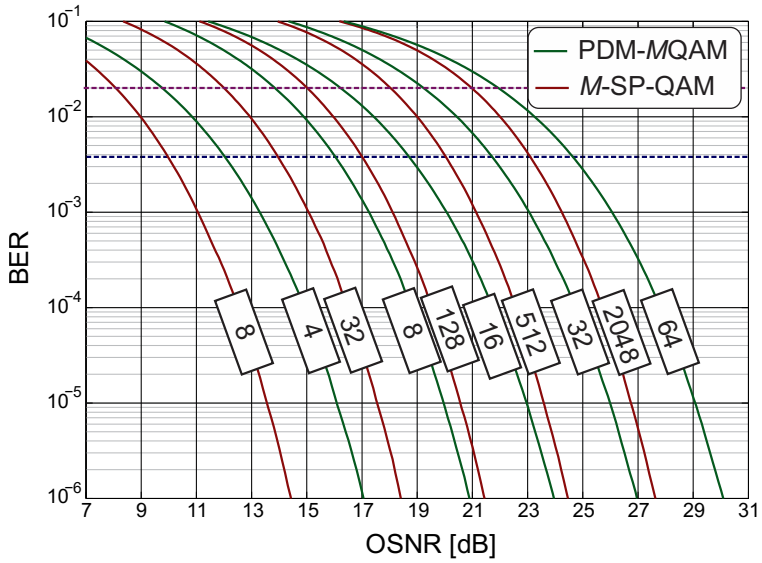

Fig. 3.7: BER versus OSNR for selected *M*-SP-QAM (red lines) and PDM-MQAM formats (green lines) in AWGN channel transmitting at the same symbol rate of 28 GBd. For each modulation format, the constellation size *M* is labeled on the corresponding curve

described in [167] which can be applied for any modulation format based on a lattice, including *M*-SP-QAM formats, this algorithm was adopted for 128-SP-QAM in [168].

Numerical simulations and experimental investigationsk were carried out by different groups to evaluate the performance of *M*-SP-QAM formats for both uncoded and coded systems.

The 32-SP-QAM and 128-SP-QAM formats were first proposed and analyzed by numerical simulation in [161]. Following, 128-SP-QAM was compared numerically with PDM-16QAM in both single channel and WDM transmission system [168]. Later, the same group demonstrated the 128-SP-QAM experimentally and compared it with PDM-16QAM at symbol rates of 10 Gbd and 12.5 Gbd in b2b and in WDM transmission system [169]. It was shown that the 128-SP-QAM format offers a b2b sensitivity gain of 1.9 dB over PDM-16QAM compared at the same bitrate of 84 Gb/s and assuming a pre-FEC threshold of BER= 10^{-3} . For the WDM transmission scenario, the 128-SP-QAM was able to extend the transmission reach of PDM-16QAM from 1300 km to 1990 km at the same bitrate of 84 Gb/s. Another experimental investigation of 32-SP-QAM and 128-SP-QAM was reported in [170], the two formats were compared with PDM-16QAM at the same symbol rate of 28 Gbd in Nyquist-WDM (NWDM) transmission system with 33 GHz channel spacing. The measured transmission reach at the HD-FEC threshold were 8400 km, 4200 km and 2400 km for 32-SP-QAM, 128-SP-QAM and PDM-16QAM, respectively.

Flexible optical transceiver based on 128-SP-QAM, 512-SP-QAM and 2048-SP-QAM and the corresponding PDM-*M*QAM format was experimentally demonstrated in [166]. In this experiment, three NWDM super-channels are generated; each of them occupies a bandwidth of 200 GHz and is formed by multiplexing five wavelengths channels on a 35 GHz grid. It was shown that for a fixed symbol rate of 28 Gbd and assuming a 26% overhead for protocol and SD-FEC, the spectral efficiency can be tuned between 3.88 bit/s/Hz and 6.67 bit/s/Hz in a step of 0.56 bit/s/Hz. While the transmission reaches at BER= 2×10^{-2} can be adapted between 3600 km to 160 km.

In [171, 172], the 32-SP-QAM format was experimentally compared with another scheme named time-domain hybrid QPSK/8QAM, which is constructed by interleaving the QPSK and 8QAM symbols in the time-domain, so that in each of the two polarizations, 50% of transmitted symbols are QPSK and 50% are 8QAM. In this way, both 32-SP-QAM and hybrid QPSK/8QAM have the same SE of 2.5 bit/sym/pol. It was shown that the 32-SP-QAM offers a longer transmission reach compared with the hybrid QPSK/8QAM in a NWDM transmission system at 32 Gbd and 32.5 GHz channel spacing [171] and at 31.2 Gbd with 33 GHz channel spacing [172].

The *M*-SP-QAM formats combined with SD-FEC codes were also evaluated by many groups. The 32-SP-QAM and 128-SP-QAM formats were compared with PDM-QPSK and PDM-8QAM by numerical simulations in the presence LDPC code with different rates [164]. It was shown that the larger OH of 33.3% employed for the 128-SP-QAM enables a sensitivity improvement of 0.8 dB over PDM-8QAM with 12.5% OH compared at BER= 2×10^{-3} and at the same information bit rate of 150 Gb/s. Nevertheless, a negligible improvement of 0.1 dB was observed for 32-SP-QAM with 50% OH compared to PDM-QPSK with 12.5% OH at the same information bit rate of 100 Gb/s.

In [173], 128-SP-QAM was experimentally investigated in a coded system using an LDPC code with ~7.5% OH and iterative decoding. The signal was transmitted in a WDM system with 160 wavelength channels on a 20 GHz grid and a symbol rate of 16 Gbd. A total of ~16.7 Tb/s information data was transmitted over 6860 km and a capacity × distance record of 114.4 Pb/s·km was reported. Another experiment which deals with 128-SP-QAM in coded system was reported in [174], where the performance of 128-SP-QAM combined with two different SD-FEC codes, namely TPC and LDPC, was discussed.

Furthermore, higher-order *M*-SP-QAM formats were also checked in a coded system. Transmission experiments of 512-SP-QAM and 2048-SP-QAM in a NWDM system combined with TPC with 21.3% OH were presented in [165] and [175], respectively.

A form of time-domain hybrid scheme, denoted as Half 4D-16QAM, was proposed in [11, 12, 176]. In this scheme, half of the transmitted symbols are 128-SP-QAM and the other half are PDM-16QAM symbols. This scheme was experimentally demonstrated in a WDM transmission system. The symbol rate was set to 16.64 Gbd and the channel spacing to 17 GHz which results in a SE of 6.1 bits /s /Hz. An LDPC code with 20% was utilized with bit interleaving and iterative decoding. A total of 30 Tb/s information data was successfully transmitted using 294 channels over 6630 km [11] and over 7230 km [176]. The Half 4D-16QAM scheme was further analyzed in [12] with some parameters' modifications. The symbol rate was increased to 32 Gbd and the channel spacing to 33 GHz and the number of channels was reduced to 106. In addition, a NLC technique was used to compensate for nonlinear impairments. A total of 21.2 Tb/s information data was transmitted over 10290 km.

3.4.4 Other interesting 4-D formats

An optimized 4-D signal constellation, denoted by $C_{4,16}$, was studied in [158, 177, 178]. This signal has M= 16 points, i.e. SE= 2 bits/sym/pol, and presents a nominal coding gain of 1.11 dB. It has been experimentally evaluated by two independent groups [179, 180]. It was shown that the $C_{4,16}$ exhibits a sensitivity gain of over PDM-QPSK format compared at the same SER. However, the advantage of $C_{4,16}$ over PDM-QPSK would become insignificant when the BER performance is considered, especially at high BER limit as it was observed in [180].

Another interesting 4-D signal constellation with M= 256 points was proposed in [129, 181]. It can be constructed based on D_4 lattice. Therefore, it will be denoted as 256-D_4. This signal constellation has the same SE of 4 bits/sym/pol as PDM-16QAM but offers a nominal coding gain of 1.71 dB. Fig. 3.8 (a) shows the simulated b2b signal constellation for the 256-D_4 at OSNR of 25 dB, where the signal coordinates are given in [182]. It can be seen that not all signal points are equally likely. The probability of the signal points is reduced gradually as their energies increase. Therefore, the signal points with the least (most) energy are the most (least) probable, as illustrated in Fig. 3.8 (b). Such a non-uniform distribution of the signal points provides a shaping gain as described in [183]. Accordingly, the 256-D_4 has intrinsically a shaping gain due to the Gaussian-like distribution of its points.

The 256-D_4 signal was experimentally realized and compared with PDM-16QAM in [182]. The b2b

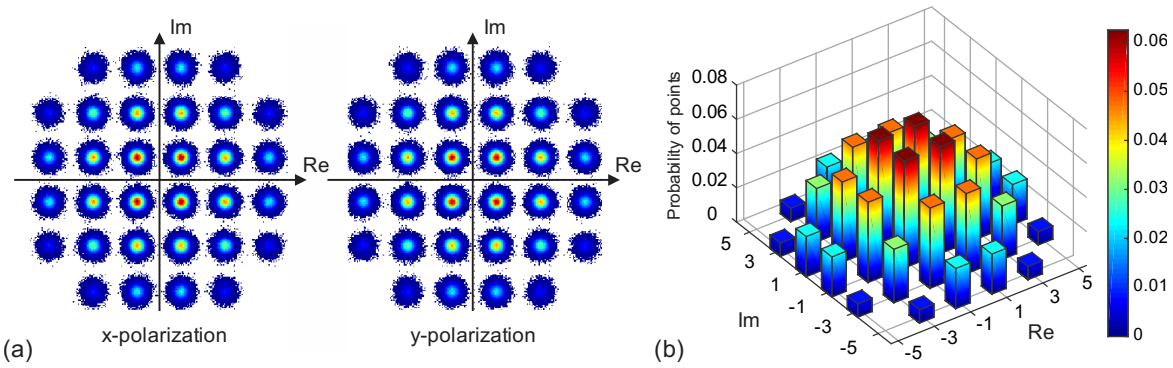

Fig. 3.8: (a) the simulated b2b signal constellation for 256-D_4 signal at an OSNR= 25 dB (b) propability of 256-D_4 signal points

experimental results shows that the 256-D_4 gives a sensitivity improvement of 0.9 dB compared with PDM-16QAM at BER= 10^{-6}. However, at a higher BER limit of 2×10^{-2}, it was observed that PDM-16QAM outperforms 256-D_4 by 1 dB, which can be attributed to the fact that the 256-D_4 is not gray-mapped. In addition, the average kissing number of 256-D_4 is 15.375, while it is only 6 for PDM-16QAM format.

Furthermore, two optimized 4-D signals with M=64 and 256 points were demonstrated in [184]. These formats, denoted by HC64 and HC256, introduce a nominal coding gain of 1.7 dB and 1.5 dB, respectively. Both formats were experimentally evaluated and compared with their equally spectrally efficient PDM-MQAM counterparts [184]. It was shown that HC64 offers a b2b sensitivity gain of 1.2 dB compared with PDM-8QAM at BER=3.8×10^{-3} after decoding using an LDPC code and ID technique, this sensitivity advantage of HC64 led to more than 15% increase in transmission reach over PDM-8QAM. In addition, it was shown that the HC256 was not able to extend the reach compared with PDM-16QAM, despite the slight sensitivity advantage of 0.3 dB which was measured in the b2b configuration.

3.5 Remarks and Discussion

- For the 4-D modulation formats considered in previous sections, it is not possible to apply a Gray-mapping rule. That means, a wrong decided symbol will not necessarily lead to only one single bit error, but it may result in multiple bit errors. As consequences, the probability of burst-error events increases and the performance in term of BER is degraded compared with SER. To overcome these problems, an outer HD-FEC code, which is particularly suited to deal with the burst error events, can be used, i.e. RS code, as it was discussed in [150, 156]. In addition, LDPC codes combined with ID technique was considered as valuable solution for anti-Gray mapped 4-D modulation formats [155, 157, 184].
- As discussed earlier, the number of nearest neighbors increases with the signal dimensionality. This factor limits the achievable coding gain especially at low-SNR regime. This explains why the sensitivity advantage of the 4-D over 2-D signal constellation becomes more visible at high SNR values, where the 4-D signals can reap the benefits of larger d_{min}. Accordingly, the 4-D signals are particularly suited for high SNR regime. As example, they can be combined with a simple HD-FEC code with low BER threshold as cost-efficient solution for metro optical transport networks.
- An interesting application scenario for the 4-D signal is the flexible optical transceivers. Transceivers that can support the optimized 4-D modulation formats in addition to the conventional 2-D PDM-MQAM formats, can provide a large variety of spectral efficiencies. Subsequently, reach can be simply traded against data rate, which is an important requirement for future optical network.
- It is worth to mention that the concept of lattice and its partitioning chain can be employed to construct coset codes [121, 185], including a trellis coded modulation (TCM) [115] and block coded modulation (BCM) [116, 122]. In the context of optical fiber communication, BCM based on dense lattices was studied and evaluated in [186-188] while the TCM will be discussed in details in the next chapter.

3.6 Digital signal processing for 4-D modulation formats

Some DSP functions for conventional 2-D formats may need to be modified to support the 4-D formats. In this section, the DSP functions related to specific 4-D modulation formats will be discussed.

For PS-QPSK format, some of the DSP functions used for PDM-QPSK need to be adjusted, namely, the time-domain equalizer (TDE) and the CPE. A modified version of constant modulus algorithm (CMA) used by the TDE was suggested in [189, 190]. While, for the CPE function, different algorithms were demonstrated, as it will be discussed in Section 3.6.1. For 6PolSK-QPSK formats, the main two functions which need to be modified are the time-domain equalizer, which will be discussed in Section 3.6.3, and the CPE functions, which will be discussed in Section 3.6.2.

3.6.1 CPE for PS-QSPK

The CPE for PS-QPSK was investigated by several groups. In [144, 191], the conventional 4-th power Viterbi-Viterbi algorithm [77] was applied in each polarization tributary independently. The same algorithm was also employed in [140, 192], preceded by a decision function block, which decide whether the QPSK symbol was transmitted in x- or y- polarization. This algorithm was also used in [193] followed by a phase ambiguity detector, which removes the uncertainty about the absolute phase of the PS-QPSK transmitted signal. A CPE which works jointly in both polarizations was considered in [139, 192]. However, the scheme described in [139] is more complex since it employs a two-stage phase recovery method based on test angles followed by a constellation-assisted maximum-likelihood CPE.

In [194], a joint-polarization CPE for PS-QPSK signal was investigated. The algorithm is based on 4-th power Viterbi-Viterbi algorithm and operates in both polarizations.

In the following sub-sections, the working principle of this algorithm will be described. In addition, its performance will be evaluated by numerical simulations and in a NWDM transmission experiment.

3.6.1.1 Principle of operation

The block diagram of the algorithm is illustrated in Fig. 3.9. The incoming complex sample sequences from the coherent polarization-phase diversity receiver at the input of the CPE unit are expressed as:

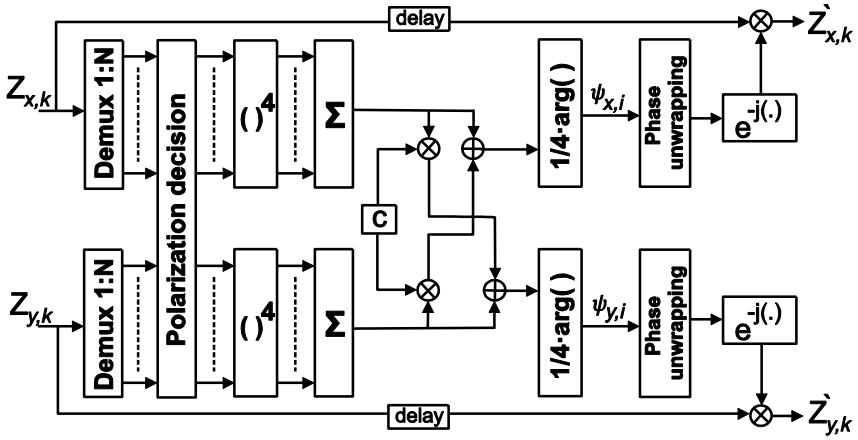

Fig. 3.9: Block diagram of the PS-QPSK joint-polarization carrier phase estimation. © IEEE 2012 [194], reprinted with permission.

$$Z_{p,k} = R\sqrt{P_{lo}P_s} \cdot A_{p,k} \cdot e^{j(\theta_{p,k}+\varphi_{p,k})} + n_{p,k} \tag{3-25}$$

where $p = [x, y]$ is the polarization component, k denotes the k-th sample, R is the responsivity of the photodiode, P_{lo} and P_s represent the average powers of local oscillator and signal respectively, $A_{p,k} \in \{0, 1\}$ and $\theta_{p,k} \in \{\pm\pi/4, \pm 3\pi/4\}$ are the signal information amplitude and phase respectively, $\varphi_{p,k}$ is the phase noise and $n_{p,k}$ represents the additive noise.

The samples $Z_{p,k}$ are first demultiplexed into blocks with N samples per block. Thus, a number of N samples will be processed in parallel. Although better phase noise tolerance may be obtained in some cases by using sliding window processing, only the more hardware-efficient block processing is considered here.

The samples are then fed into a polarization decision block, which compares the amplitude of samples from both polarizations. It decides in favor of samples having larger amplitude and suppresses the amplitude of the samples in the orthogonal polarization to zero [139, 140]. In other words, it is used to determine whether the QPSK symbol was transmitted in x-polarization or in y-polarization. Afterwards, the decided symbols $\tilde{Z}_{p,k}$ are raised to the 4th power in order to remove the QPSK modulation. Averaging over N samples is then performed in order to mitigate the influence of additive noise, such as e.g. amplified spontaneous emission (ASE) noise.

Both polarizations are contaminated by the same laser phase noise. Therefore, the phase noise in x- and y-polarization is highly correlated in the absence of nonlinear impairments. Consequently, coupling the phase noise information between both polarizations can enhance the performance of the algorithm [195]. The phase noise in both polarizations is coupled after being weighted by a coupling factor C ∈ [0, 1]. Setting C=0 results in no coupling [144, 191], and C=1 results in identical phase noise estimates in both polarizations [192].

The phase of the resulting signal after coupling is then divided by four, resulting in the phase noise estimates for x- and y-polarization ψ_x, ψ_y for the i-th block:

$$\begin{aligned} \psi_{x,i} &= \frac{1}{4}\arg\left[\sum_{q=1}^{N} \tilde{Z}_{x,k}^4 + C \cdot \tilde{Z}_{y,k}^4\right] \\ \psi_{y,i} &= \frac{1}{4}\arg\left[\sum_{q=1}^{N} \tilde{Z}_{y,k}^4 + C \cdot \tilde{Z}_{x,k}^4\right] \end{aligned} \tag{3-26}$$

Where $k = q + (i-1)N$, $q \in \{1, 2, \ldots N\}$, in the i-th block.

The phase noise estimates ψ_x and ψ_y lie inside the interval between -π/4 and π/4 due to the argument function. Phase unwrapping is applied in order to restore the original phase noise trajectory. After that, the estimated phase noise is used to correct the phase of the received symbols in the corresponding block.

3.6.1.2 Simulation results

The PS-QPSK transmitter was modeled based on a conventional PDM-QPSK transmitter with two extra XOR gates as described in [120]. A 112 Gb/s PS-QPSK signal is generated using three pseudo-random binary sequences of length 2^{16}. The resulting electrical signals are then used to drive two I/Q-modulators, one for each polarization. The modulated optical signal is shaped by a 2nd order Gaussian optical filter of bandwidth twice the symbol rate. At the receiver side, a polarization diversity coherent receiver with a DSP unit is used. The received optical signal is split into two orthogonal polarization components and interfered with local oscillator (LO) light by two 90˚ optical hybrids. The LO frequency matches the frequency of the transmitter laser. The outputs

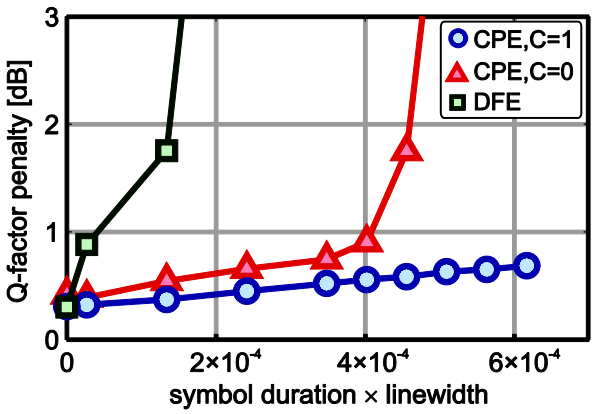

Fig. 3.10: Q-factor penalty for carrier phase estimation with (C=1) and without joint-polarization operation (C=0). For comparison, results obtained with a decision feedback equalizer are also reported. © IEEE 2012 [194], reprinted with permission.

of the optical hybrids are then detected by four balanced detectors and then passed through 5th order Bessel electrical low pass filters. Finally, the signals are down-sampled by four ADCs to twice the symbol rate and fed into the DSP unit.

To evaluate the tolerance against laser phase noise, the Q-factor penalty as a function of the (symbol-duration × linewidth) product was obtained for three different approaches, as shown in Fig. 3.10. The symbols are simulation results. Circles and triangles refer to the CPE with full coupling (C= 1) and without coupling (C= 0), respectively. The averaging length N was optimized for each simulation run by a trade-off between phase tracking and averaging of the additive Gaussian noise. For comparison, we also report the phase noise tolerance of an adaptive 2×2 decision-feedback equalizer (DFE) whose filter tap coefficients are adapted using a decision-directed least-mean square criterion [51]. For each case, the step width for the filter update was optimized. In that case no additional carrier phase estimation was performed. The simulations were performed for an OSNR of 13 dB. The Q-factor penalties were calculated with respect to the theoretical noise-limited Q-factor obtained for zero laser linewidth. This reference Q-factor is ~10.6 dB [130].

Clearly, both CPE algorithms show better tolerance against laser phase noise compared to the DFE. Furthermore, it can be noticed that the joint-polarization operation improved the algorithm performance and lower penalties were induced. For 112 Gb/s PS-QPSK signals and a Q-factor penalty of ≤ 0.5 dB, the maximum tolerable combined laser linewidth is ≈5 MHz for C=0 and ≈13 MHz for C=1. In order to examine the CPE algorithm robustness against cycle slips, we evaluated 62 million symbols for C = (0,1) at the same OSNR of 13 dB for a bit rate 112 Gb/s. Signal and LO laser each have a linewidth of 5 MHz. The number of induced cycle slips was counted to estimate the cycle slip probability. The observed cycle slip probability per symbol is approximately 5×10^{-6} for C=0 and approximately 8×10^{-8} for C=1, i.e. the joint-polarization operation reduces the probability of cycle slip events by about two orders of magnitude.

3.6.1.3 Experimental results

In order to evaluate the performance of the CPE algorithm in the presence of nonlinear impairments, the samples obtained from two transmission experiments were reprocessed. A single channel PS-QPSK experiment [142] as well as a NWDM PS-QPSK experiment [196]. Fig. 3.11 shows the Q-factor obtained from measured values of the BER as a function of transmitted distance

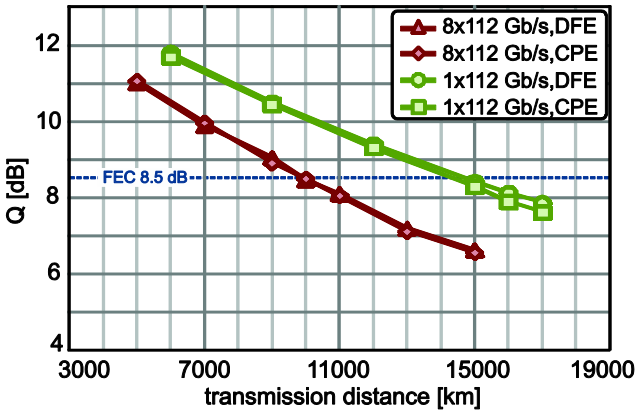

Fig. 3.11: Q-factor as a function of transmitted distance for 112 Gb/s PS-QPSK signals. Shown are results obtained with the joint-polarization CPE (C=1) and with a DFE. © IEEE 2012 [194], reprinted with permission.

for 112 Gb/s PS-QPSK signals. We consider single channel transmission and NWDM transmission with 40 GHz channel spacing. The launch power per channel is 0 dBm. Transmitter laser and LO laser each have a linewidth of approximately 100 kHz (corresponding to the leftmost point in Fig. 3.10). Two different approaches were implemented for the carrier phase recovery: the DFE and the CPE algorithm. For the CPE algorithm, the averaging length N was optimized at each transmission distance. It can be observed that both approaches have virtually the same performance for such narrow laser linewidth. However, The CPE does not require a feedback path, making it a preferable choice for simple integration in a parallel DSP architecture. Previous investigations have revealed severe penalties when using a feed-forward joint-polarization CPE in the presence of cross-phase modulation induced by on-off keying neighbors in dispersion-managed links [195]. However, in uncompensated transmission, the nonlinear distortions can be assumed as Gaussian distributed in inphase and quadrature component [197], i.e. they can be viewed as additive noise.

The CPE algorithm has two essential parameters: the averaging length N and the coupling factor C. In principle, a larger N can better minimize the ASE noise impact. Therefore, it is preferable in case ASE noise is the dominant impairment. However, a smaller N can better follow the phase varying. Thus, it is better for relatively broad laser linewidth or in presence of channel nonlinearity like cross phase modulation (XPM). In addition, the optimum coupling factor depends on the nonlinear channel impairments and on the XPM induced by neighboring channels [195]. The interplay between the filter taps N and the coupling factor C as a contour plot is presented in

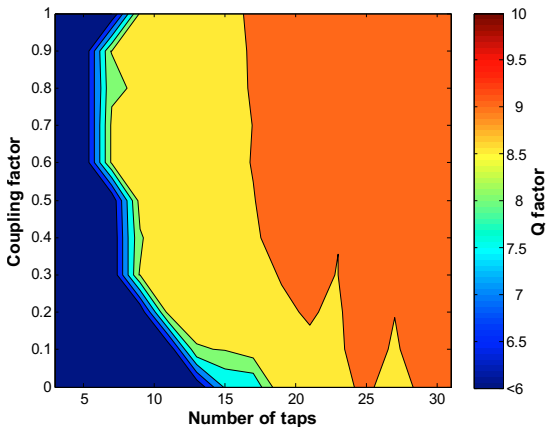

Fig. 3.12: Q-factor vs. the coupling factor C and the number of filter taps that used for averaging process N, for 8×112 Gb/s NWDM PS-QPSK after transmission over 9000 km at a launched power of 0 dBm.

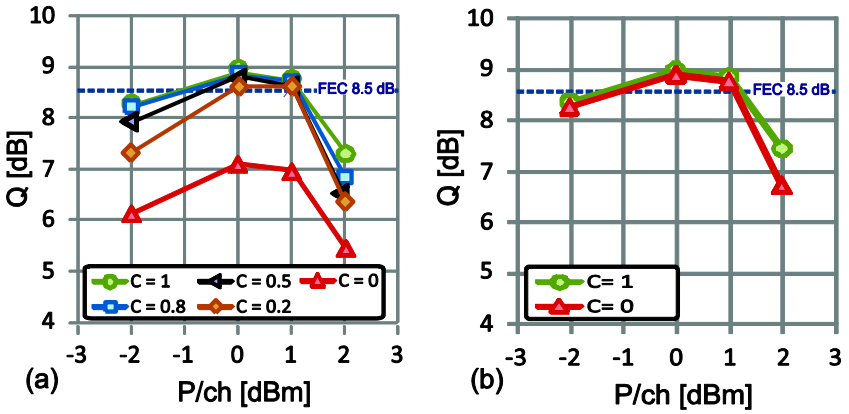

Fig. 3.13: Q-factor vs. fiber launch power per channel after 8×112-Gb/s NWDM PS-QPSK transmission over 9000 km ULAF using joint- (C=1) and single-polarization (C=0) CPE for (a) N= 15, (b) N=25. © IEEE 2012 [194], reprinted with permission.

Fig. 3.12. The figure shows a contour plot of Q-factor (in dB) versus the C and N used for the 112 Gb/s NWDM PS-QPSK after transmission over 9000 km at a launch power of 0 dBm. It can be observed that for constant values of C, more filter taps yield a better performance, that is because the transmitter and LO lasers had a narrow linewidth and thus the link is additive noise-limited, e.g. a 0.6 dB Q-factor improvement can be attained by increasing N form 7 to 17 taps for C= 0.8. Also, it can be seen that coupling the phase noise information between the two polarization components call for fewer taps at a fixed averaging length, e.g. for N=17 taps, a Q-factor of 7.53 dB is obtained for C=0 compared with 9 dB for C=1.

Finally, in order to investigate the impact of nonlinear distortions on the performance of the joint-polarization CPE, we compare the obtained Q-factor as a function of channel launch power after NWDM transmission over 9000 km ULAF for different coupling factors. Fig. 3.13 shows the Q-factor for an averaging length of (a) N=15 taps and (b) N=25 taps. It can be observed in Fig. 3.13(a) that for N=15, the joint-polarization approach improves the performance significantly already at small coupling factors compared with the single-polarization approach. The reason is that after polarization decision is performed, on average only half of the samples within each block can be used for phase estimation in each polarization due to the polarization switching. Therefore, coupling the phase noise information between two polarization tributaries will improve the averaging process to mitigate the influence of additive noise and thus improves the algorithm performance. Contrary to dispersion managed systems as described in [195], the optimum performance is obtained at maximum coupling factor. Fig. 3.13(b) shows the performance for larger averaging length N=25 taps. In this case, the performance is virtually independent of the coupling factor, since there are enough filter taps to suppress the additive noise.

3.6.2 CPE for 6PolSK-QPSK

It was discussed in Section 3.4.2, that the 6PolSK-QPSK signal constellation is made up of two subsets, the PDM-QPSK and PS-QPSK. Therefore, the 6PolSK-QPSK signal has eight phase states as it can be seen in Fig. 3.5 (a). Therefore, in order to remove the phase modulation, the 4-th power Viterbi-Viterbi algorithm can be modified and the received complex samples are raised to the power of 8 instead, as it was mentioned in [153]. Alternatively, the CPE can be performed after partitioning the 6PolSK-QPSK to its two subsets [198]. The principle of operation of this algorithm will be described in the following.

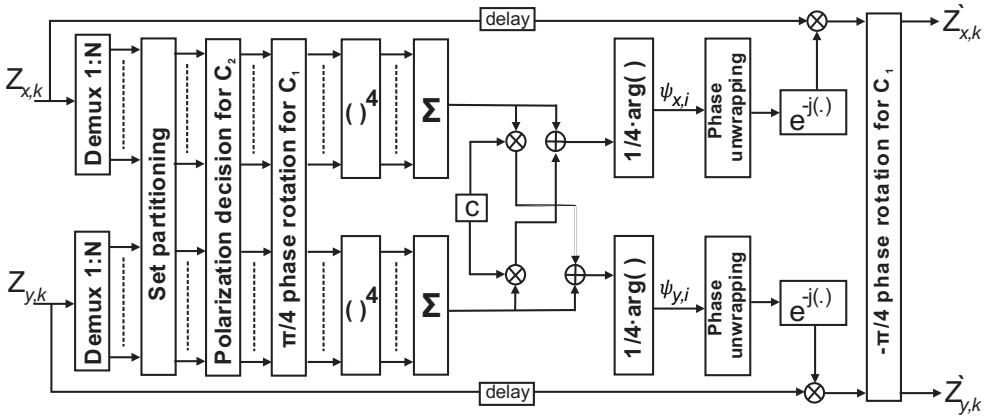

Fig. 3.14: Block diagram of the 6PolSK-QPSK joint-polarization CPE

The block diagram for the CPE algorithm for 6PolSK-QPSK signal is shown in Fig. 3.14. The complex sample sequences $Z_{p,k}$ at the input of the CPE unit are given in Equation (3-26), where $p = [x, y]$ is the polarization component and the index k indicates the k-th sample. It can be found from equations (3-21), (3-23) and (3-24) that the 6PolSK-QPSK signal has in each polarization eight phase states $\theta = m\pi/4$ with $m \in \{0,1,2, \dots ,7\}$ and three amplitude states $S \in \{0, 1, \sqrt{2}\}$.
The samples $Z_{p,k}$ are first demultiplexed into blocks of N samples and then classified into two groups using a set partitioning unit. This unit first calculates the received sample amplitude in each polarization, $|Z_{x,k}|$ and $|Z_{y,k}|$, then it computes the amplitude differences between the k-th sample and the reference amplitude levels in x-polarization $v_{x,l} = \left(|Z_{x,k}| - S_{x,l}\right)^2$ and in y-polarization $v_{y,l} = \left(|Z_{y,k}| - S_{y,l}\right)^2$, where $S_{x,l} = \{0, \sqrt{2}, 1\}$ and $S_{y,l} = \{\sqrt{2}, 0, 1\}$ with $l = [1, 2, 3]$, respectively. The received k-th sample is assigned to PDM-QPSK subset if $v_{x,3}$ and $v_{y,3}$ were the minimum, whereas it is assigned to PS-QPSK subset if either $v_{x,1}$ and $v_{y,1}$ or $v_{x,2}$ and $v_{y,2}$ were the minimum. Afterwards, a polarization decision is performed on the samples belonging to PS-QPSK subset as described in Section 3.6.1. These samples are then rotated by 45° to make them aligned with the PDM-QPSK subset. All samples are then raised to the 4-th power to remove the phase modulation. Alternatively, the samples from both subsets can be directly raised to the 8-th power without the need for the 45° phase rotation [153]. The phase noise in x- and y-polarization are then estimated according to Equation(3-26). After the phase unwrapping process, the estimated phase noise are used to derotate the received samples. Finally, the samples belonging to PS-QPSK subset are rotated back by 45°.

3.6.3 Adaptive equalizer for 6PolSK-QPSK

An algorithm for adaptive equalization for 6PolSK-QPSK signal was demonstrated in [153]. It is based on the fact that 6PolSK-QPSK signal can be separated in two subsets, the $\mathcal{C}_1 = \mathcal{C}_{PDM-QPSK}$ subset and $\mathcal{C}_2 = \grave{\mathcal{C}}_{PS-QPSK}$ subset. Therefore, a decision can be first made to determine whether the received 6PolSk-QPSK sample belongs to $\mathcal{C}_1$ or $\mathcal{C}_2$. Based on this decision, the appropriate cost function is chosen. Where the cost function employed therein, can be switched between PDM-QPSK mode and PS-QPSK mode, as described in [189].

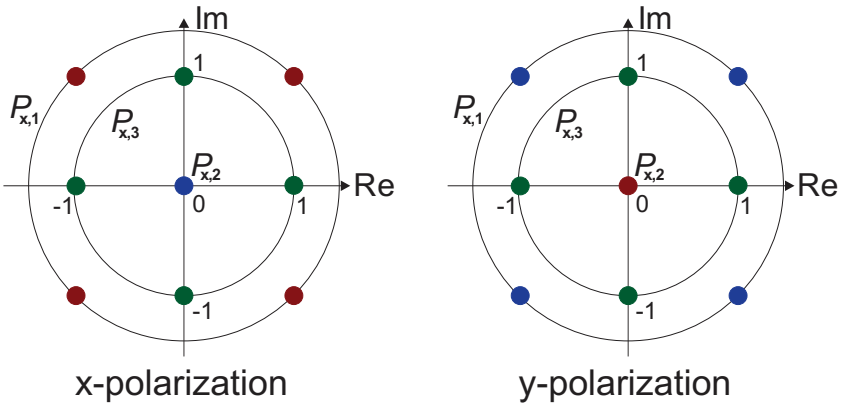

Fig. 3.15: 6PolSK-QPSK signal constellation diagram with the reference power levels in both polarizations.

A different algorithm for 6PolSK-QPSK equalization was proposed in [199]. The proposed cost function as well as a method for filter-taps initialization will be described in the following subsections.

3.6.3.1 Principle of operation

The algorithm attempts to minimize the following error criteria in both polarizations:

$$\begin{aligned} {\varepsilon_x}^2 &= (P_x - |x_{out}|^2)^2 \\ {\varepsilon_y}^2 &= (P_y - |y_{out}|^2)^2, \end{aligned} \tag{3-27}$$

where P_x and P_y are the constellation power levels in x- and y-polarization and $(P_x, P_y) \in \{(2,0), (0,2), (1,1)\}$ as illustrated in Fig. 3.15. The quantities x_{out} and y_{out} are the TDE output signals in x- and y-polarization, respectively.

In order to decide whether a processed symbol belongs to subset $\mathcal{C}_1$ or $\mathcal{C}_2$, the joint error in both polarizations is calculated for all three possible values of (P_x, P_y):

$$\nu_n = {\varepsilon_{x,n}}^2 + {\varepsilon_{y,n}}^2 = \left(P_{x,n} - |x_{out}|^2\right)^2 + \left(P_{y,n} - |y_{out}|^2\right)^2, \tag{3-28}$$

with $n = 1,2,3$. It follows that

$$(P_x, P_y) = \begin{cases} (2,0) \text{ if } \nu_1 \leq \nu_2 \wedge \nu_1 < \nu_3 \\ (0,2) \text{ if } \nu_2 < \nu_1 \wedge \nu_2 < \nu_3 \\ (1,1) \text{ if } \nu_3 \leq \nu_1 \wedge \nu_3 \leq \nu_2 \end{cases} \tag{3-29}$$

The outputs of the TDE x_{out} and y_{out} are given by:

$$\begin{aligned} x_{out} &= {\boldsymbol{w}_{xx}}^H \boldsymbol{x}_{in} + {\boldsymbol{w}_{xy}}^H \boldsymbol{y}_{in} \\ y_{out} &= {\boldsymbol{w}_{yx}}^H \boldsymbol{x}_{in} + {\boldsymbol{w}_{yy}}^H \boldsymbol{y}_{in} \end{aligned} \tag{3-30}$$

where $\boldsymbol{w}_{xx}, \boldsymbol{w}_{xy}, \boldsymbol{w}_{yx}, \boldsymbol{w}_{yy}$ are the equalizer tap weight vectors, with $\boldsymbol{x}_{in}$ and $\boldsymbol{y}_{in}$ denoting the equalizer input in x- and y-polarization, respectively. H denotes Hermitian transpose. The filter tap weights are updated using the least mean square algorithm [51] as follows:

$$\begin{aligned} \boldsymbol{w}_{xx} &= \boldsymbol{w}_{xx} + \mu \varepsilon_x \boldsymbol{x}_{in} {x_{out}}^* \\ \boldsymbol{w}_{xy} &= \boldsymbol{w}_{xy} + \mu \varepsilon_x \boldsymbol{y}_{in} {x_{out}}^* \end{aligned} \tag{3-31}$$

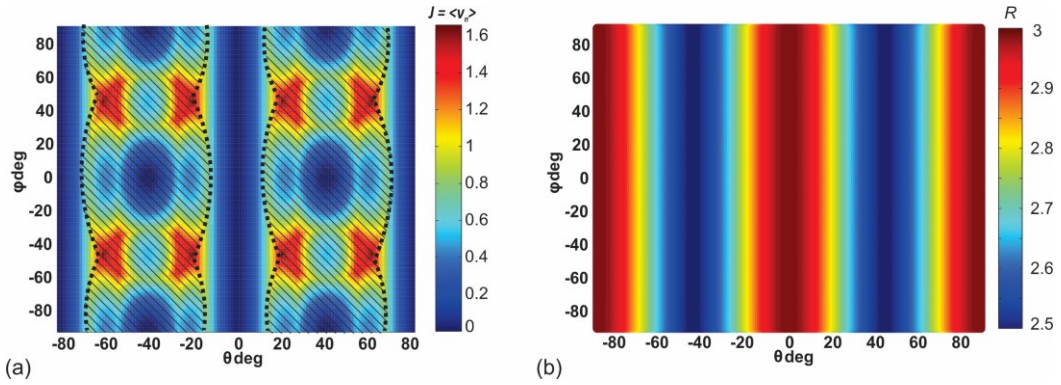

Fig. 3.16: (a) Control surface for a 6PolSK-QPSK signal. (b) The correlation between signal output powers as a function of polarization rotation angles.

$$\boldsymbol{w}_{yx} = \boldsymbol{w}_{yx} + \mu\varepsilon_y \boldsymbol{x}_{in} y_{out}{}^{*}$$
$$\boldsymbol{w}_{yy} = \boldsymbol{w}_{yy} + \mu\varepsilon_y \boldsymbol{y}_{in} y_{out}{}^{*}$$

Here, μ is the step size parameter. In order to assess the control surface of the equalizer, the cost function $J = \langle v_n \rangle$ was obtained by simulation. Assuming that the 6PolSK-QPSK signal $\boldsymbol{E}_{in} = (\boldsymbol{x}_1, \boldsymbol{y}_1)$ passed through a polarization rotation, the output signal can be written as

$$\boldsymbol{E}_{out} = (\boldsymbol{x}_2, \boldsymbol{y}_2)^T = M \cdot \boldsymbol{E}_{in}{}^{T} \tag{3-32}$$

With T stands for vector transpose, M is a Jones matrix given by:

$$M = \begin{pmatrix} \cos(\theta) & e^{j\varphi}\sin(\theta) \\ -e^{-j\varphi}\sin(\theta) & \cos(\theta) \end{pmatrix} \tag{3-33}$$

Both θ and φ were swept from –π/2 to π/2 with a step size of π/180.

As can be seen in Fig. 3.16(a), the cost function reveals local minima within the shaded area from which the equalizer may not be able to de-multiplex the two signal polarizations correctly. However, these undesirable cases can be avoided by proper initialization of the filter tap weights as we will show later. Using the bit-to-symbol mapping rule described in [130], 75% of the 6PolSK-QPSK symbols belong to the subset $\mathcal{C}_1$ and 25% of the symbols belong to the subset $\mathcal{C}_2$. By applying a unitary polarization rotation to the 6PolSK-QPSK signal as described in Equation.(3-33), the power exchange between the two polarization states will yield a conversion of symbols from $\mathcal{C}_1$ to $\mathcal{C}_2$, and vice versa .As a result, the correlation R between the powers of the two signal polarization outputs given in Equation (3-34) varies accordingly:

$$R = \langle |\boldsymbol{x}_2|^2 \cdot |\boldsymbol{y}_2|^2 \rangle \tag{3-34}$$

Fig. 3.16(b) shows the correlation R as a function of polarization rotation angles.

It is interesting to note, that this correlation is maximized for the correct symbol probabilities. In which, 75% of the 6PolSK-QPSK symbols belong to the subset $\mathcal{C}_1$ where the total signal power is equally distributed between the two polarizations and 25% of the symbols belong to the subset $\mathcal{C}_2$ where the signal total power is confined in one polarization and the other polarization contains noise only.

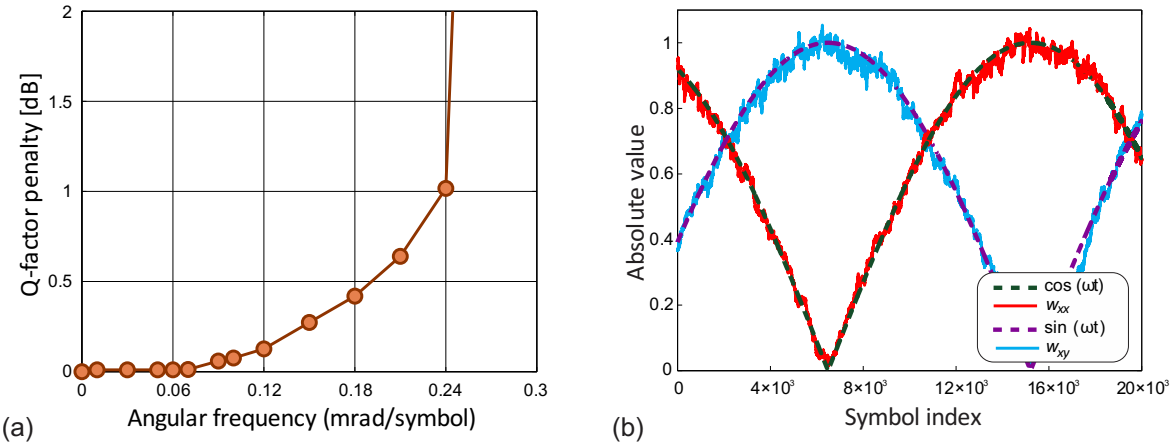

Fig. 3.17: Dynamical characteristic of the equlizer (a) Q-factor penalty as a function of angular frequency for μ= 10^{-3} (b) Tracking of endless polarization rotation for ω = 0.18 mrad per symbol with μ= 10^{-3}

The equalizer can take advantage of this property and initialize the central tap weights near the desired minima of the cost function, which can be obtained by finding the angular parameters θ and φ of the polarization rotation matrix M for which the correlation R is maximized:

$$[\theta_{opt}, \varphi_{opt}] = \arg\left(\max_{[\theta,\varphi]} R\right), \tag{3-35}$$

The central tap weights $\boldsymbol{w}$ are then initialized using the optimum angle values as following:

$$\begin{pmatrix} w_{xx}\, w_{xy} \\ w_{yx}\, w_{yy} \end{pmatrix} = \begin{pmatrix} \cos(\theta_{opt}) & e^{j\varphi_{opt}} \sin(\theta_{opt}) \\ -e^{-j\varphi_{opt}} \sin(\theta_{opt}) & \cos(\theta_{opt}) \end{pmatrix} \tag{3-36}$$

By this preconditioning, the TDE will converge to the correct output for arbitrary input SOP.

3.6.3.2 Simulation and Experimental results

To verify the capability of the proposed algorithm to track endless time-varying SOP, the transmitted signal is multiplied by a channel matrix $\boldsymbol{\mathcal{H}}$ given by:

$$\boldsymbol{\mathcal{H}} = \begin{pmatrix} \cos(\omega t) & \sin(\omega t) \\ -\sin(\omega t) & \cos(\omega t) \end{pmatrix} \tag{3-37}$$

Where ω is the angular frequency of the polarization rotation. The signal was noise loaded to an OSNR of 14 dB before it was multiplied by the channel matrix $\boldsymbol{\mathcal{H}}$ where ω was increased at a constant rate. Fig. 3.17(a) shows the Q-factor penalty as a function of ω for a step size parameter μ=10^{-3}. The TDE was able to track a varying SOP showing a Q-factor penalty below 1 dB for rotation frequencies up to 0.2 mrad/symbol. Fig. 3.17(b) shows an example of the filter adaptation for ω = 0.18 mrad/symbol.

In order to investigate the tolerance of the equalizer to polarization-dependent loss (PDL), the orientation of the signal polarizations was first modified according to Equation (3-33). The angle θ was swept from –π to π with a step size of π/180, whereas φ was set to zero. The signal was then applied to a PDL element. Afterwards the signal was rotated again to randomize the signal SOP at the receiver input. The signal was then noise loaded to an OSNR of 14 dB corresponding to a BER of 10^{-3} at a symbol rate of 28 GBd. As can be seen in Fig. 3.18(a), the TDE performs well in presence of PDL with a Q-factor penalty of less than 1 dB for PDL values up to 3 dB.

In order to examine the equalizer performance experimentally, the 6PolSK-QPSK signal samples obtained from a transmission experiment were reevaluated [154]. Fig. 3.18(b) shows the Q-factor as a function of transmission distance for two different equalizers, a data-aided frequency-domain equalizer (DA-FDE) [154] and the proposed TDE. For the TDE, an 11-tap T/2 filter was used for equalization, initialized with $\mu=10^{-4}$ and 5×10^{3} symbols. Both equalizers yield similar performance with the TDE slightly in the lead.

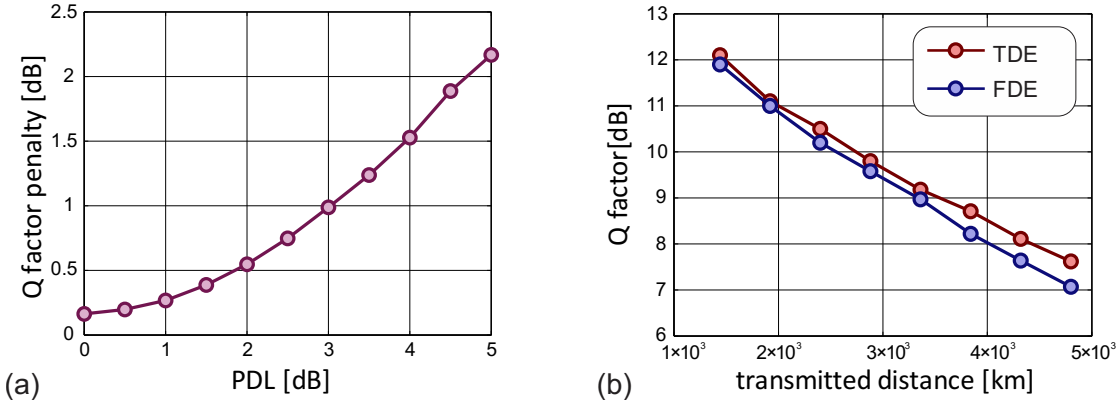

Fig. 3.18: (a) The averaged Q-factor penalty in presence of PDL (b) Q-factor versus transmitted distance

3.7 Author contribution related to this chapter

My contribution has focused on the DSP part for the 4-D modulation formats. In addition, I have support my colleague in some of the lab experiments.

For PS-QPSK format, I have implemented and evaluated a CPE algorithm for this format, the evaluation results were presented in [194] and in Section 3.6.1.

J. K. Fischer and I have proposed a CPE algorithm for 6PolSK-QPSK format, which was submitted as patent application [198]. I implemented the algorithm in Matlab and performed numerical simulations to evaluate this algorithm. In addition, I have proposed an algorithm for digital equalization of 6PolSK-QPSK format, the algorithm was evaluated by numerical simulation and by system experiment and the results were presented in [199] and in Section 3.6.3.

Moreover, together with T. Tanimura I investigated the 6PolSK-QPSK in presence of RS code and NLC. I have implemented the necessary DSP functions for 6PolSK-QPSK format, including the mapper, the CPE, the decision unit and the demapper. Furthermore, I impeded the RS and NLC codes to the DSP toolbox developed at Heinrich-Hertz-Institut (HHI), which was used in this experiment. C. Schmidt-Langhorst built the experimental setup and T. Tanimura and me performed the experiment. The results were published in [159]

I have carried out a numerical simulation study for 4-D modulation formats using VPItransmissionMaker™ Optical Systems software and the results were used in [32].

Finally, together with T. A. Eriksson I demonstrated an experimental study for 256-D_4 format. E. Agrell suggested the bit-to-symbol rule. I implemented the TPC functions and added the mapper, the demapper and decision functions for the 256-D_4 format to the DSP toolbox. C. Schmidt-Langhorst prepared the experimental setup. T. A. Eriksson and me executed the experiment and the result were published in [182]

CHAPTER 4

Trellis Coded Modulation for Optical Transmission System

This chapter discusses the benefit of combining coding and modulation, so-called coded modulation. Then, it introduces the concept of two-dimensional (2-D) and multidimensional (multi-D) trellis coded modulation (TCM). Afterwards, it reviews the different techniques used for partitioning the multi-D signal set, where an approach based on Multilevel coding (MLC) is described in detail. Finally, turbo TCM (TTCM) based on multi-D signal set is discussed.

4.1 Fundamentals of TCM

The FEC codes are based on the concept of adding a redundancy, in a controlled manner, to the information at the transmitter, and then try to detect and correct possible errors at the receiver side employing this redundancy. Accordingly, in order to maintain the same information transmission rate, either the symbol rate (i.e. the channel bandwidth) or the order of the modulation format should be increased. Until the mid-1970's, the redundancy of FEC codes was accommodated for by increasing the symbol rate (bandwidth expansion) when the target SE is smaller than 2 bits/symbol, while for larger required SEs, high-order modulations were used without coding. Since there was no practical coding scheme that could be implemented with high-order modulation format to offer adequate coding gain over solely uncoded modulation [123, 200].

Fig. 4.1 shows the SE as a function of SNR in AWGN channel for Gaussian input (i.e. Shannon capacity limit) and for some input modulation formats (i.e. constellation-constrained capacity), namely, QPSK, 8PSK and 16QAM. In addition, the require SNR to achieve a BER of 10^{-5} for uncoded case and some coded approaches obtained by numerical simulations are also depicted.

It can be seen that the required SNRs to transmit at SE of 2, 3, 4 bits/symbol are 12.6 dB, 17.7 dB and 19.5 dB corresponding to uncoded QPSK, 8PSK and 16QAM and the gaps to the Shannon capacity limit are 7.8 dB, 9.2 dB and 7.7 dB, respectively. Normally, FEC codes are employed to reduce these SNR requirements. Thus, in order to operate at SE= 2 bits/symbol, one option is to use 8PSK with rate-2/3 convolutional code. As it can be seen in Fig. 4.1, the results are not promising and no improvement is obtained even with a constrain length of v= 6 (corresponding to 64-state for Viterbi algorithm). Now, for SE= 3 bits/symbol, 16QAM is encoded with rate-3/4 convolutional encoder, it can be observed here, that while the code with v= 3 brings no advantage, the longer constrain length v= 6 enables an SNR reduction by more than 2 dB.

Another option for coded system which targets SE> 2 bits/symbol is to employ the BCH code with 8PSK and 16QAM formats. The results for two different codeword lengths of n= 63 and n= 255 are plotted in Fig. 4.1. It can be seen that for SE= 2 bits/symbol, the BCH code with n= 63 is completely useless, and a 1 dB improvement is only possible by longer codeword of n= 255. Moreover, for SE= 3 bits/symbol, the BCH with n= 63 performs similar to convolutional code with v= 6, and further improvement of 1 dB is enabled by switching to longer codeword of n= 255.

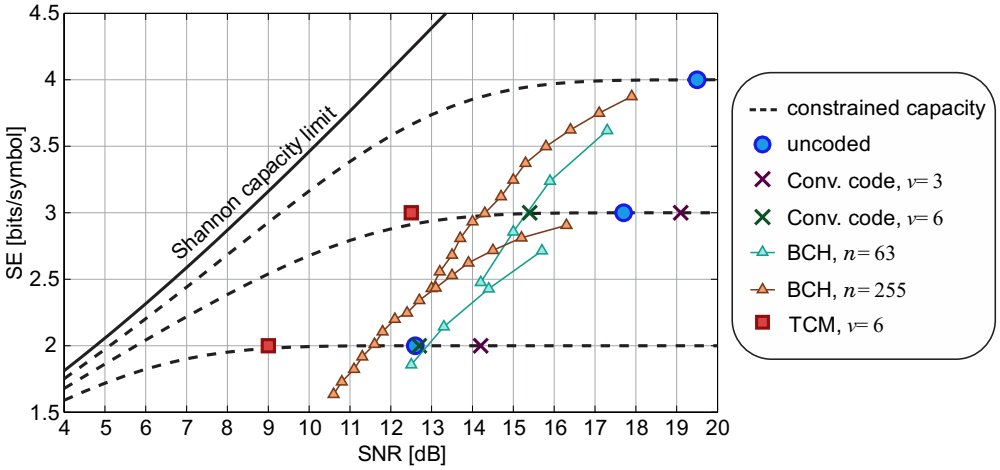

Fig. 4.1: Simulation results show the SEs as a function of SNR in AWGN channel for Gaussian input as well as for some input modulation formats. The required SNR at a BER of 10^{-5} for some uncoded and coded modulation formats in an AWGN channel is also shown. The results includes: uncoded QPSK, 8PSK, 16QAM (blue circles), 8PSK and 16QAM combined with: 1- convolutional code with 8-state (violet cross) and 64-state (green cross), 2- BCH code with n= 63 (turquoise triangles) and n= 255 (brown triangles), 3- TCM with 64-state (red squares).

Nevertheless, none of these coding schemes were good enough to be adopted in practical systems, since the required hardware complexity does not pay off in term of delivered coding gain.

The remarkable progress in the coding field for this regime (i.e. SE> 2 bits/symbol) was made by Ungerboeck [160, 201], who suggested that coding and mapping functions could be design jointly to improve the system performance, this technique is referred to as *coded modulation*. The idea was to combine a convolutional code with an appropriate signal mapping, so called trellis coded modulation (TCM). Fig. 4.1 depicts the results obtained by employing TCM with 8PSK and 16QAM, both with constrain length of v= 6, to operate at SE= 2, 3 bits/symbol, respectively. It can be clearly seen that the TCM scheme outperforms the previous coding scenarios and reduces the gap to the Shannon limit to about 4 dB.

The performance of a coded transmission system is governed by the minimum free Euclidian distance (d_{free}) between signal sequences, unlike classical error correction codes where the hamming distance between codewords dominates the error rate performance [202].

Recalling from Section 3.2, the symbol error probability on an AWGN channel for uncoded system is given in Equation (3-10). Similarly, the *events error probability* for coded system P_e can be upper bounded by [200, p. 957]:

$$P_e \leq K_{d_{free}} \, \mathrm{Q}\left(\sqrt{\frac{d_{free}^2}{2N_0}}\right) \tag{4-1}$$

Where $K_{d_{free}}$ represent the number of nearest neighbor signal sequences at a minimum distance d_{free} from a given coded sequence and Q-function is defined in equation (3-11). The Viterbi algorithm [203] is usually used to perform maximum-likelihood sequence decoding. That is, it finds the closest symbols sequence on the trellis to the received symbol sequence in term of squared Euclidian distance. The error event happens when the decoded symbol is differed from the transmitted one.

Ungerboeck [160] has made an interesting observation that by combining the coding and the mapping functions, performance improvement is attainable. To this end, the uncoded signal constellation Ω is expanded, typically by factor of 2, to a larger signal constellation Ὼ. Then, by a judicious choice of bit-to-symbol mapping together with an appropriate convolutional encoder, a coding gain is achieved by making the d_{free} of a coded system based on Ὼ larger than the d_{min} of an uncoded system based on Ω. The distance coding gain is then $\gamma_d = {d_{free}}^2/{d_{min}}^2$.

The signal set expansion is mandatory to keep the transmission rate unchanged without increasing the required bandwidth for transmission. Nevertheless, the expanded signal constellation Ὼ imposes an increase in the average signal energy compared with the smaller signal constellation Ω at the same minimum distance. In this case, an energy loss of $\gamma_e = \mathrm{E}_\Omega/\mathrm{E}_{\grave{\Omega}}$ is inevitable. Then, the asymptotic coding gain for TCM system is given as [200, p. 958]:

$$\gamma_{TCM} = \gamma_d \cdot \gamma_e = \frac{{d_{free}}^2}{{d_{min}}^2} \cdot \frac{\mathrm{E}_\Omega}{\mathrm{E}_{\grave{\Omega}}} \tag{4-2}$$

A standard textbook example for TCM is the partitioning of 8PSK signal set, which will be described briefly in the following as a proof of concept.

The 8PSK signal set is successively divided into smaller subsets as shown in Fig. 4.2, where the minimum Euclidian distance between points within each subset, referred to as minimum subset distance (MSD) δ_p, is increased progressively at each partitioning level p. Now, consider the TCM scheme for 8PSK signal shown in Fig. 4.3, it consists of convolutional encoder and signal mapper. The convolutional encoder is a rate R=1/2 systematic encoder, it has two delay elements and one Exclusive-OR (XOR) gate. One information bit b_0 entered at a time, which is replicated at the output of the encoder, hence the name systematic. The two encoded bits are then used to select one of the four subsets at the partitioning level p= 2, while the remaining uncoded bit b_1 is used to select one of the two points within the subset.

The 4-state trellis diagram corresponding to the encoder is depicted in Fig. 4.3(b), the encoder states are presented in the decimal form inside the circles. There are two branches diverging from each state, corresponding to the information bit which enters the encoder. However, since the coded system involves one uncoded bit, the trellis representation should be modified to include this

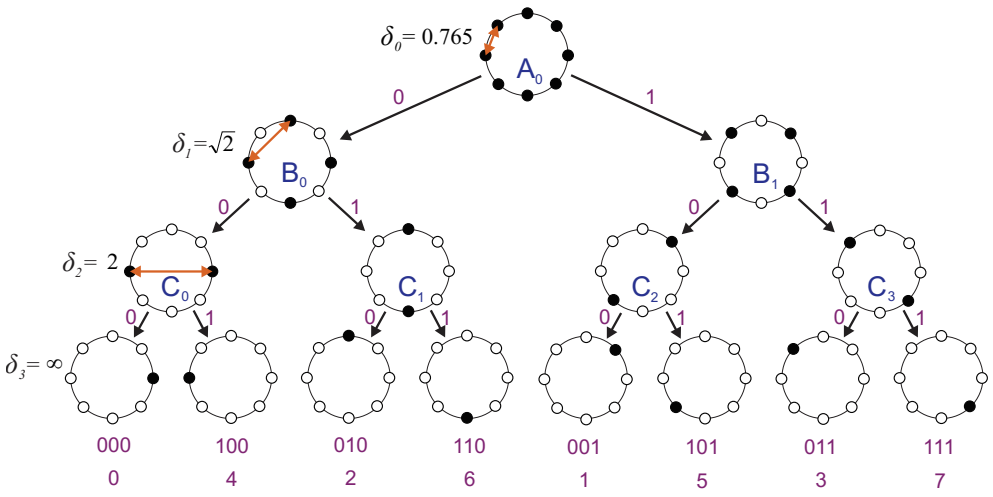

Fig. 4.2: Partitioning of 8PSK signal set

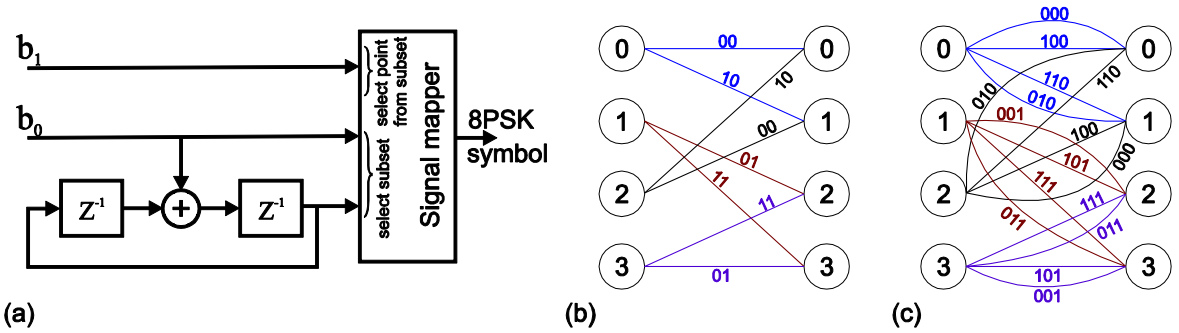

Fig. 4.3: The 8PSK-TCM coded system (a) R=1/2, 4-state systematic convolutional encoder with a signal mapper (b) the trellis diagram for the convolutional encoder (c) the complete trellis diagram which includes the parallel transitions corresponding to the uncoded bit b_1

bit. Fig. 4.3 (c) shows the modified trellis after adding the *parallel transitions* corresponding to the uncoded bit.

At this point, it is can be easily found that the d_{free} for the 4-state 8PSK TCM equals to 2 [204, 205, p.537-542]. Therefore, from Equation (4-2), the asymptotic coding gain over the uncoded QPSK with $d_{min} = \sqrt{2}$ is $\gamma_{TCM} = \gamma_d = 3.01$ dB, where $\gamma_e = 1$ since the average energies of the coded and uncoded formats are normalized to one. Fig. 4.4 shows the BER performance as a function of SNR for 4-state 8PSK TCM and for uncoded QPSK, both have a SE of 2 bits/symbol. The results are obtained by numerical simulations in an AWGN channel. It can be noted that the coded scheme offers a coding gain of ~2.3 dB over QPSK at BER= 10^{-5}. The coding gain can be further enhanced by ~1.2 dB via increasing the number of encoder's state to 64 as it was shown in Fig. 4.1.

In order to design a good TCM system, there are three rules which should be considered [204]:

- The parallel transitions, corresponding to uncoded bits, should be assigned to the signal points separated by the maximum Euclidian distance.
- The Euclidian distance between adjacent transitions on the trellis should be maximized. There are transitions that start and end at the same state.
- All signal points should be used equally often.

Ungerboeck [206] has proposed a practical technique to address these requirements, which is called *mapping by set partitioning*. It provides a mean to assign binary labels to the signal points, in order to assist the process of designing good TCM. The concept of this technique is illustrated in Fig. 4.2

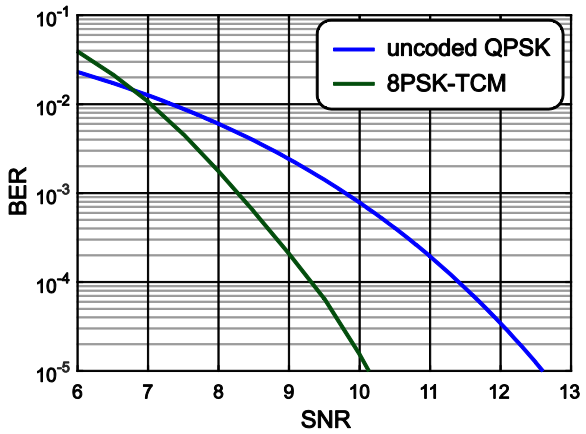

Fig. 4.4: BER as a function of SNR for uncoded QPSK format and for R=1/2, 4-state 8PSK-TCM format

for 8PSK signal set. At the first level of partitioning, the 8 points signal set, denoted as A_0, with $\delta_0 = 0.765$ is partitioned into two subsets B_0 and B_1, each has 4 signal points and a $\delta_1 = \sqrt{2}$. Then, the two subsets are divided into four subsets C_0, C_1, C_2 and C_3, where the distance between adjacent signal points within each subset is increased to $\delta_2 = 2$. The partitioning is then continued until only one signal point is left in each subset. The resultant binary labels with the signal number are indicated under each signal point at the lowest level of partitioning tree. It is interesting to note that the mapping leads to a naturally mapped 8PSK signal.

By this partitioning process, it is assured that each of the parallel transition pairs, namely (000, 100), (010, 110), (001, 101), (011, 111), are separated by $\delta_2 = 2$, which is the maximum possible Euclidian distance for a subset with two points. Therefore, the first condition for a good TCM code is fulfilled. Also, the state transition pairs leaving and entering the same state in the trellis, labeled as (00, 10), (01, 11), are originated from the same subset at p= 1. That is, $C_0 \cup C_1 = B_0$ and $C_2 \cup C_3 = B_1$. Since the signal points in B_0 and B_1 subsets are separated by at least $\delta_1 = \sqrt{2}$, which is the maximum possible distance for a subset with four points, hence the second condition is granted. Finally, it can be noted that the signal points are used with equal probability, since each signal point is represented by two state transitions in the trellis, which agrees with the last condition for constructing a good TCM scheme.

To achieve coding gain, the described mapping rule should be accompanied with a proper convolutional code. To this end, a code search algorithm is performed to find the optimal convolutional code for a given signal set and constrain length. The algorithm searches for those codes which maximize the d_{free} and then chooses the one which minimizes the $K_{d_{free}}$. Tables for the best 2-D TCM for various signal sets are presented in [160].

4.2 Multidimensional TCM

Shannon's channel coding theorem [89] says that the performance of transmission systems, operating at a rate R smaller than the capacity C, can be improved by increasing the code length n. That is, the error probability tends to zero as n tends to infinity. Geometrically, this is equivalent to increase the signal dimensionality in the Euclidean space to make the performance better.

In Chapter 3 we have described how the uncoded optimized 4-D signal sets offer a sensitivity improvement over 2-D signal sets. Now, we will consider the benefits of coded systems based on multidimensional (multi-D) signal sets, in particular, 4-D signal sets.

The multi-D signal set can be constructed from a 2-D signal set by time division approach. That is, $2L$-D signals with duration T can be generated by transmitting L 2-D signals over L consecutive time slots, each with duration $\tau = T/L$. In this way, the $2L$-D signal set is obtained by L-fold Cartesian product of the 2-D signal set [200]. Hence, the multi-D signal set will be referred to as $2L$-D signal set. According to this approach of constructing a multi-D signal set, the 4-D signal set is easily generated by letting L= 2 ,where two 2-D signal points are sent over two adjacent time slots. Alternatively, the 4-D signal set can be constructed by utilizing the two quadrature components (I and Q) of the two orthogonal polarizations of the electromagnetic field. The later approach is well suited for coherent optical receiver system [130, 137]. It is worth mentioning that the coding gain is only achieved by design the 4-D modulation format jointly over all dimensions rather than sending the information independently over each dimension.

The concept of 2-D TCM, which was presented in the previous section, can be extended to multi-D signal sets. That turns out to be a fruitful approach for the following reasons [200]:

- Flexibility: Multi-D TCM enables designing a transmission system with fractional values of spectral efficiencies.
- Rotational invariance: Multi-D TCM facilitates constructing schemes which are fully transparent to the rotation of the signal set symmetry angles. This can be achieved using a linear code, contrary to 2-D TCM where a nonlinear code is unavoidable.
- Shaping: increasing the signal dimensionality implies that larger shaping gain can be attained. Therefore, shaping techniques can be applied together with TCM technique to enhance to total coding gain.
- High-speed decoding: Multi-D TCM has a normally a high code rate, thus a larger number of bits are decoded at once [216].

The multi-D TCM is constructed similar to 2-D TCM. Set partitioning is applied on the multi-D signal set. Then, $\tilde{k}$ out of k information bits are encoded using a rate $\tilde{k}/(\tilde{k}+1)$ convolutional encoder. The output coded bits are used to select one of the $2^{\tilde{k}+1}$ signal subsets. The remaining information bits $k-\tilde{k}$ are used to choose one signal point from the selected subset to be transmitted. Afterward, the convolutional code is chosen, for a give number of states and a given code rate, in which the d_{free} is maximized and the $K_{d_{free}}$ is minimized.

The major part of designing a multi-D TCM scheme is the signal set partitioning, which cannot be realized by a simple plot as in the 2-D signal set case. Following Ungerboeck introduction of 2-D TCM [160], some groups have considered TCM with 4-D signal set [116, 124, 207] and with 8-D signal set [208]. However, they did not provide generic guidelines of how to design TCM schemes in the multi-D space. On the other hand, some systematic approaches for constructing multi-D TCM were proposed, which can be classified into three main categories:

1. Wei approach: L.-F. Wei [209] has proposed a geometrical method to construct a $2L$-D TCM based on a 2-D constituent rectangular constellation. The procedures of his approach are outlined as follows: in order to transmit $(L\eta+1)$ bits per $2L$-D symbol, a 2-D rectangular constellation Ω with $(2^{\eta}+2^{\eta}/L)$ signal points is chosen. Afterwards, Ω is partitioned to a desired number of sub-constellations. Following, the $2L$-D signal set is constructed by L-fold Cartesian product of Ω, and the mapping function between the $L\eta+1$ bits and the $2L$-D symbol is simplified and performed on the 2-D constellation. In addition, a shaping gain can also obtained using a shell mapping technique, the Ω is divided into two groups, inner group comprises 2^{η} signal points with the lowest energy and outer group comprises $2^{\eta}/L$ signal points with highest energy. Then, power saving is accomplished by eliminating those $2L$-D signal points with the highest energies. That is, the signal point's combinations from the outer group are excluded to minimize the signal power. Moreover, the proposed $2L$-D TCM scheme is rotationally invariant over all constellation symmetry. The Wei's approach of construction a TCM in the multi-D space was adopted by the telephone-line modem standard V.34 [210] and by digital subscriber line (DSL) modem [211].
2. Lattice approach: Calderbank and Sloane [115] have developed a method to construct multi-D TCM schemes using a lattice partition technique. As we have briefly discussed in Section 3.1, a lattice Λ can be partitioned into a sublattice Λ' and its cosets, denoted by Λ/Λ'. Accordingly, the signal constellation, which is assumed to be a finite subset of a lattice Λ, can be partitioned into subsets with increase minimum Euclidian distance. Then, the output of the convolutional code is used to select one subset (coset) from Λ/Λ' and the

remaining uncoded bits are used to select which one of signal points within the subset is to be transmitted. A list of various TCM codes based on this approach is presented in [115].

3. Multilevel coding (MLC) approach: It is based on the multilevel coding technique [212-214] and on the algebraic properties of the binary linear block codes. It was adopted for multi-D TCM design in [215, 216]. This approach will be discussed in details in the following section.

4.3 Multidimensional signal set partitioning

MLC is an effective technique to design a coded modulation system with an arbitrary large minimum distance in the Euclidean space. That can be achieved through combining multilevel binary codes with a judicious bits-to-symbol mapping [212]. It was suggested in [215, 216] that this technique together with algebraic properties of binary block codes can be fruitfully utilized to construct good multi-D TCM schemes. In the following, the main components for this approach are discussed. First, the partitioning of the linear block code into subcode and its cosets is described in Section 4.3.1. Then, the general structure of MLC technique is briefly outlined in Section 4.3.2. Finally, the multi-D signal set partitioning based on MLC is explained in Section 4.3.3.

4.3.1 Linear block code partitioning

Given a binary linear block code $C_0(n, k_0, d_0)$, with length n, dimension k_0 , minimum hamming distance d_0 and generator matrix G_0, we can take a subset of codewords from C_0 to form a linear subcode of C_0, denoted as $C_1(n, k_1, d_1)$ with $0 \leq k_1 < k_0$ and . The generator matrix $G_1$of C_1 can be simply obtained by selecting any set of k_1 rows from G_0. Now, let u be a binary n-tuples codeword in C_0 but not in C_1, then a modulo-2 sum of C_1 with u, denoted as $C_1 \oplus u$, generates a coset of C_1 in C_0. The codeword u is called a coset representative. Clearly, if $u \in C_1$, then $u \oplus C_1$ generates C_1 itself, due to the linear property of C_1.

Along the line with binary lattice partition, C_0 can be partition into $2^{k_0-k_1}$ disjoint cosets of C_1, denoted by C_0/C_1, such as the union of these cosets assembled into C_0. Then, if we arbitrarily pick one codeword from each of these distinct cosets, we have a set of coset representatives, referred to as $[C_0/C_1]$. The C_0 code can then be written as:

$$C_0 = \cup_{i=1}^{t}(u_i \oplus C_1) = [C_0/C_1] \oplus C_1 \tag{4-3}$$

where $t = 2^{k_0-k_1}$ is called the order of the partitioning. The set of coset representatives $[C_0/C_1]$, which comprises $2^{k_0-k_1}$ codewords, forms a linear code denoted by *coset code*. Furthermore, a linear subcode of C_1, denoted by $C_2(n, k_2, d_2)$ with $0 \leq k_2 < k_1$, can be formed. Then, the C_2 can be used to further partition each coset in $[C_0/C_1]$ into $2^{k_1-k_2}$ cosets of C_2. As a result, we obtain a partition chain $C_0/C_1/C_2$, which is made up of $2^{k_0-k_2}$ cosets of C_2 [217, 218]. Thus, Equation (4-3) can be updated to include C_1/C_2 partition as follows:

$$C_0 = [C_0/C_1] \oplus [C_1/C_2] \oplus C_2 \tag{4-4}$$

where $[C_1/C_2]$ represents the set of coset representatives for C_1/C_2 partition.

In general, let $C_0, C_1, C_2, \cdots C_m$ be a sequence of m linear codes such that each code is a subcode of the previous one, then a partition chain of C_0, denoted as $C_0/C_1/C_2 \cdots/C_m$, can be formed and C_0 can be expressed as:

$$C_0 = [C_0/C_1] \oplus [C_1/C_2] \oplus \cdots \oplus [C_{m-1}/C_m] \oplus C_m \tag{4-5}$$

Accordingly, every codeword in C_0 can be represented as a modulo-2 sum of the m coset representatives of the coset codes, i.e. $[C_0/C_1], [C_1/C_2] \cdots [C_{m-1}/C_m], C_m$. It follows that; each of the coset codes can be expressed as linear combinations of code generators, those generators are simply the coset representatives of the corresponding coset codes [121].

We may now illustrate the block code partitioning by an example, let $C_0(2,2,1)$ be a binary linear block consisting of four codewords, i.e. the codewords are the columns of $C_0 = \begin{bmatrix} 0 & 0 & 1 & 1 \\ 0 & 1 & 0 & 1 \end{bmatrix}$. The minimum hamming distance for C_0, which is the minimal number of positions in which any two codewords differ, is $d_0 = 1$. Following, $C_1(2,1,2)$ is a linear subcode of C_0 with two codewords, i.e. $C_1 = \begin{bmatrix} 0 & 1 \\ 0 & 1 \end{bmatrix}$. Thus, it has a minimum Hamming distance of $d_1 = 2$. C_1 induces a 2-way partition of C_0 into two cosets. The coset representative (or the generator) can be arbitrarily chosen to be $g_0 = [0\ 1]^T$, where $g_0 \in C_0$ but $g_0 \notin C_1$. Note that $[1\ 0]^T$ can also be chosen to perform the partitions and only the order of cosets will be different. Subsequently, the set of the coset representatives (or the coset code) $[C_0/C_1]$ can be found by binary linear combinations of g_0. That is, $[C_0/C_1]$ is composed of two codewords $[0\ 0]^T$ and $[1\ 1]^T$. From equation (4-3) we can readily see that C_0 can be represented as a union of $C_1 = C_1^0 = C_1 \oplus [0\ 0]^T$ and $C_1^1 = C_1 \oplus [0\ 1]^T$. The cosets of C_1 can be then expressed as [216]

$$C_1^{v_0} = C_1 \oplus v_0 g_0 \tag{4-6}$$

where $v_0 \in \{0,1\}$. Now, the last linear subcode in the partition chain is $C_2(2,0,\infty)$, which consists only of the all-zeros codeword $[0,0]^T$, thus the minimum hamming distance is $d_2 = \infty$. Each coset of C_1, one being C_1 itself and C_1^1, can be further partitioned into two cosets based on C_2. The generator g_1 should be chosen such as $g_1 \in C_1$ but $g_1 \notin C_2$, that leaves us with only one option $g_1 = [1\ 1]^T$. Accordingly, the cosets of C_2 can be written as:

$$C_2^{2v_1+v_0} = C_2 \oplus v_1 g_1 \oplus v_0 g_0 \tag{4-7}$$

Where v_0 and $v_1 \in \{0,1\}$. It can be seen that, for $v_0 = 0$, C_1 is partitioned into C_2 and C_2^2, and for $v_0 = 1$, C_1^1 is partitioned into C_2^1 and C_2^3 with $v_1 = 0$ and 1, respectively. It can be noted that, the union of the four cosets of C_2 form C_0, and that any codeword in C_0 can be written as a linear combination of the generators g_0 and g_1.

4.3.2 Multilevel coding

This section aims to introduce two important concepts. First, it will discuss how the multi-D signal set is constructed using MLC technique. Then, it will show how coding gain can be obtained based on MLC idea.

Given a 2-D signal set Ω with M points, each signal point $\boldsymbol{s} \in \Omega$ can be labelled with η-tuples binary vector, such as $\boldsymbol{s} = (s^{\eta-1}, \ldots, s^1, s^0)$ where $\eta = log_2 M$ denotes the spectral efficiency of Ω and $s^i \in \{0,1\}$ is the i-th coordinate of the binary label of the signal point $\boldsymbol{s}$. Equivalently, the signal point $\boldsymbol{s}$ can be represented as an integer number $\boldsymbol{s} \in \{0,1,\ldots,M-1\}$ given as $\boldsymbol{s} = \sum_{i=0}^{\eta-1} 2^i s^i$, where s^0 is in the least-significant-bit (LSB) level and $s^{\eta-1}$ is in the most-significant-bit (MSB) level. Following, a 2L-D signal constellation, denoted by $\mathcal{A}$, can be constructed by taking the L-fold

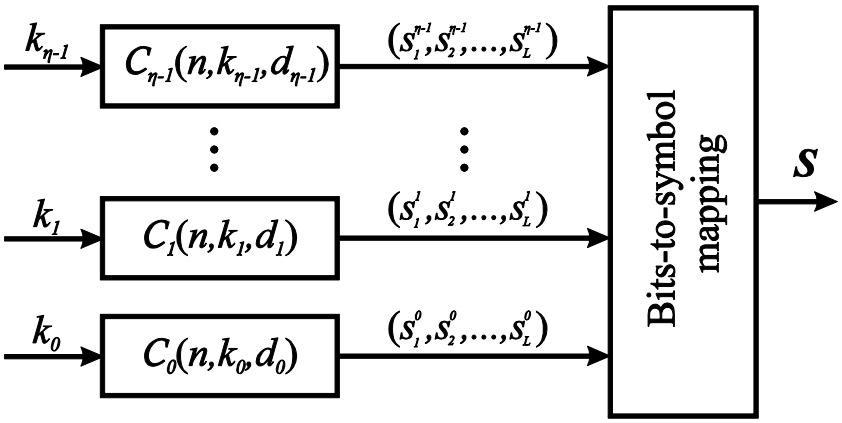

Fig. 4.5: Multilevel encoder consists of η-levels binary block codes

Cartesian product of the constituent 2-D signal set Ω, such that $\mathcal{A} = \Omega \times \Omega \times \cdots \times \Omega$ (L times) [200]. $\mathcal{A}$ comprises M^L $2L$-D signal points, that is, all possible combinations between L 2-D signal set Ω. Then, $\mathcal{A}$ can be expressed as:

$$\mathcal{A} = \begin{bmatrix} \boldsymbol{s_1} \\ \boldsymbol{s_2} \\ \vdots \\ \boldsymbol{s_L} \end{bmatrix} = \begin{bmatrix} s_1^{\eta-1} & \cdots & s_1^1 & s_1^0 \\ s_2^{\eta-1} & \cdots & s_2^1 & s_2^0 \\ \vdots & \cdots & \vdots & \vdots \\ s_L^{\eta-1} & \cdots & s_L^1 & s_L^0 \end{bmatrix} \tag{4-8}$$

where each row $\boldsymbol{s_j}, 1 \leq j \leq L$, represents the j-th 2-D signal point of the $2L$-D signal point and $(s_j^{\eta-1}, \ldots, s_j^1, s_j^0)$ is its binary labels, which are assigned according to a bits-to-symbol mapping function.

It was suggested in [212, 219] that multi-D signal constellation can be constructed using a multilevel coding technique, which involves combining a simple 1-D or 2-D signal constellation with binary block codes, the goal is to design a multi-D coded modulation with increased minimum distance compared with constituent signal constellation. Within this framework, $\mathcal{A}$ can be constructed using η-levels binary block codes as shown in Fig. 4.5. Each column of the matrix representation of $\mathcal{A}$ is corresponding to codewords from a binary block code $C_q(n, k_q, d_q), 0 \leq q \leq \eta - 1$. Hence, the first column from the left is generated by $C_{\eta-1}(n, k_{\eta-1}, d_{\eta-1})$ and the last column is generated by $C_0(n, k_0, d_0)$. Therefore, $\mathcal{A}$ can be represented as a η-tuples of binary block codes $\mathcal{A}(C_{\eta-1}, \ldots, C_1, C_0)$ [216]. Note that all of the constituent linear binary codes $C_q(n, k_q, d_q)$ have the same length $n = L$. The output η codewords are then interleaved and fed into a bit-to-symbol mapping function, where each η bits are used to label one signal point from the 2-D signal set according to a mapping function rule, that is, the bits $\boldsymbol{s_1} = (s_1^{\eta-1}, \ldots, s_1^1, s_1^0)$ specify the first 2-D symbol, $\boldsymbol{s_2} = (s_2^{\eta-1}, \ldots, s_2^1, s_2^0)$ specify the second 2-D symbol and $\boldsymbol{s_L} = (s_L^{\eta-1}, \ldots, s_L^1, s_L^0)$ specify the L-th 2-D symbol. The $2L$-D symbol $\boldsymbol{S}$ is then formed by these L 2-D symbols.

Assuming that all $2L$-D signal points $\boldsymbol{S} = [\boldsymbol{s_1}, \boldsymbol{s_2}, \ldots, \boldsymbol{s_L}]^T \in \mathcal{A}$ are equiprobable, then all of the η components codes are simply $(L, L, 1)$ binary block code and the minimum Euclidean distance of the $2L$-D signal set, is equal to the minimum Euclidean distance of constituent 2-D signal set Ω, no coding gain is attained though. However, similar to TCM scheme, a coding gain can be achieved

by introducing some constraints on the components 2-D symbols that are allowed to be transmitted, such that the distance between the transmitted 2L-D symbol sequences increased compared with the minimum distance between constituent 2-D signal points. To this end, mapping by signal set partitioning technique can by utilized together with binary block codes to achieve a coding gain.
The constituent 2-D signal set can be simply partitioned as described in [160, 204]. Following, the output of each constituent linear binary code is used to label one of the η partitioning levels. As example, for the 8-PSK partitioning case, presented in Section 4.1, three binary block codes, $C_0(n, k_0, d_0)$,$C_1(n, k_1, d_1)$ and $C_2(n, k_2, d_2)$, are needed to construct the MLC signal set. The 8-PSK signal set is divided into two QPSK signal sets at $p = 1$, which are then divided into four BPSK signal sets at $p = 2$. Finally, these BPSK signal sets are divided into eight subsetes, each contains a single point only. The codewords of C_0 with length n are used to choose a series of n QPSK signal sets. Then, the codewords of C_1 are used to select a series of n BPSK signal sets out of the chosen QPSK series. Finally, the codewords of C_2 determine the n signal points to be transmitted out of the selected BPSK series. The main designing parameter for MLC system is the minimum squared Euclidean distance between the multi-D signal points, denoted by Δ^2, which can be lower bounded as [219]:

$$\Delta^2 \geq \min\left(\delta_{\eta-1}^2\, d_{\eta-1}, \dots, \delta_1^2\, d_1, \delta_0^2\, d_0\right) \tag{4-9}$$

Where $d_0 \leq d_1 \leq \cdots \leq d_{\eta-1}$ are the minimum Hamming distances of the component binary codes $C_0,\ C_1, \dots,\ C_{\eta-1}$ and $\delta_0^2 \leq \delta_1^2 \leq \cdots \leq \delta_{\eta-1}^2$ are the minimum squared subset distances (MSSD) in the partition chain of the constituent 2-D signal set. As example, the minimum squared Euclidean distance for 8-PSK MLC system is $\Delta^2 \geq \min(4\, d_2, \dots, 2\, d_1, 0.586\, d_0)$. It can be noted that for a given dimension n, the minimum Hamming distance of the components binary codes should be maximized, as the result, the Δ^2 will be maximized. Note that, the MSSD for L= 1 is denoted by lower case delta δ^2 while the MSSD for L > 1, i.e. multi-D case, is denoted by upper case delta Δ^2 [216].

4.3.3 Multi-D signal set partitioning based on multilevel coding

The block codes partitioning technique, which was discussed in section 4.3.1, can be systematically employed to perform multi-D signal set partitioning [121, 216]. The multi-D signal set partitioning is best explained by an example. Consider a square 16QAM signal set to be used as a constituent 2-D signal set, denoted by Ω. For L= 2, the 4-D signal set $\mathcal{A}$ is constructed by 2-fold Cartesian product of Ω, i.e. $\mathcal{A} = \Omega \times \Omega$. It comprises $16^2 = 256$ points and can be represented as:

$$\mathcal{A} = \begin{bmatrix} \boldsymbol{s_1} \\ \boldsymbol{s_2} \end{bmatrix} = \begin{bmatrix} s_1^3 & s_1^2 & s_1^1 & s_1^0 \\ s_2^3 & s_2^2 & s_2^1 & s_2^0 \end{bmatrix} \tag{4-10}$$

Each signal point $\boldsymbol{S} = [\boldsymbol{s_1}, \boldsymbol{s_2}]^T \in \mathcal{A}$ consists of two 2-D signal points, $\boldsymbol{s_1}$ and $\boldsymbol{s_2} \in \Omega$. Four bits are needed to label signal points in the 2-D signal set, thus eight bits are required to label all 256 signal points in the 4-D signal set. As discussed in previous section, the 4-D signal set $\mathcal{A}$ can be generated by 4-levels linear binary code $C_0(2,2,1)$, such that each of the four columns of Equation (4-10) corresponds to a codeword from C_0. Therefore, the 4-D signal, which includes all of 256 4-D signal points, is denoted as $\mathcal{A}_p = \mathcal{A}_0 = \mathcal{A}(C_0, C_0, C_0, C_0)$, where the superscript p refers to the current partition level. Here $p = 0$ since no partition was yet applied.

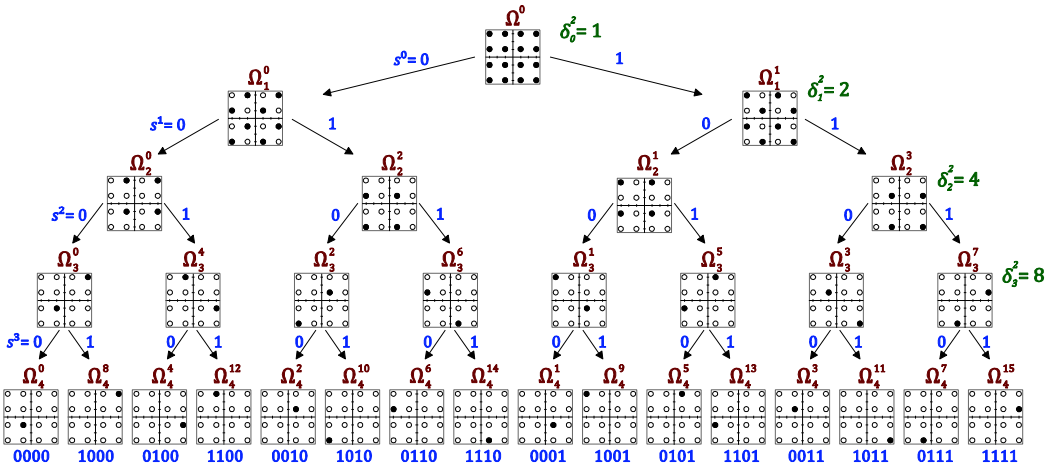

Fig. 4.6: Partitioning of 16QAM signal set

Before describing the partitioning process of the 4-D signal set, we should first present the partitioning of the constituent 2-D 16-QAM signal set. Fig. 4.6 show the four levels partitioning of the 16QAM signal set. The signal set at $p = 0$, denoted as $\Omega = \Omega_0$, consists of 16 signal points and has a minimum Euclidian distance $\delta_0^2 = 1$, assuming average signal energy $E_s = 5$. At $p = 1$, Ω_0 can be partitioned into subset $\Omega_1 = \Omega_1^0$ and its coset Ω_1^1, where the subscript denotes the current partition level and the superscript denotes the subset index. Each subset has 8 signal points and MSSD $\delta_1^2 = 2\delta_0^2$. Following, each of the two cosets is further partitioned into two cosets, each has 4 signal points and $\delta_2^2 = 4\delta_0^2$. The partitioning continues in the similar way for $p = 3$, where each subset has two signal points and $\delta_3^2 = 8\delta_0^2$. Finally, at $p = 4$, only one signal point is left in each subset and thus $\delta_4^2 = \infty$. As it can be seen in Fig. 4.6, the superscript indices of these cosets represent the signal number $\boldsymbol{s} = \sum_{i=0}^{3} 2^i s^i$ with $\boldsymbol{s} \in \{0,1, \dots, 15\}$.

After introducing the partitioning of the constituent 2-D signal set, we can proceed to the 4-D signal set partitioning. The partitioning of the 4-D signal set into 4-D subsetes and their cosets can be explained with the assistance of the block code partitioning technique. That is, through the partitioning of the multilevel code $\mathcal{A}_0$ into multilevel subcodes and their cosets.

At $p = 0$, $\mathcal{A}_0$ contains 256 signal points and the minimum squared Euclidian distance between these signal points is $\Delta_0^2 = \delta_0^2 = 1$. Next, at partitioning level $p = 1$, the subcode $C_1 \subset C_0$ can be used to partition one of the 4-level codes of $\mathcal{A}_0$. The target is to find the partitioning which maximizes the MSSD Δ_1^2. So let us assume first that the code C_0 corresponding to the level 0 is the one to be partitioned, such that C_0 is partitioned into a subcode C_1^0 and its coset C_1^1. Accordingly, $\mathcal{A}_0$ is partitioned into two cosets, $\mathcal{A}_1^0$ and $\mathcal{A}_1^1$. Since C_1^0 contains only two codewords, the all-zeros and the all-ones codewords, then the LSBs $[s_1^0, s_2^0]^T$ of the signal points in the subset $\mathcal{A}_1^0 = \mathcal{A}(C_0, C_0, C_0, C_1)$ can be either zeros or ones. Similarly, C_1^1 comprises two codewords, $[0,1]^T$ and $[1,0]^T$, thus LSBs of the signal points in the coset $\mathcal{A}_1^1$ should not be equal, i.e. either $[0,1]^T$ or $[1,0]^T$. Accordingly, each of two cosets contains 128 4-D signal points and can be constructed based on the 2-D cosets as follows $\mathcal{A}_1^0 = \{\Omega_1^0 \times \Omega_1^0 \cup \Omega_1^1 \times \Omega_1^1\}$ and $\mathcal{A}_1^1 = \{\Omega_1^0 \times \Omega_1^1 \cup \Omega_1^1 \times \Omega_1^0\}$. Thus, it can be readily seen that the MSSD for this partitioning is equal to $\Delta_1^2 = 2$. In more general way, the lower bound for the MSSD can be found using Equation (4-9) as follows:

$$\Delta_1^2 \geq \min(\delta_3^2 d_0, \delta_2^2 d_0, \delta_1^2 d_0, \delta_0^2 d_1) = \min(8d_0, 4d_0, 2d_0, 1d_1) = 2 \tag{4-11}$$

For $d_0 = 1$ and $d_1 = 2$, the bound is fulfilled with equality. Let us now consider the case where the code C_0 which is chosen to be partitioned is other than the one at level 0. Then, it can be found from Equation (4-11) that these partitioning is useless since the MSSD is equal to $\Delta_1^2 = \Delta_0^2 = 1$. Therefore, the code which should be partitioned at $p = 1$ in order to maximize the MSSD is the one corresponding to the level 0.

Similar to the coset codes, the two cosets, $\mathcal{A}_1^0$ and $\mathcal{A}_1^1$, at the partitioning level $p = 1$ can be expressed as:

$$\mathcal{A}_1^{v_0} = \mathcal{A}_1^{v_0} \oplus v_0 \mathcal{G}_0 \tag{4-12}$$

where $v_0 \in \{0,1\}$ and $\mathcal{G}_0$ is the coset generator, which is a multilevel codeword such that $\mathcal{G}_0 \in \mathcal{A}_0$ but $\mathcal{G}_0 \notin \mathcal{A}_1^0$. As discussed in Section 4.3.1, $g_0 = [0\ 1]^T$ can be used as a coset generator for C_1^0, in the similar way, it can be inserted at level 0 of the coset generator $\mathcal{G}_0$. Since codes at level 1, level 2 and level 3 are not yet partitioned, and then all-zero vectors are inserted at these levels of the $\mathcal{G}_0$. Therefore, $\mathcal{G}_0$ can be written as:

$$\mathcal{G}_0 = \begin{bmatrix} 0 & 0 & 0 & 0 \\ 0 & 0 & 0 & 1 \end{bmatrix} \tag{4-13}$$

The $\mathcal{G}_0$ in Equation (4-13) is given in the binary form; a different way to represent $\mathcal{G}_0$ is to give it in integer form, i.e. $\mathcal{G}_0 = [0\ 1]^T$. In this case, the modulo-2 sum in Equation (4-12) should be replaced by modulo-M sum, then for the 16QAM signal, it is substituted by modulo-16 sum and the two cosets are formed as:

$$\mathcal{A}_1^{v_0} = \mathcal{A}_1^{v_0} + v_0 \begin{bmatrix} 0 \\ 1 \end{bmatrix} (mod\ 16) \tag{4-14}$$

It should be noted that, using either (4-12) or (4-14), brings the needed partition and the resulting cosets will contain the same signal points. However, the order of these signal points will be different depending whether modulo-2 or modulo-16 sum was used [216].

We proceeds in the partitioning tree, at $p = 2$, each of the two cosets from the the previous partitioning level is further partitioned into two cosets. Therefore, four cosets are obtained, that is, the subset $\mathcal{A}_2^0$ and its cosets $\mathcal{A}_2^1$, $\mathcal{A}_2^2$ and $\mathcal{A}_2^3$, each comprises 64 signal points. The partition should be realized in such way that the MSSD Δ_2^2 is as big as possible. In this case, there are two choices to form the subset $\mathcal{A}_2^0$ from the subset $\mathcal{A}_1^0 = \mathcal{A}(C_0, C_0, C_0, C_1)$. The first option is to substitute the C_0 code at level 1 by a subcode C_1 and the second option is to substitute the subcode C_1 at level 0 by a subcode C_2. In both cases the number of signal points within the subset $\mathcal{A}_2^0$ will be half compared with $\mathcal{A}_1^0$ and thus a valid partition is obtained. For the MSSD calculation, let us first consider the first option $\mathcal{A}_2^0 = \mathcal{A}(C_0, C_0, C_1, C_1)$, then the MSSD Δ_2^2 can be calculated as $\Delta_2^2 = \min(8d_0, 4d_0, 2d_1, 1d_1)$ with $d_0 = 1$ and $d_1 = 2$ then $\Delta_2^2 = 2$. For the second option $\mathcal{A}_2^0 = \mathcal{A}(C_0, C_0, C_0, C_2)$, then $\Delta_2^2 = \min(8d_0, 4d_0, 2d_0, 1d_2)$ with $d_0 = 1$ and $d_2 = \infty$ then Δ_2^2 is also equal to 2. Therefore, either of the two options can be used at $p = 2$, the only difference is that the subset resulting from first option is constructed as $\mathcal{A}_2^0 = \{\Omega_2^0 \times \Omega_2^0 \cup \Omega_2^1 \times \Omega_2^1 \cup \Omega_2^2 \times \Omega_2^2 \cup \Omega_2^3 \times \Omega_2^3\}$ it can be noted that it is formed using subsets from the second level of partitioning of the constituent 16QAM signal set presented in Fig. 4.6, while for the second option the subset $\mathcal{A}_2^0 =$

Table 4-1: The signal set partitioning for 4-D 16QAM

Partition level p	Subset $\mathcal{A}_p$	MSSD Δ_p^2	Coset generator $\mathcal{G}_p$
0	$\mathcal{A}(C_0, C_0, C_0, C_0)$	$\min(8,4,2,1) = 1$	$[0\ 1]^T$
1	$\mathcal{A}(C_0, C_0, C_0, C_1)$	$\min(8,4,2,2) = 2$	$[1\ 1]^T$
2	$\mathcal{A}(C_0, C_0, C_0, C_2)$	$\min(8,4,2,\infty) = 2$	$[0\ 2]^T$
3	$\mathcal{A}(C_0, C_0, C_1, C_2)$	$\min(8,4,4,\infty) = 4$	$[0\ 4]^T$
4	$\mathcal{A}(C_0, C_0, C_2, C_2)$	$\min(8,4,\infty,\infty) = 4$	$[2\ 2]^T$
5	$\mathcal{A}(C_0, C_1, C_2, C_2)$	$\min(8,8,\infty,\infty) = 8$	$[4\ 4]^T$
6	$\mathcal{A}(C_0, C_2, C_2, C_2)$	$\min(8,\infty,\infty,\infty) = 8$	$[0\ 8]^T$
7	$\mathcal{A}(C_1, C_2, C_2, C_2)$	$\min(16,\infty,\infty,\infty) = 16$	$[8\ 8]^T$
8	$\mathcal{A}(C_2, C_2, C_2, C_2)$	$\min(\infty,\infty,\infty,\infty) = \infty$	

$\{\Omega_1^0 \times \Omega_1^0\}$ is formed using subsets from the first level of partitioning, in the following the second option will be adopted. Then, the coset generator $\mathcal{G}_1$ can be formed by inserting the generator $g_1 = [1\ 1]^T$ at the level 0, as following:

$$\mathcal{G}_1 = \begin{bmatrix} 0 & 0 & 0 & 1 \\ 0 & 0 & 0 & 1 \end{bmatrix} \tag{4-15}$$

equivalently, it can be written in integer form as $\mathcal{G}_1 = [1\ 1]^T$. The four cosets at $p = 2$ can be obtained as following

$$\mathcal{A}_2^{2v_1+v_0} = \mathcal{A}_2^{2v_1+v_0} + v_1 \begin{bmatrix} 1 \\ 1 \end{bmatrix} + v_0 \begin{bmatrix} 0 \\ 1 \end{bmatrix} \ (mod\ 16) \tag{4-16}$$

Afterwards, the partitioning continues in the same manner for the remaining partitioning levels until the last partitioning level, in this case $p = 8$, is reached, where the target at each level is to maximize the MSSD. Table 4-1 summarizes the signal set partitioning for 4-D 16QAM using the subcodes technique
[220]. It can be noted from Table 4-1 that, $\Delta_1^2 = \Delta_2^2$, $\Delta_3^2 = \Delta_4^2$ and $\Delta_5^2 = \Delta_6^2$. Nevertheless, the average number of nearest neighbors K_p at the partition level $p = 2, 4$ and 6 is less than the K_{p-1} at the partition level $p = 1, 3$ and 5 , respectively. As example, the average number of nearest neighbors at $p = 1$ is $K_1 = 13.5$ however this number is reduced to $K_2 = 4.5$ at $p = 2$.
From the coset generators presented in Table 4-1, we can express mapping for the 4-D 16QAM signal set as following:

$$\boldsymbol{S^v} = \begin{bmatrix} \boldsymbol{s_1} \\ \boldsymbol{s_2} \end{bmatrix} = v_7 \begin{bmatrix} 8 \\ 8 \end{bmatrix} + v_6 \begin{bmatrix} 0 \\ 8 \end{bmatrix} + v_5 \begin{bmatrix} 4 \\ 4 \end{bmatrix} + v_4 \begin{bmatrix} 2 \\ 2 \end{bmatrix} + v_3 \begin{bmatrix} 0 \\ 4 \end{bmatrix} + v_2 \begin{bmatrix} 0 \\ 2 \end{bmatrix} + v_1 \begin{bmatrix} 1 \\ 1 \end{bmatrix} + v_0 \begin{bmatrix} 0 \\ 1 \end{bmatrix} \ (mod\ 16) \tag{4-17}$$

Equation (4-17) is used in the signal set mapper to map the encoded bits v_i where $0 \leq i \leq 7$ into 4-D signal points $\boldsymbol{S^v} = [\boldsymbol{s_1}, \boldsymbol{s_2}]^T$ where $\boldsymbol{v} = \sum_{i=0}^{7} 2^i v_i$ is the equivalent decimal representation of the encoded bits v_i, i.e. the signal number.
In general, the mapping rule using coset generators technique can be expressed as:

$$\boldsymbol{S^v} = \begin{bmatrix} \boldsymbol{s_1} \\ \vdots \\ \boldsymbol{s_L} \end{bmatrix} = \sum_{i=0}^{\eta L-1} \mathcal{G}_i \, v_i \; (mod\ 2^{\eta}) \tag{4-18}$$

The coset generators for 4-D ($L = 2$) and higher dimensional ($L > 2$) signal sets are tabulated for *M*PSK signals in [216] and *M*QAM signals in [220].

4.4 The Encoder System for Multidimensional TCM

As previously stated, the encoder system for multi-D ($2L$-D) TCM is similar to the one for 2-D TCM. That is, $k = \eta L - 1$ information bits are fed into the encoder, from which, $\tilde{k}$ bits are encoded by a rate $\tilde{k}/(\tilde{k}+1)$ convolutional encoder and the remaining $k - \tilde{k}$ are left uncoded. The output $(k+1)$ bits, denoted by w_i with $0 \leq i \leq k$, are input to $2L$-D signal set mapper, which performs the set partitioning based on the multilevel coding technique described in Section 4.3.3.

The spectral efficiency for such $2L$-D TCM scheme, defined as the number of information bits transmitted per 2-D signal period τ, is equal to $SE = k/L$ where the unit is (bits/symbol). An interesting feature of mapping technique using coset generators is the possibility to attain different *SEs* with the same encoder structure. That can be realized by setting the ξ least significant bits in the coset generator equation to zero [216]. Therefore, for $\xi = 0$, the $2L$-D signal mapper selects a signal point in $\mathcal{A}$, where $\mathcal{A}$ is $2L$-D signal set at the partition level $p = 0$. While for $\xi > 0$, it select a signal point that belongs to a subset of $\mathcal{A}$ but not to its cosets at $p = \xi$. Note that since the MSSD for the subset of $\mathcal{A}$ is larger than the MSSD of $\mathcal{A}$, then, better perfomace is obtained for $\xi > 0$ and the resulting spectral efficiency is reduced $SE = (k - \xi)/L$ (bits/symbol).

As an example, if we set the bit v_0 to zero in the Equation (4-17), then the subset $\mathcal{A}_1^0 = \mathcal{A}(C_0, C_0, C_0, C_1)$ will be always selected, this subset is then considered as base signal set at $p = 0$ and the $2L$-D signal set mapper will map the input $(k-1)$ to a point $\boldsymbol{S^v} \in \mathcal{A}_1^0$ according to the following coset generators:

$$\begin{aligned} \boldsymbol{S^v} = \begin{bmatrix} \boldsymbol{s_1} \\ \boldsymbol{s_2} \end{bmatrix} = v_6 \begin{bmatrix} 8 \\ 8 \end{bmatrix} + v_5 \begin{bmatrix} 0 \\ 8 \end{bmatrix} + v_4 \begin{bmatrix} 4 \\ 4 \end{bmatrix} + \; v_3 \begin{bmatrix} 2 \\ 2 \end{bmatrix} + \\ v_2 \begin{bmatrix} 0 \\ 4 \end{bmatrix} + v_1 \begin{bmatrix} 0 \\ 2 \end{bmatrix} + v_0 \begin{bmatrix} 1 \\ 1 \end{bmatrix} \; (mod\ 16) \end{aligned} \tag{4-19}$$

The SE is reduced from 3.5 bits/symbol for $\xi = 0$ to 3.0 bits/symbol for $\xi = 1$, but the MSSDs of the base signal set is doubled.

4.5 Rotationally Invariant Multidimensional TCM

A very attractive feature of the TCM schemes is the possibility to design a coded modulation system which is invariant to various phase rotations. To illustrate this point, we consider the 4-D 16QAM TCM case.

Fig. 4.7 (a) and (b) shows the labelling of the 2-D 16QAM signal set Ω obtained in Section 4.3.3 given in binary and integer form, respectively. Note that Ω can be seen as a union of four subsets α_i, where i is the index of the subset with $0 \leq i \leq 3$. Each of these subsets consists of four signal points. The different subsets are marked with different colors. Let the two LSBs of the binary labels indicate the subset index, then the first subset is α_0 (blue points). Following, a 90° phase rotation of α_0 generate the next subset α_1 (green points). It can be noted that the two MSBs are not affected by this rotation and they stay unchanged, while the two LSBs are affected. The same applies when

rotating $\alpha_1$by 90°, the α_2 (orange points) is obtained. Finally, the α_3 (red points) is obtained by rotating $\alpha_2$by 90°. Note that the two MSBs of the signal points within each subset are altered in the same way as the naturally mapped QPSK. Therefore, the mapping rule presented in Fig. 4.7 is called natural mapping [220].

As discussed before, the 2-D 16QAM signal set Ω is used as constituent component to form the 4-D 16QAM signal set $\mathcal{A}$. The bits-to-symbol mapping function is performed according to the coset generators method defined in (4-17). Now, to investigate the effect of 90°phase rotation on the 4-D signal points, let us consider the following example.

Let $\boldsymbol{v} = [0,0,1,1,1,0,1,1]$ be the input bits to the 4-D signal set mapper. According to (4-17), these bits will be mapped into the 4-D symbol $\boldsymbol{S^v} = [7,12]^T$. Now, if we induce a 90° phase rotation in anticlockwise direction, then the rotated 4-D symbol will be $[4,13]^T$. By substituting these numbers into the left side of (4-17), it can be easily found that the rotated 4-D symbol will be demapped into $\tilde{\boldsymbol{v}} = [0,1,1,0,0,0,0,1]$. Hence, four bits are affected by this 90° phase rotation, namely, the 2nd, 4th, 5th and 7th bits, where the order is assumed such that the LSB is the 1st bit.

It was suggested in [220] that it is possible to reduce the number of bits which are affected by the 90° phase rotation for multi-D *M*QAM signals. This can be achieved by modifying the equation of signal set mapper given in (4-18). Accordingly, instead of using only modulo-2^η arithmetic, it was suggested to use a combination of modulo-4 and modulo-2 arithmetic. In such a way, only two bits are affected by the 90° phase rotation. For the 4-D 16QAM case, the mapping function can be expressed as [220]:

$$\begin{aligned}\boldsymbol{S^v} = \begin{bmatrix}\boldsymbol{s_1}\\ \boldsymbol{s_2}\end{bmatrix} = \left[(2v_4 + v_1)\begin{bmatrix}1\\1\end{bmatrix} + (2v_2 + v_0)\begin{bmatrix}0\\1\end{bmatrix}(mod\ 4)\right] \\ + 4\left[v_5\begin{bmatrix}1\\1\end{bmatrix} \oplus v_3\begin{bmatrix}0\\1\end{bmatrix}\right] + 8\left[v_7\begin{bmatrix}1\\1\end{bmatrix} \oplus v_6\begin{bmatrix}0\\1\end{bmatrix}\right]\end{aligned} \tag{4-20}$$

It should be emphasized that by employing the equation (4-20) in the signal set mapper, we can still acquire the same subsets as if we employed equation (4-17), however, the order of signal points within the subsets will be different.

Let us now check the effect of the 90° phase rotation on the 4-D symbols which are mapped according to the new rule. If we plug in the aforementioned input bits $\boldsymbol{v}$ to the equation (4-20), then the resultant 4-D symbol is $\boldsymbol{S^v} = [7,0]^T$. The 90° phase rotation will turn it into $[4,1]^T$. The rotated version of the 4-D symbol will be demapped into $\tilde{\boldsymbol{v}} = [0,0,1,0,1,0,0,1]$ according to

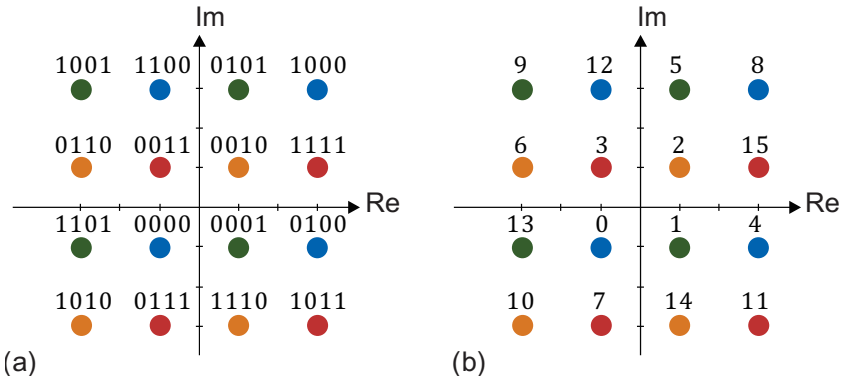

Fig. 4.7: (a) the binary labelling of the 2-D 16QAM signal set (b) the corresponding labelling given in integer form

(4-20). Subsequently, only two bits are affected by the rotation, namely, 2nd and 5th bits. Therefore, these two bits must be differentially encoded/decoded to insure that all bits are correctly recovered (in the absence of noise) after integer number of 90° phase rotation.

To construct a TCM system which is rotationally invariant, a mandatory condition is that the convolutional encoder produces a valid code sequence from the rotated version of the input code sequence. In other words, if the input bits sequence to the convolutional encoder is replaced by the rotated bits sequence, then the parity check equation of the encoder should be still satisfied. This condition can be met with a linear code in the multi-D signal set [221], while a nonlinear code is required for the 2-D case [222].

4.6 Turbo-TCM

In order to go beyond the capacity limits of TCM, a turbo code principle [223] with TCM as constituent codes has been proposed, referred to as TTCM [224]. By applying iterative decoding techniques, TTCM achieves a performance just 1 dB away of the Shannon limit for BER in the range between 10^{-4} to 10^{-5} [224]. Subsequently, an outer HD-FEC code can then further reduce the BER to a desired level for optical communication transmission system, i.e. BER< 10^{-12}. The principle of the operation for the encoder and decoder for TTCM will be discussed in the following subsections

4.6.1 Encoder system

The TTCM encoder structure is shown in Fig. 4.8. A block of $l \cdot k$ information bits is fed to the encoder to generate a multi-D symbol sequence of length l. For each multi-D symbol, only $\tilde{k}$ out of k bits are encoded, while the remaining $k - \tilde{k}$ bits are left uncoded. The systematic bits $\boldsymbol{c}^t = [b_1^t, b_2^t, \dots, b_{\tilde{k}}^t]$, with $t \in \{1,2, \dots, l\}$, are encoded by a rate $R = \tilde{k}/(\tilde{k}+1)$ systematic feedback convolutional encoder. In parallel, the systematic bits $\boldsymbol{c}^t$ are fed to an interleaver of length l. The interleaver maps each group of bits $\boldsymbol{c}^t$ with an odd (even) t index to a different odd (even) t index. The interleaved bits are then encoded by the same convolutional encoder, followed by a de-interleaver, which reverses the permutation introduced by the interleaver. Since the encoder is systematic, the output of the upper convolutional encoder and the output of the de-interleaver are different only in the parity bits, while the remaining bits are identical. A selector is then used to alternatively switch between the parity bits from the upper and lower encoder. Such that the bits $\boldsymbol{v}^t$, where t is odd (even) indices are provided by the upper (lower) encoder. The resulting bits

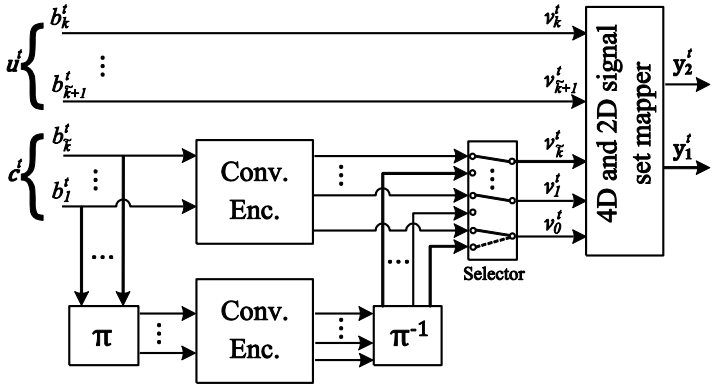

Fig. 4.8: Block diagram of the TTCM Encoder system. © IEEE 2016 [87].

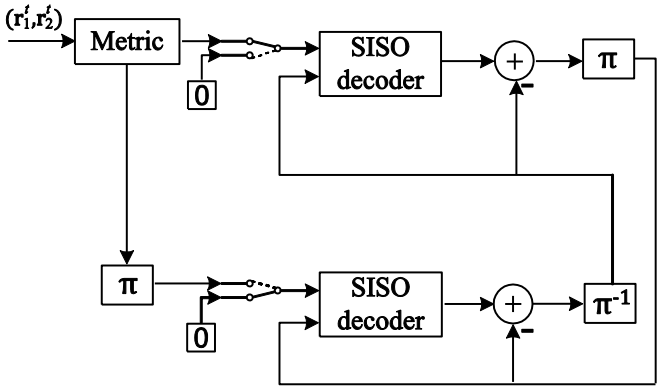

Fig. 4.9: (a) Block diagram of the TTCM Decoder system. © IEEE 2016 [87].

$\boldsymbol{v}^t = [v_0^t, v_1^t, \ldots, v_k^t]$ are then mapped to a multi-D symbol using the MLC technique described in the Section 4.3.3.

4.6.2 Decoder system

The TTCM decoder is shown in Fig. 4.9. It is based on the iterative decoding technique. The decoder iteration comprises two stages. Each stage employs a soft-input soft-output (SISO) decoder. The SISO decoder receives two inputs, (1) the soft metric corresponding to the received symbols and (2) a-priori information produced by the other decoder. At the beginning, multi-D symbol log-likelihood ratios (LLRs) are calculated and provided as a soft metric to the decoder. For the first decoding stage, the soft metrics corresponding to the odd multi-D symbols (t is odd) are fed to the upper SISO decoder, whereas the soft metrics with even indices are (t is even) set to zero (punctured). For the SISO decoder, symbol-by-symbol maximum a posteriori (MAP) decoding was employed [225]. The algorithm calculates the a-posteriori information of the input bits. Subsequently, the input a-priori information received from the other decoder is subtracted from the SISO decoder's output. The resulting information forms the a-priori information, which will be fed to the next decoding stage. For the second decoding stage, the soft metric of the even multi-D symbols together with the a-priori information produced by the first decoding stage is interleaved and fed to the lower SISO decoder. At the output of this decoder, the a-priori information is calculated as in the first decoding stage before being de-interleaved and forwarded to the upper SISO decoder. By now one decoder iteration is finished. The iteration process is repeated until a prescribed maximum number of iterations is reached. Finally, the a- posteriori information at the output of the lower SISO decoder is de-interleaved and sent to a hard-decision unit, resulting in an estimation of the transmitted systematic information bits. The uncoded bits are then estimated by considering the parallel transitions of the most likely states on the trellis [224].
The computation of the MAP decoding algorithm can be performed in the logarithmic domain, so called log-MAP algorithm. As a rule of thumb, log-MAP algorithm is three times more complex than the Viterbi algorithm [200, p. 570]. Since the algorithm is executed two times per turbo iteration. Then, the TTCM decoder is generally assumed to have a higher complexity compared with TCM decoder by a factor of (6×number of iterations) [226, p.411-414].

4.7 Author contribution related to this chapter

In this chapter, the aim was to analyze different designing approaches for multi-D TCM and to choose the one which is best suited for optical communication systems. I have implemented all the

necessary functions to operate and evaluate the multi-D TCM based on MLC approach. In addition, I have implemented all the needed functions to examine the TTCM approach with multi-D signal set. The experimental results for 4-D TCM/TTCM will be presented in Chapter 5.

CHAPTER 5

System Experiments

This chapter presents two experimental investigations of the topics discussed in previous chapters. The first experiment introduces an evaluation of a 4-D 128-SP-QAM modulation format, which was discussed in chapter 3, in a Nyquist-wavelength division multiplexing (NWDM) system. The performance of this 4-D format is investigated in presence of two SD-FEC codes, namely, the TPC and the LDPC code.

The second experiment demonstrates a realization of flexible optical transceivers based on 4-D TCM and TTCM, which was described in chapter 4. In addition, the performance of 4-D TCM and TTCM concatenated with low-complexity HD-FEC is compared with the standard PDM-*M*QAM formats combined with SD-FEC code.

5.1 Transmission performance of 4-D 128-SP-QAM with SD-FEC

It should be first mentioned that the discussion and the materials presented in this section are based on the Author's publication [174].

Moving beyond 100 Gb/s throughput per wavelength channel in fiber optical communication systems requires using a powerful SD-FEC code. The two main SD-FEC codes suitable for optical communication are the TPC and LDPC code. In addition, advanced optical modulation formats play an important role in designing a flexible, robust and spectrally efficient optical transmission system. Along with standard PDM-*M*QAM formats, 4-D modulation formats provide a means to tune system parameters such as spectral efficiency, bit rate and reach [32]. In particular, 4-D *M*-SP-QAM, where *M* is the size of the signal alphabet, are produced by applying Ungerboeck's set-partitioning scheme to their PDM-*M*QAM counterparts. As it was discussed in section 3.4.3, each partitioning will lead to a larger minimum Euclidean distance between constellation points and thus better power efficiency at the expense of 1 bit/s/Hz reduction of the SE. This permits to adjust the system parameters with minor hardware changes. For instance, 128-SP-QAM is generated by applying a single set-partitioning to PDM-16QAM in four dimensions. It encodes 7 bits per symbol and provides an asymptotic power efficiency gain of 1.55 dB compared to PDM-16QAM [169].

It has been shown that 128-SP-QAM is a promising candidate to smoothen the transition between PDM-16QAM and PDM-QPSK modulation formats in bit rate variable transponders. Its performance has been investigated in uncoded simulations [168] and experiments [169, 170]. However, the aforementioned publications only consider uncoded transmission. In [164] the performance of *M*-SP-QAM formats was compared with PDM-*M*QAM by numerical simulations for different constellation size *M* in the presence of SD-FEC based on an LDPC code. It was shown that the larger SD-FEC overhead employed for the 128-SP-QAM format enables a sensitivity improvement of 0.8 dB at BER= 2×10^{-3} compared with 64-SP-QAM and PDM-8QAM at the same bit rate.

In this work, we experimentally evaluate the performance of 128-SP-QAM signals at a symbol rate of 28 GBd in a Nyquist WDM system with two FEC codes, a TPC and the LDPC code, which was considered in [164]. It is observed that the TPC offers a faster convergence of the decoder towards

the error-free state compared with the LDPC code. However, application of the LDPC code enables better performance after decoder convergence.

5.1.1 Experimental setup and DSP

The experimental setup is shown in Fig. 5.1. Three Nyquist WDM super-channels are generated, each formed by multiplexing five wavelengths channels. Fifteen external cavity lasers (ECL) with <100 kHz linewidth and spaced 35 GHz apart are separated into even and odd channel groups. The two groups are then modulated independently by integrated dual-polarization (DP) I/Q modulators which are driven by 4-channel DAC operating at a sample rate of 56 GS/s and 8 bit resolution. The modulated optical signals are then amplified using EDFAs before being power equalized and fed into the fiber loop. The optical spectrum of the 128-SP-QAM signal at the input of the fiber loop is shown in Fig. 5.1(a).

The loop consists of three 80 km standard single mode fiber (SSMF) spans, a loop-synchronous polarization scrambler to avoid unrealistic accumulation of polarization impairments, a programmable gain equalizer filter to flatten the loop gain over the considered frequency band and EDFAs.

At the receiver, the channel under test at 193.4 THz is selected by an optical band-pass filter and detected by a polarization-diversity coherent receiver. The LO laser is an ECL with <100 kHz linewidth. The signals are then digitized using ADC operating at a sample rate of 50 GS/s. DSP is performed offline on a computer.

For the transmitter side DSP, random information bit sequences are encoded either by TPC or LDPC prior to bit to symbol mapping. Afterwards, header sequences required for the data-aided DSP at the receiver are periodically inserted into the payload signal leading to 2.7% overhead. After header insertion, a root raised cosine pulse-shaping filter with a roll-off factor of 0.1 is applied. Finally, digital pre-distortion is carried out to compensate for the linear and nonlinear transfer characteristics of DAC, driver amplifiers and DP I/Q modulator.

At the receiver side DSP, the signal is first resampled to 2 samples per symbol. Subsequently, compensation for quadrature imbalance of the optical frontend is carried out. The accumulated CD is then estimated and compensated for by a frequency domain equalizer. Next, the signal is sent

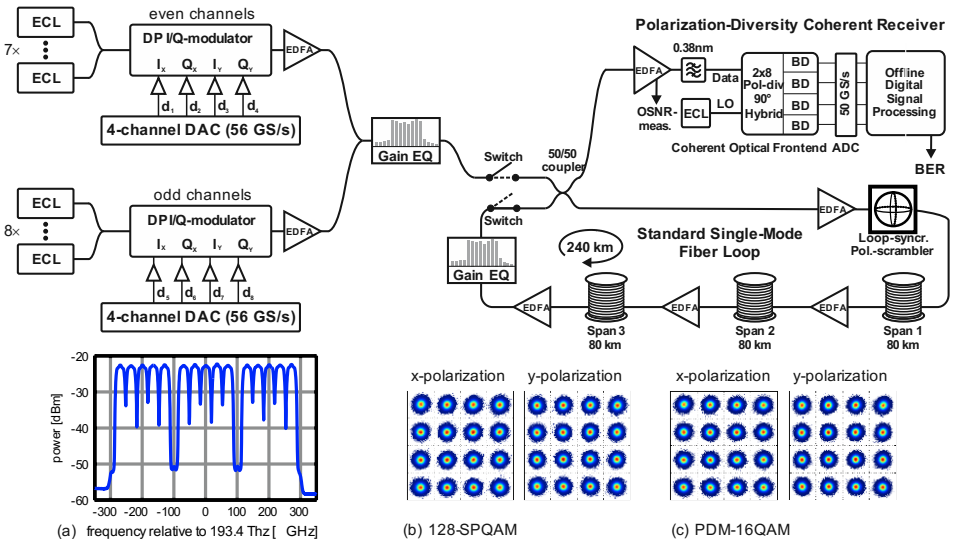

Fig. 5.1: Experimental setup. (a) Optical spectrum at the input of the fiber loop. (b), (c) Back-to-back recovered constellations of the channel under test at 193.4 THz at maximum OSNR (~31 dB). © IEEE 2015 [174].

into a data-aided single-carrier frequency domain equalizer (DA-SC-FDE) [75], which performs carrier frequency recovery, polarization demultiplexing and equalization. Subsequently, carrier phase recovery is carried out based on the blind phase search algorithm including pilot-aided phase unwrapping for cycle slip mitigation [85]. Constellation diagrams of the recovered 128-SP-QAM and PDM-16QAM signals after DSP are shown for maximum OSNR in Fig. 5.1 (b) and (c), respectively.

5.1.2 The FEC schemes

Two FEC codes were considered for the 128-SP-QAM format, a TPC and an LDPC code. The TPC is constructed by two BCH codes, BCH(256,239,6) × BCH(128,113,6). It has a code rate R= 0.8242 with 21.3% overhead and a minimum Hamming distance d = 36. The second considered option is the LDPC code which was evaluated for 128-SP-QAM in numerical simulations [164]. It is based on FEC encoding/decoding defined by the Digital Video Broadcasting over Satellite (DVB-S2) standard [227]. The code consists of a concatenation of a BCH (54000, 53840) code and an LDPC (64800, 54000) code, which results in a code rate R = 0.831 corresponding to 20.3% overhead.

At the encoder stage, the input information bit sequences are demultiplexed into seven bit streams b_m^l, for $0 \leq l \leq 7$ and $0 \leq m < k$ where k is the length of information bits in each FEC codeword. The seven bit streams are then processed in parallel.

For the TPC case, each information bit stream b_m^l, with length k=27007, is placed in a 239×113 matrix. The rows are encoded by a BCH(128,113,6) code. Subsequently, the columns are encoded using a BCH(256,239,6) code, yielding a codeword length of 32768 bits, the structure of the TPC codeword is illustrated in Fig. 5.2 (a).

In the case of DVB-S2, the 7 bit streams, each with length 53840 bits, are first encoded by an outer BCH(54000,53840) codes. Following, the output bit streams are further encoded by an inner LDPC(64800,54000) codes, resulting in a 7 codewords, each having a length of 64800 bits.

Assuming the bit-to-symbol mapping reported in [164], the seven bits corresponding to a 4D symbol of the 128-SP-QAM format have different error probabilities in the uncoded case. Fig. 5.3 shows the 128-SP-QAM symbol bit indices as a function of the individual error rate of each bit. It can be noted that the 2nd, 4th and 6th bit, each has twice the number of errors as the adjacent bits. Therefore, the seven FEC coded bits streams are interleaved randomly in order to scramble the

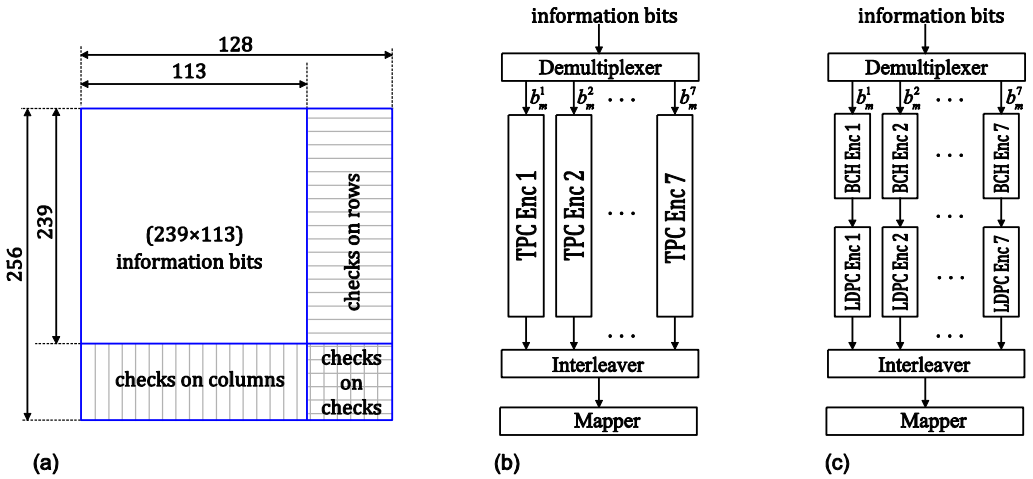

Fig. 5.2: (a) The structure of TPC codeword. The encoder block diagram for (b) TPC and (c) DVB-S2

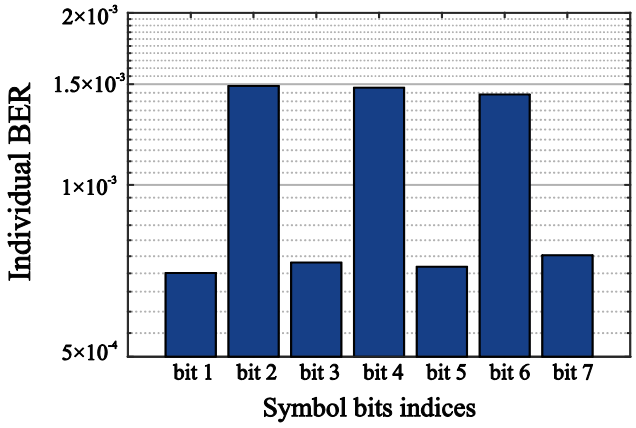

Fig. 5.3: Individual BER corresponding to 7 bits per 128-SP-QAM symbol calculated at average BER= 1×10^{-3}.

coded bits before mapping them into the 128-SP-QAM symbol alphabet. After the interleaver, the encoded bits are forwarded to a bit-to-symbol mapper. The block diagram of the encoder for the TPC and DVB-S2 schemes are shown in Fig. 5.2 (b) and (c), respectively.

At the decoder stage, a SISO decoder calculates the symbol log-likelihood ratios (LLRs) of the 4D symbols and then forwards them to the bit LLR calculators. The bit LLRs are then de-interleaved before being processed by either the TPC decoder or the LDPC decoder. The TPC decoder procedures are described in [228] where the number of test patterns is set to 31. These test patterns are generated based on the five least reliable bit positions. For the LDPC scenario, hard decision is performed after the last decoding iteration. The decoded bits are then forwarded into an outer BCH decoder to remove any errors left from the LDPC decoder stage [227].

5.1.3 Experimental Results

Fig. 5.4 shows the measured BER in back-to-back configuration as a function of OSNR (measured with 0.1 nm resolution bandwidth) for 128-SP-QAM. The results for PDM-16QAM at the same symbol rate of 28 GBd are reported as a reference. Comparing the experimental results for the uncoded case with results obtained by Monte Carlo simulations of an additive white Gaussian noise channel (solid lines), we observe an implementation penalty of 0.9 dB and 1.4 dB at a BER=10^{-3} for 128-SP-QAM and PDM-16QAM, respectively. The PDM-16QAM shows higher implementation penalty compared with 128-SP-QAM. This is attributed to the fact that the 128-SP-QAM has a larger minimum Euclidian distance between neighboring symbols, which makes it more resilient towards hardware imperfections [169]. Assuming a HD-FEC threshold at BER=3.8×10^{-3} with 7% FEC overhead [94], 128-SP-QAM shows 1.4 dB better sensitivity compared with PDM-16QAM. Comparing both formats at the SD-FEC threshold, which is typically assumed to be at BER= 2×10^{-2} at overhead slightly above 20%, a sensitivity gain of 1.1 dB of 128-SP-QAM over PDM-16QAM was measured.

For the coded 128-SP-QAM cases, two FEC scenarios were evaluated the TPC and LDPC. Comparing the two scenarios after 5 decoding iterations at BER=10^{-8}, TPC provides ~0.4 dB improvement in OSNR. On the other hand, increasing the maximum number of iterations from 5 to 25 will lead to 0.9 dB additional gain for LDPC and only 0.2 dB for TPC. LDPC then outperforms TPC by ~0.35 dB at BER = 10^{-8}. Further decoding iterations result in a negligible gain (<0.1 dB) in both scenarios. This indicates a faster convergence speed of TPC compared with LDPC, i.e. it requires less decoding iterations to converge to the error-free state.

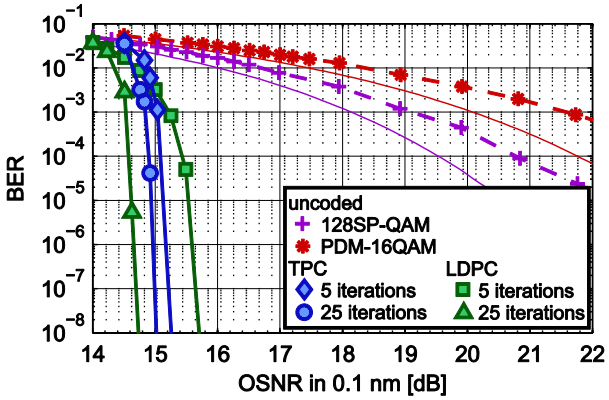

Fig. 5.4: Evaluated BER in a back-to-back measurement as a function of OSNR for 128-SP-QAM and PDM-16QAM at a symbol rate of 28GBd, without FEC decoding (dashed lines) and with FEC decoding for 128-SP-QAM (solid lines with markers). Simulation results in AWGN channel without FEC are also depicted as a reference for both formats (solid lines). © IEEE 2015 [174].

After 5 iterations, no errors were observed at pre-FEC BERs of 2.57×10^{-2} and 1.95×10^{-2} for TPC and LDPC, respectively. More than 2^{29} information bits were evaluated to estimate the post-FEC BER, which is corresponding to post-FEC BER < 2×10^{-9}. After 25 iterations, no errors were observed for pre-FEC BER of 3×10^{-2} and 3.35×10^{-2} for TPC and LDPC, respectively. However, it should be noted that the codeword length of LDPC is approximately twice as long as the one used for TPC.

TPC is well known for its rapid convergence, thus requiring a low number of iterations [96]. In order to investigate the convergence speed of the two FEC scenarios in more detail, the coding gain as a function of the number of decoding iterations at pre-FEC BER=10^{-5} is shown in Fig. 5.5. It is observed that for TPC, the coding gain improvement becomes negligible (<0.1 dB) after 10 iterations whereas for LDPC 20 iterations were required to achieve convergence. Furthermore, increasing the number of decoding iterations from 3 to 25 iterations improves the coding gain by 1.5 dB for LDPC code and only by 0.4 dB for TPC.

For the transmission experiment, Fig. 5.6 shows the measured BER vs. transmission distance for PDM-16QAM and 128-SP-QAM at the optimum launch power of -3 dBm per wavelength channel. Assuming a HD-FEC threshold at BER = 3.8×10^{-3}, a maximum reach of 1920 km and 1200 km is obtained for 128-SP-QAM and PDM-16QAM, respectively. Assuming a SD-FEC threshold at BER= 2×10^{-2}, a maximum reach of 3600 km and 2640 km is observed for uncoded 128-SP-QAM

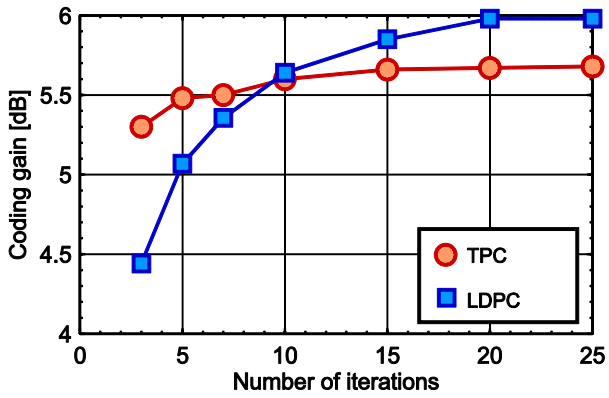

Fig. 5.5: Coding gain as a function of number of decoding iterations at pre-FEC BER= 1×10^{-5}. © IEEE 2015 [174].

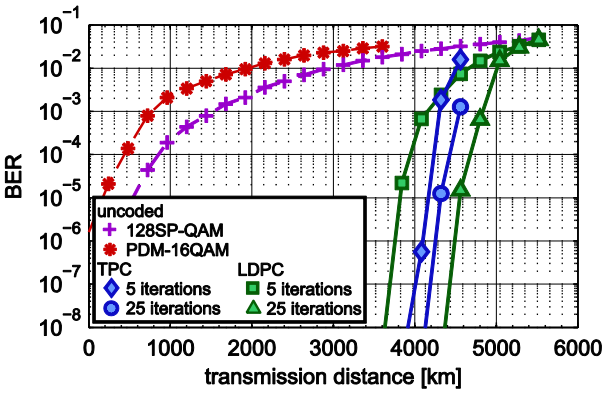

Fig. 5.6: Evaluated BER as a function of transmission distance for 128-SP-QAM and PDM-16QAM without FEC codes (dashed lines) and for 128-SP-QAM with FEC codes (solid lines). © IEEE 2015 [174].

and PDM-16QAM, respectively.

For 128-SP-QAM with FEC codes, we compare the two FEC schemes after 5 and 25 decoding iterations using $>2^{29}$ decoded bits for performance evaluation. After 5 iterations of TPC no errors were observed after 16 loop round-trips corresponding to 3840 km, performing 25 iterations yield a maximum reach increment by one loop round-trip to 4080 km. For LDPC case, a maximum reach of 3600 km is attained after 5 iterations. Increasing the number of iterations to 25 extends the transmission reach by 3 loop round-trips corresponding to a maximum reach of 4320 km.

Working at optimum launch power, at which the influences of nonlinear distortions and the amplified spontaneous emission noise are similarly high, suggests non optimal performance of the FEC codes were observed. This can be improved by using a non-linear mitigation technique [229].

5.1.4 Discussion

In this experiment, we have evaluated the 128-SP-QAM format in the presence of two FEC schemes: one scheme uses TPC based on BCH codes as constituent codes and the other scheme consists of a concatenation of an inner LDPC code and an outer BCH code. It is observed that the TPC-based solution converges faster than the LDPC-based solution to its optimum performance. However, after full convergence, LDPC shows 0.35 dB improvement in coding gain at BER = 10^{-8} compared with TPC. For the transmission experiment, no errors were observed after transmission over 3840 km and 3600 km and decoding more than 2^{29} bits with 5 iterations using TPC and LDPC, respectively. Increasing the number of decoding iterations to 25, results in an increase of the transmission reach by 240 km and 720 km for the considered TPC and LDPC, respectively.

5.2 Flexible Optical Transponders based on 4-D TCM and TTCM

In this section, we present an experimental investigation of the 4-D TCM and TTCM in an optical WDM transmission system. It should be noticed that this section is based on the Author's publication [87]. However, some more results and discussion are included.

5.2.1 Motivation and Introduction

The rapid growth in metro traffic would necessitate the development of elastic and cost-efficient optical transponders [10, 30]. To this end, coded modulations combined with simple FEC code are considered as a potential candidate to address these requirements [163].

Recently, 4-D TCM based on PDM-QPSK and 16QAM was demonstrated [230, 231], providing spectral efficiencies of 1.5 and 3.5 bits/symbol/polarization, respectively. An additional value of SE= 2.5 bits/symbol/polarization was realized in [230]. However, a different encoder structure was required to achieve such tuning. In addition, the reported scheme does not exploit the possible rotational invariance of multi-dimensional TCM for cycle slip tolerance. An approach using a rotationally-invariant 2-D TCM with 8-Gbd 64QAM signals and multi-level coding was shown recently in a real-time experiment [88].

In order to enhance the coding gain achieved by TCM and inspired by the turbo code principle, the iterative decoding technique was applied with TCM as constituent codes and is referred to as turbo TCM (TTCM) [224]. The TTCM scheme performs within 1 dB from the Shannon limit at BER levels of 10^{-4} to 10^{-5} [224]. In optical transmission systems, the performance of TTCM using a 2-D 8PSK as base constellation was evaluated [232]. Sensitivity gains of 2.8 dB and 3.8 dB were reported for TTCM compared with QPSK at HD-FEC limit for b2b and after 1000 km transmission, respectively.

In this work, a 4-D TCM scheme based on PDM-16QAM, PDM-32QAM and PDM-64QAM constellations is investigated experimentally at a symbol rate of 28 GBd. It enables the design of rate-adaptive optical transponders with a bitrate granularity of 25 Gb/s with a single encoder/decoder structure. Furthermore, the proposed and implemented scheme is invariant to 90° phase rotations. It is shown that for low-complexity 100GBASE-KP4 FEC [233], the implemented 4-D TCM outperforms standard PDM-*M*QAM formats at the same spectral efficiency. We also show that the 4-D TCM combined with HD-FEC defined in the ITU-T G.975.1 recommendation [94], could serve as an alternative to SD-FEC for complexity-performance trade-off [163]. Finally, the performance of 4-D TTCM based on PDM-*M*QAM is investigated. The b2b experimental result shows a sensitivity improvement of more than 1.5 dB for 4-D TTCM over 4-D TCM compared at the KP4 FEC limit. However, the sensitivity gain vanishes when 4-D TCM is concatenated with more powerful FEC code, e.g. G.975.1.

5.2.2 The structure of 4-D TCM scheme

A. The 4-D TCM Encoder

The implemented 4-D TCM is based on the 2-D *M*QAM signal set, where M is the number of signal states per 2-D signal set. The 4-D signal set is constructed as a 2-fold Cartesian product of the 2-D signal set, yielding a total number of M^2 signal states.

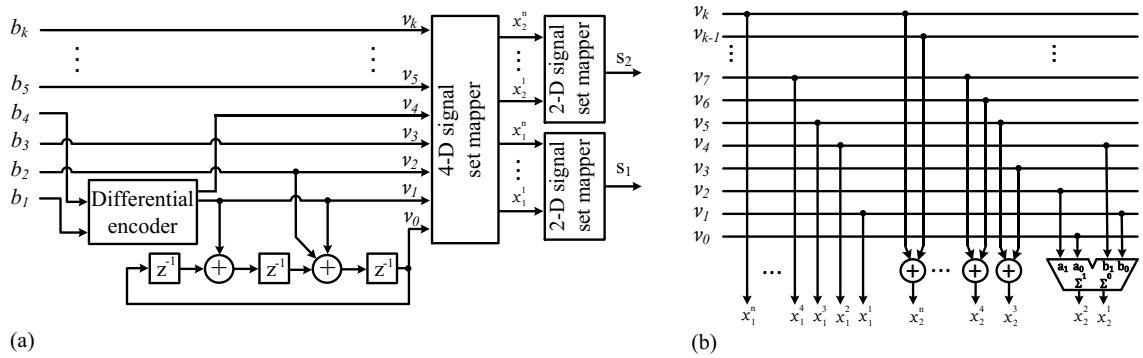

Fig. 5.7:(a) 4-D TCM encoder schematic for $\xi = 0$ and (b) 4-D TCM signal set mapper with *M*QAM signal for $\xi = 0$. © IEEE 2016 [87].

A block diagram of the proposed 4-D TCM encoder is shown in Fig. 5.7(a). The 4-D TCM encoder receives k information bits $[b_1, b_2, \dots, b_k]$ out of which two bits are encoded by a rate-2/3, 8-state linear convolutional encoder. The remaining bits remain uncoded. The resulting k+1 bits $[v_0, v_1, \dots, v_k]$ are mapped onto the 4-D signal set using two function blocks, the 4-D and 2-D signal set mapper.

The 4-D signal set mapper performs the signal set partitioning based on the multilevel block coding technique described in Section 4.3.3. The output bits of the 4-D signal set mapper $[x_1^1, \dots, x_1^n, x_2^1, \dots, x_2^n]$, where $n = log_2 M$ is the number of bits in each 2-D signal set, are then used to select two signal states s_1 and s_2 from the naturally mapped *M*QAM signal set. The obtained SE in bits per symbol per polarization is: $SE = k/2$, where $k = 2 \cdot n - 1 - \xi$ and $\xi \in \{0, 1\}$ refers to the partitioning level at which the bit-to-symbol mapping is applied, as discussed in Section 4.4. For $\xi = 0$ the encoded bits are mapped into the 4-D M^2-ary signal constellation, whereas for $\xi = 1$ the encoded bits are mapped into the 4-D M^2/2-ary subset obtained after one partition.

An important feature of 4-D TCM is the possibility to use a linear convolutional encoder in order to design a signal set which is transparent to various phase rotations. The implemented 4-D TCM formats are invariant to phase rotations of 90° and multiples thereof, making them more robust against cycle-slip events. Using the 4-D signal set mapper and the binary labeling discussed in [220] and in Section 4.5, only two bits are affected by multiple of 90° phase rotations for the 4-D TCM based on the *M*QAM signal set. Therefore two bits should be differentially encoded, whereas the remaining bits are unaffected. For $\xi = 0$, the affected bits are b_1 and b_4. For $\xi = 1$, the affected bits are b_3 and v_0.Fig. 5.7 (a) shows the 4-D TCM encoder block diagram for the case $\xi = 0$. For the case $\xi = 1$, the inputs of the differential encoder are switched to bits which are affected by the phase rotations, i.e. to b_3 and v_0.

The 4-D signal set mapper for $\xi = 0$ is implemented as following:

$$\begin{bmatrix} \boldsymbol{x}_1 \\ \boldsymbol{x}_2 \end{bmatrix} = \left[(2v_4 + v_1) \begin{bmatrix} 1 \\ 1 \end{bmatrix} + (2v_2 + v_0) \begin{bmatrix} 0 \\ 1 \end{bmatrix} (mod\ 4) \right] + 2^2 \left[v_5 \begin{bmatrix} 1 \\ 1 \end{bmatrix} \oplus v_3 \begin{bmatrix} 0 \\ 1 \end{bmatrix} \right] + \sum_{j=4}^{n} 2^{j-1} \left[v_{2j-1} \begin{bmatrix} 1 \\ 1 \end{bmatrix} \oplus v_{2j-2} \begin{bmatrix} 0 \\ 1 \end{bmatrix} \right] \tag{5-1}$$

Where $\boldsymbol{x}_d \in \{0,1, \dots, M-1\}$ with $d \in \{1, 2\}$, which represents the 2-D signal point in the naturally mapped *M*QAM signal set, is expressed as:

$$\boldsymbol{x}_d = \sum_{i=1}^{n} 2^{i-1} x_d^i \tag{5-2}$$

Fig. 5.7 (b) shows the block diagram of the 4-D signal set mapper for $\xi = 0$, which consists of few XOR gates and a modulo-4 adder.

Equation (5-1) can be modified for $\xi = 1$ by setting v_0 to zero and decreasing other bits indices by one. The mapping equation for $\xi = 1$ is then given as:

$$\begin{bmatrix} \boldsymbol{x}_1 \\ \boldsymbol{x}_2 \end{bmatrix} = \left[(2v_3 + v_0) \begin{bmatrix} 1 \\ 1 \end{bmatrix} + 2v_1 \begin{bmatrix} 0 \\ 1 \end{bmatrix} (mod\ 4) \right] + 2^2 \left[v_4 \begin{bmatrix} 1 \\ 1 \end{bmatrix} \oplus v_2 \begin{bmatrix} 0 \\ 1 \end{bmatrix} \right] + \sum_{j=4}^{n} 2^{j-1} \left[v_{2j-2} \begin{bmatrix} 1 \\ 1 \end{bmatrix} \oplus v_{2j-3} \begin{bmatrix} 0 \\ 1 \end{bmatrix} \right] \tag{5-3}$$

Accordingly, same logical gates can be used with some minor connections adjustment. The 4-D TCM Decoder

B. The 4-D TCM Decoder

For 4-D TCM decoding, a soft-input hard-output (SIHO) Viterbi algorithm is employed followed by a differential decoder for the bits which are affected by the phase rotations. The Viterbi algorithm is used to estimate the most likely transmitted symbol sequence. The squared Euclidian distances between each received 2-D symbol and the 2^n possible states in the 2-D signal set are computed. The soft metrics input to the Viterbi algorithm are the sum of squared Euclidian distances corresponding to each two received consecutive 2-D symbols. For the case of a rate-2/3, 8-state convolutional code, there are $2^2 \cdot 2^3 = 32$ distinct transitions per 4-D symbol for the Viterbi algorithm. Eight 4-way add-compare-select (ACS) operations are required for parallel processing, where each ACS operation involves 4 additions and 3 comparisons. For the subset decoding, a brute-force search to find the parallel transition with the best metric will not be a realistic option, especially for a large number of parallel transitions. Nevertheless, it is possible to perform the subset decoding with a similar complexity to a Viterbi-decoder, which significantly reduces the complexity compared with a brute-force approach [216].

5.2.3 Experimental setup and DSP

The experimental setup is similar to the one shown in Fig. 5.1 in Section 5.1.1. Seven ECLs on the 37.5 GHz ITU-T flexgrid [234] are used as light sources. The lasers are grouped into even and odd channels and modulated independently by integrated DP I/Q modulators. The modulators are driven by 28-GBd signals generated from two 4-channel DAC operating at a sample rate of 64 GS/s. The modulated optical signal is coupled into a recirculating fiber loop and received by a digital coherent optical receiver.

The DSP at the transmitter side includes the following: for the 4-D TCM/TTCM schemes, k random bit streams are encoded and mapped as described in the sections 5.2.2 and 4.6.1, respectively. For the PDM-*M*QAM formats, TPC was considered for FEC coding. At the information source $k + 1$ random bit streams are generated and encoded using two BCH codes, BCH(256,239,6) × BCH(128,113,6). The encoded bits are then mapped into *M*QAM symbols using Gray coding for the square constellation with *M*=16 and 64 and pseudo-Gray labelling for the cross-constellation with *M*=32. Afterwards, training sequences are inserted for the data-aided DSP

Table 5-1: Considered Modulation Formats with the corresponding information bit rate at a symbol rate of 28 Gbd.

Format	2-D signal set	Partitioning level ξ	SE (bits/sym/pol)	Line rate (Gb/s)	FEC+ Protocol OH	Information bit rate (Gb/s)
TCM-3.0 bits	16QAM	1	3.0	168	12%	150.0
TCM-3.5 bits	16QAM	0	3.5	196	12%	175.0
TCM-4.0 bits	32QAM	1	4.0	224	12%	200.0
TCM-4.5 bits	32QAM	0	4.5	252	12%	225.0
TCM-5.0 bits	64QAM	1	5.0	280	12%	250.0
TCM-5.5 bits	64QAM	0	5.5	308	12%	275.0
TTCM-3.5 bits	16QAM	0	3.5	196	12%	175.0
TTCM-4.5 bits	32QAM	0	4.5	252	12%	225.0
TTCM-5.5 bits	64QAM	0	5.5	308	12%	275.0
PDM-16QAM	16QAM	-	4.0	224	27.4%	175.8
PDM-32QAM	32QAM	-	5.0	280	27.4%	219.8
PDM-64QAM	64QAM	-	6.0	336	27.4%	263.7

at the receiver, followed by root-raised cosine pulse shaping with a roll-off factor of 0.14. Finally, the signal is up-sampled to 64 GS/s and digital nonlinear pre-distortion of the transfer characteristics of DAC, driver amplifiers and modulator is performed [235].

The DSP at the receiver consists of frontend correction followed by chromatic dispersion compensation, data-aided carrier frequency recovery, channel estimation and frequency domain equalization [75]. Carrier phase recovery is carried out based on the blind phase search algorithm [82]. For PDM-*M*QAM and TTCM, cycle slip mitigation is required and performed by pilot-aided phase unwrapping [85]. However, for 4-D TCM scheme, it is transparent to 90° phase rotations and thus inherently robust against cycle slip events. Therefore, the pilot-aided phase unwrapping is deactivated for processing of the 4-D TCM signals. At the decoder stage, the 4-D TCM/TTCM signals are decoded as described in sections 5.2.2 and 4.6.2, respectively. For TPC decoding, an iterative SISO algorithm is used followed by a hard-decision unit [228].

Table 5-1 summarizes the investigated formats with their corresponding information bit rates. The symbol rate was fixed to 28 GBd. 4-D TCM based on PDM-16QAM, PDM-32QAM and PDM-64QAM signals each with $\xi = [0, 1]$ was investigated, resulting in SE of 3.0, 3.5, 4.0, 4.5, 5.0 and 5.5 bits/symbol/polarization, in the following referred to as TCM-3.0bits, TCM-3.5bits, TCM-4.0bits, TCM-4.5bits, TCM-5.0bits and TCM-5.5bits, respectively. In addition, 4-D TTCM, employing TCM-3.5bits, TCM-4.5bits and TCM-5.5bits as component codes, was also investigated. It is referred to as TTCM-3.5bits, TTCM-4.5bits and TTCM-5.5bits, respectively. Operating at symbol rate of R_s= 28 GBd and assuming an overhead OH= 12% for outer HD-FEC including protocol overhead, the corresponding information bit rate R_b is calculated as: $R_b = \mathrm{nPol} \cdot R_s \cdot \frac{\mathrm{SE}}{1+\mathrm{OH}}$, where $\mathrm{nPol} = 2$ for polarization multiplexed signals, $R_s = 28\,\mathrm{GBd}$ is the symbol rate and OH= 12% is the overhead for an outer HD-FEC code including protocol overhead. Two reference HD-FEC codes were considered. The first one is the RS (544,514) defined in the 100GBASE-KP4 standard [233], with a pre-FEC BER threshold at 1.7×10^{-4}. The second code is defined by the ITU-T G.975.1 recommendation [94], with a pre-FEC BER threshold of 3.8×10^{-3}. PDM-*M*QAM formats combined with SD-FEC based on a TPC were also evaluated. A total overhead of 27.4% for SD-FEC and protocol overhead was considered.

5.2.4 Experimental results

First, the 4-D TCM/TTCM signals are evaluated in the b2b configuration. The required OSNR of these signals at two different HD-FEC limits are compared with required OSNR for conventional PDM-*M*QAM combined with TPC. Next, the effect of burst error events on the performance of 4-D TCM is investigated. Finally, the performance of 4-D TCM signals in WDM transmission experiments is presented.

A. B2B Measurement Results

Fig. 5.8 (a-c) shows the measured b2b BER as a function of OSNR measured in 0.1 nm resolution bandwidth, for the PDM-*M*QAM formats and the corresponding 4-D TCM. First the TCM formats are compared to their respective base PDM-*M*QAM formats. At the G.975.1 FEC threshold, it is observed that the TCM-3.5bits, TCM-4.5bits and TCM-5.5bits offer a sensitivity gain of 2.5 dB, 2.8 dB and 3.8 dB over PDM-16QAM, PDM-32QAM and PDM-64QAM, respectively, with SE reduction of 12.5%. Similarly, for TCM-3.0bits, TCM-4.0bits and TCM-5.0bits with a SE reduction of 25%, sensitivity gains of 4.3 dB, 4.7 dB and 6.8 dB were measured. It can be deduced that the 4-D TCM provides a smooth trade-off between SE and receiver sensitivity, which is desired for flexible optical transponders.

In order to investigate the penalty caused by the differential decoding of the two bits for the 4-D TCM schemes, the b2b BER is calculated with and without differential encoding/decoding. A modest penalty of 0.1 dB is measured for all cases.

Although the 4-D TCM formats provide significant sensitivity gains compared to their base PDM-*M*QAM formats, it is more interesting to compare 4-D TCM and PDM-*M*QAM formats at the same SE. For example, the TCM-4.0bits format is derived from the PDM-32QAM format. Despite the higher implementation penalty for PDM-32QAM compared with PDM-16QAM, the TCM-4.0bits format offers a sensitivity gain of 0.4 dB and 2.7 dB over PDM-16QAM at G.975.1 and KP4 FEC limits, respectively. For TCM-5.0bits, an OSNR advantage of 0.2 dB over PDM-32QAM was measured at the G.975.1 FEC limit. An error-floor was observed for PDM-32QAM format above the KP4 limit, while the TCM-5.0bits based on PDM-64QAM was able to significantly lower the error floor below the KP4 FEC limit.

The measured b2b post-FEC BER curves for PDM-*M*QAM formats with TPC and for TTCM

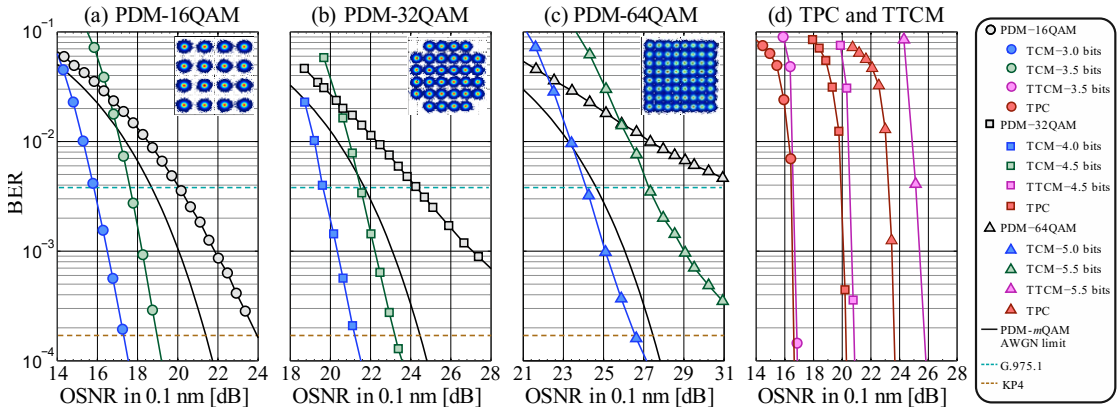

Fig. 5.8: (a)-(c) Measured back-to-back BER for uncoded PDM-*M*QAM (black symbols) as well as their theoretical limits (solid black lines), 4-D TCM with $\xi = 0$ (green symbols) and 4-D TCM with $\xi = 1$ (blue symbols). Insets show measured constellations in x-polarization for PDM-16QAM, PDM-32QAM and PDM-64QAM at maximum OSNR (~31 dB). (d) Measured b2b post-FEC BER for PDM-*M*QAM with TPC (red symbol) and for TTCM with KP4 code (violet symbol). © IEEE 2016 [87].

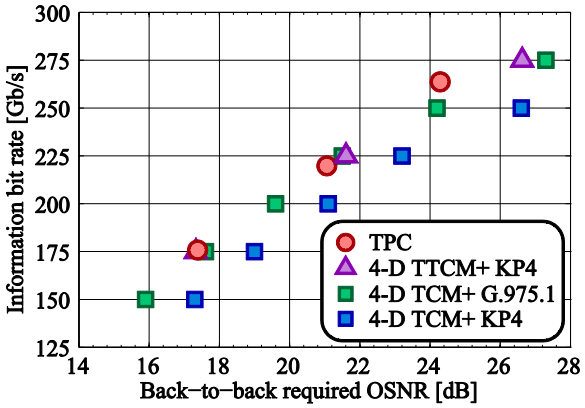

Fig. 5.9: Information bit rate as a function of b2b required OSNR for different modulation schemes. © IEEE 2016 [87].

concatenated with an outer KP4 code are shown in Fig. 5.8 (d). For TPC, five decoding iterations are used with 31 test error patterns based on the 5 least reliable bit positions. For TTCM scheme, symbol-by-symbol Log-MAP algorithm is used. The results are obtained after seven decoding iterations with an interleaver length of 5540. For each measured point, more than $2.6 \cdot 10^8$ bits are decoded with no error. It can be noticed, that PDM-16QAM with TPC attains the same performance as TTCM-3.5 bits with a KP4 FEC. However, for larger signal sets, the performance of TTCM degrades due to the increased number of parallel transitions, since the bits corresponding to these parallel transitions are left uncoded and thus will not profit from the turbo code principle. Hence, despite the slightly higher data rate for TTCM formats, the PDM-32QAM and PDM-64QAM formats combined with TPC provide 0.6 dB and 2.3 dB advantages over TTCM-4.5 bits and TTCM-5.5 bits, respectively.

Fig. 5.9 summarizes the b2b required OSNRs for different modulation schemes and different information bit rates. It can be noticed that the PDM-*M*QAM formats with TPC give the least required OSNR for a given information bit rate. However, the 4-D TCM concatenated with a HD-FEC can be considered for performance and complexity tradeoffs. For example, only a small sensitivity gain of 0.2 dB was measured for PDM-16QAM using a TPC FEC compared with TCM-3.5 bits concatenated with a G.975.1 FEC. A similar observation was also reported in [230]. A further reduction in complexity can be obtained by switching to the KP4 FEC as outer FEC, at the expense of 1.5 dB less OSNR sensitivity. Comparing the 4-D TCM/TTCM both concatenated with KP4, it is observed that the 4-D TTCM approach provides a sensitivity gain > 1.5 dB over 4-D TCM. However, 4-D TCM concatenated with a more powerful outer FEC (e.g. G.975.1) is able to obtain similar performance as TTCM.

B. The Impact of Burst Error Events in the Transmission Experiment

After the b2b characterization, transmission experiments were performed. In order to evaluate the performance in the presence of fiber nonlinearities, the fiber launch power is swept between -7 dBm to +3 dBm per channel. The BER for the PDM-32QAM format was measured after transmission over various distances. The optimal launch power is -3 dBm per channel.

It was observed that the histogram of symbol errors after transmission changes compared to the b2b configuration. In particular, for higher fiber launch powers more and longer error bursts are observed. To validate that behavior, the PDM-32QAM was evaluated in b2b configuration and after transmission at the fiber launch powers of -3 dBm and +2 dBm. The burst error histograms were evaluated at approximately the same symbol error rate (SER) of ~2.6×10^{-2} (BER of ~6×10^{-3}),

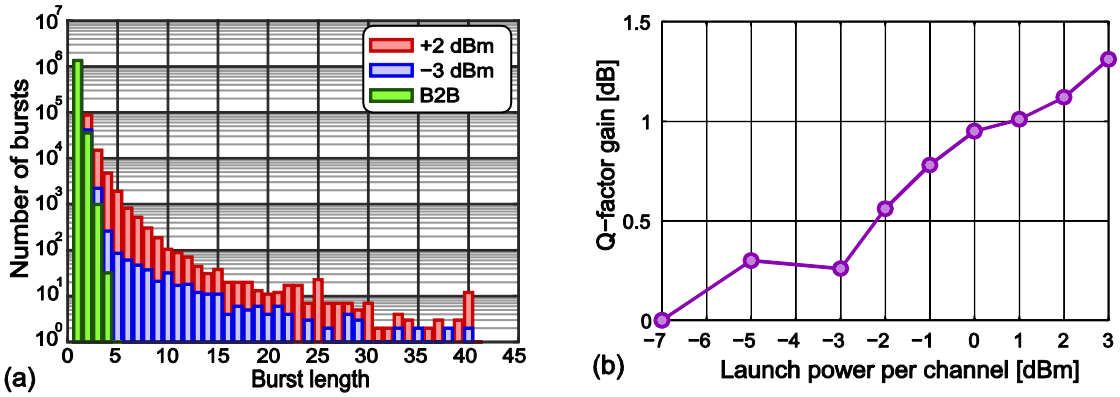

Fig. 5.10: (a) Number of error burst events as a function of burst length for the PDM-32QAM format in b2b configuration as well as for transmission at a fiber launch power of -3 dBm and +2 dBm per channel. (b) the Q-factor gains as function of fiber launch power per channel attained by introducing a channel interleaver for TCM.4.5bits format. © IEEE 2016 [87].

corresponding to a b2b required OSNR of 23.4 dB and transmission distances of 560 km and 240 km for -3 dBm and +2 dBm, respectively. Fig. 5.10 (a) shows the histogram of burst error occurrence versus the burst length. The burst length is defined as the number of consecutive erroneous symbols. The errors in b2b case tend to occur randomly, the longest burst error which was observed has a length of 5 consecutive erroneous symbols. In contrast, in the transmission scenario, a burst length up to 41 erroneous symbols was observed, where the higher launch power of 2 dBm shows more burst error events.

In order to investigate the impact of the burst error events on the performance of TCM, the TCM-4.5bits format was transmitted at different fiber launch powers. The BER of TCM-4.5bits and of the reference PDM-32QAM format were measured after transmission over various distances. Afterwards, the performance of TCM-4.5bits is compared for different fiber launch powers at approximately the same uncoded PDM-32QAM BER of ~6×10^{-3}. It was observed that the gain delivered by TCM decreases for increasing fiber launch power where the burst error events become more frequent. To mitigate this performance reduction of TCM, the encoded symbols are randomly interleaved before transmission and the received symbols are accordingly de-interleaved before the Viterbi decoder. The performance of TCM-4.5bits is evaluated with channel interleaver and then compared with the case without channel interleaver. Fig. 5.10 (b) shows the Q-factor gain obtained by employing a channel interleaver as a function of the fiber launch power. It shows that the Viterbi decoder took the advantages from spreading around the burst errored symbols and larger gain is obtained by interleaving technique at higher launch powers where the burst error events are more dominant.

C. Transmission Results

Fig. 5.11 shows the measured BER as a function of the transmission distance for the considered 4-D TCM formats and the corresponding base PDM-*M*QAM formats at the optimum launch power of -3 dBm per wavelength channel. All transmission measurements are taken with a channel interleaver to reduce the impact of the burst error events.

At the KP4 FEC limit, the achievable transmission distance for PDM-16QAM was 480 km, whereas for both PDM-32QAM and PDM-64QAM, the error floor measured in b2b was already above the KP4 FEC limit and no error-free transmission was possible. On the other hand, the achievable transmission distances for 4-D TCM formats were 2560 km, 1840 km, 880 km, 560 km,

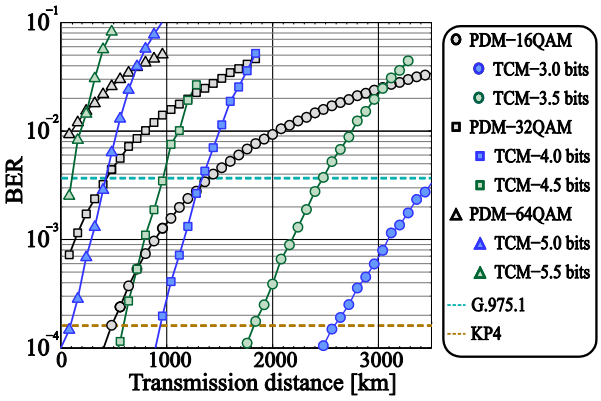

Fig. 5.11: Measured BER as a function of transmission distance for the considered 4-D TCM formats and the corresponding base PDM-*m*QAM formats at the optimum launch power of 3 dBm per wavelength channel. © IEEE 2016 [87].

and 80 km for TCM-3.0bits, TCM-3.5bits, TCM-4.0bits, TCM-4.5bits and TCM-5.0bits, respectively. However, no error-free transmission was possible for TCM-5.5bits assuming the KP4 FEC. As it can be noticed, the TCM-4.0bits format (based on PDM-32QAM) was able to extend the transmission reach by about 80% compared with PDM-16QAM at the same SE value. In addition, TCM-5.0bits (based on PDM-64QAM) enabled the transmission over 80km, whilst transmission using PDM-32QAM was not feasible. At the G.975.1 FEC limit, the 4-D TCM formats showed no advantages over standard PDM-*m*QAM formats for the same SE, which is partially attributed to the larger implementation penalties of higher order PDM-*M*QAM base formats.

The obtained maximum information bit rate as a function of reach is shown in Fig. 5.12. It can be seen that the 4-D TCM allows to trade-off smoothly between bit rate and transmission reach, while using a single low-complexity encoder. Using the low-complexity KP4 FEC, bit rates between 150 Gb/s and 250 Gb/s are supported for distances between 80 km and 2560 km, while for the G.975.1 FEC bit rates between 150 Gb/s and 275 Gb/s over 80 km to 3520 km are achieved.

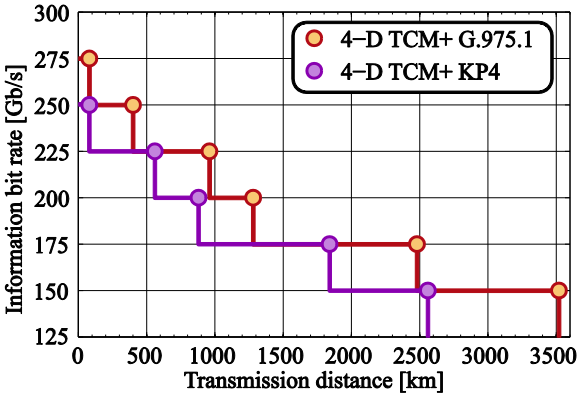

Fig. 5.12: Information bit rate vs. transmission distance for 4-D TCM concatenated with KP4 and G.975.1 FEC. © IEEE 2016 [87].

5.2.5 Discussion

The performance of a multi-rate optical transponder using 90° rotationally-invariant 4-D TCM based on PDM-*M*QAM formats was experimentally evaluated. Flexible SE was realized by using a single fixed encoder and decoder structure, which enables a fine granularity in bit rate and

transmission reach desired for flexible optical transponders. It was shown that 4-D TCM outperforms PDM-*M*QAM formats at the KP4 FEC limit for the same SE, which makes it particularly interesting for metro optical transport networks. Furthermore, it was discussed that 4-D TCM combined with more powerful FEC codes (e.g. those define by G.975.1 recommendation) are of a practical interest for providing trade-off options in complexity vs. performance compared to the SD-FEC approach. Finally, the performance of 4-D TTCM concatenated with an outer KP4 FEC code was experimentally investigated. The b2b results show that it achieves larger than 1.5 dB sensitivity gain over 4-D TCM with the same outer FEC. Nevertheless, similar performance was observed when 4-D TCM is concatenated with a G.975.1 FEC.

5.3 Author contribution related to this chapter

In this chapter, two system experiments were presented. In the first experiment, the 128-SP-QAM modulation format was evaluated in presence of two SD-FEC codes. I have implemented the TPC, prepared the necessary functions to evaluate the 128-SP-QAM format with the two FEC codes and carried out the experimental measurement.
In the second experiment, a multi-rate optical transponder was demonstrated based on 4-D TCM and TTCM. I have implemented the codes for multi-D TCM and TTCM schemes and performed the experiment.

CHAPTER 6

Conclusion

Throughout this thesis, multidimensional modulation formats for optical communication systems were investigated. The four degrees of freedom of the optical electromagnetic field (real and imaginary part in two orthogonal polarizations) enable us to construct power-efficient signal constellation in the 4-D space. Various optimized 4-D modulation formats are considered and discussed in details. These formats together with standard 2-D modulation formats enable a high degree of flexibility for future elastic transceivers. Moreover, 4-D TCM and TTCM are analyzed and evaluated in conjunction with FEC codes.

After a short introduction, the three basic components of digital coherent optical communication system were described, i.e. the optical transmitter, the fiber link and digital coherent receiver.

The main contents of the thesis can be classified into three parts:

In the first part, the task of finding the optimal placement of the signal points in the multidimensional space was considered. First, the concept of lattice and its properties was reviewed. Then, it was shown that a signal constellation with increased coding gain can be constructed by selecting its points from a dense lattice. It was briefly mentioned that, in addition to coding gain, shaping gain can be obtained geometrically by making the constellation's boundary as close as possible to a sphere; hence the maximum shaping gain is obtained for spherical boundaries. Focus was then directed on the 4-D space. It was discussed that the total nominal coding gain that can be achieved in the 4-D space is 1.96 dB, of which 1.51 dB is nominal coding gain and 0.45 dB shaping gain. Next, an elaborate discussion of some interesting 4-D modulation formats was presented, showing their potential performance advantages over their 2-D counterparts and reviewing the most related publications in the optical communication community. Following, three DSP algorithms for specific 4-D modulation formats were studied: 1- A joint-polarization CPE algorithm for PS-QPSK format was investigated. It was shown by numerical simulation that the tolerance to laser phase noise can be doubled by coupling the phase noise information between the two polarization components. Also, the tolerance to nonlinear distortions was examined in a NWDM transmission experiment, where it was noticed that the algorithm does not suffer in the presence of nonlinear impairments and shows comparable results to a decision-feedback equalizer. 2- A novel CPE algorithm for 6PolSK-QPSK signal was described. 3- An adaptive equalizer algorithm for 6PolSK-QPSK modulation format was proposed. In addition, a special way to initialize the filter coefficients which guarantees a fast convergence of the equalizer was suggested. The proposed algorithm has been found to perform well in both numerical simulations and transmission experiments.

Optimized 4-D modulation formats were found to be an interesting complement for standard modulation formats (i.e. PDM-*M*PSK and PDM-*M*QAM) for future BVT. These formats support fractional SEs and hence enable a smooth transition of the bit rate and reach based on the actual network demand [32]. Another attractive feature is their potential coding gain over conventional formats. The coding gain is more apparent at high SNR regime and vanishes as the SNR degraded; this is due to the increased number of nearest neighbors for multi-D modulation formats. Therefore, optimized 4-D modulation formats, especially those with large number of nearest neighbors, are

more practical for latency-constrained systems or low-complexity systems where no FEC or only a simple FEC code is employed [133].

The second part of the thesis deals with the coded modulations, which have been considered as an interesting approach to provide moderate coding gain while keeping the complexity reasonable. After introducing the fundamental of TCM schemes, their benefits and potential coding gain were presented. Then, the advantages of constructing TCM in the multidimensional space were discussed. Different techniques for designing good multidimensional TCM were considered, from which the MLC technique was adopted and described in details. In addition, it was shown that the rotationally invariant feature can be simply included in the signal design, which is particularly interesting for the optical communication system since it provides immunity against cycle slip events. Afterwards, in order to enhance the achievable coding gain of the TCM, the iterative decoding techniques combined with multidimensional TCM, i.e. TTCM, was explained.

The third part of the thesis reported two experimental demonstrations on the 4-D modulation formats. In the first experiment, the performance of 4-D 128-SP-QAM modulation format was investigated in a NWDM transmission system and compared with PDM-16QAM in b2b configuration and after transmission. In addition, two FEC scenarios were evaluated for the 128-SP-QAM, namely, the TPC employing two BCH component codes and LDPC concatenated with an outer BCH code. It was found that TPC grants faster conversion than LDPC, while the LDPC offers a small additional coding gain over TPC after the full convergence. In the second experiment, 4-D TCM based on PDM-*M*QAM was considered. A multi-rate optical transceiver was realized by a single encoder/decoder structure. Resilience against cycle-slip events was enabled by the rotational invariant feature of the 4-D TCM scheme. In addition, TTCM scheme was experimentally evaluated and its superior performance over TCM was validated. Furthermore, the performance of 4-D TCM and TTCM was compared with standard PDM-*M*QAM formats combined with the SD-FEC codes. It was shown that 4-D TCM concatenated with a low complexity HD-FEC could be an interesting candidate for complexity-performance tradeoff with SD-FEC.

For future research, it would be interesting to investigate coded modulations which take nonlinear impairments of the optical transmission channel into consideration. In such a way, a better performance can be attained, especially for systems with increased nonlinearity effects such as those with in-line dispersion compensation. This is currently an active topic for research and many groups have already assessed the capacity limit for nonlinear optical fiber [236, 237], in addition, some coded modulation schemes have been proposed to mitigate the influence of deterministic fiber nonlinearities, e.g. [238-240].

Another attractive topic for future research is the space division multiplexing (SDM) technique for optical communication systems. SDM is proposed as promising technique to scale up the capacity of optical networks [241]. It can be realized using multimode fibers, multicore fibers or a combination of both. Therefore, it would be important to design multidimensional modulation formats that are aware of the impairments presented in such multiple spatial channels medium.

Bibliography

[1] A. Einstein, “The quantum theory of radiation,” *Phys. Zeits*, vol. 18, p. 121, 1917.

[2] T. H. Maiman, “Stimulated Optical Radiation in Ruby,” *Nature*, vol. 187, no. 4736, pp. 493–494, 1960.

[3] R. N. Hall, G. E. Fenner, J. D. Kingsley, T. J. Soltys, and R. O. Carlson, “Coherent Light Emission From GaAs Junctions,” *Phys. Rev. Lett.*, vol. 9, no. 9, pp. 366–368, Nov 1962.

[4] G. Kao, K.C.; Hockham, “Dielectric-fibre surface waveguides for optical frequencies,” *Proc. of the Institution of Electrical Engineers*, vol. 113, no. 7, pp. 1151–1158, 1966.

[5] T. Miya, Y. Terunuma, T. Hosaka, and T. Miyashita, “Ultimate low-loss single-mode fibre at 1.55 μm,” *Electron Lett.*, vol. 15, no. 4, pp. 106–108, Feb. 1979.

[6] J. Chesnoy, *Undersea Fiber Communication Systems*. Academic Press, 2002.

[7] S. Abbott, “Review of 20 years of undersea optical fiber transmission system development and deployment since TAT-8,” in *Proc. 34th Eur. Conf. Opt. Commun. (ECOC)*, 2008, p. Mo.4.E.1.

[8] I. Kaminow, T. Li, and A. E. Willner, *Optical Fiber Telecommunications VB: Systems and Networks*. Elsevier, 2010.

[9] T. J. Xia, G. Wellbrock, B. Basch, S. Kotrla, W. Lee, T. Tajima, K. Fukuchi, M. Cvijetic, J. Sugg, Y. Ma, B. Turner, C. Cole, and C. Urricariet, “End-to-end native IP data 100G single carrier real time DSP coherent detection transport over 1520-km field deployed fiber,” in *Proc. Opt. Fiber Commun. Conf. (OFC)*, San Diego, CA, Mar. 2010.

[10] “Cisco visual networking index: Forecast and methodology, 2014-2019,” *Cisco White Paper, Cisco San Jose, CA, USAs*, 2015.

[11] M. V. Mazurczyk, D. Foursa, H. G. Batshon, H. Zhang, C. Davidson, J.-X. Cai, A. Pilipetskii, G. Mohs, and N. Bergano, “30 Tb/s Transmission over 6,630 km Using 16QAM Signals at 6.1 bits/s/Hz Spectral Efficiency,” in *Proc. 38th Eur. Conf. Opt. Commun. (ECOC)*, Amsterdam, Netherlands, 2012, p. Th.3.C.2.

[12] H. Zhang, J.-X. Cai, H. G. Batshon, M. Mazurczyk, O. Sinkin, D. Foursa, A. Pilipetskii, G. Mohs, and N. Bergano, “200 Gb/s and Dual Wavelength 400 Gb/s Transmission over Transpacific Distance at 6 b/s/Hz Spectral Efficiency,” in *Proc. Opt. Fiber Commun. Conf. (OFC)*. Optical Society of America, 2013, p. PDP5A.6.

[13] H. Masuda, E. Yamazaki, A. Sano, T. Yoshimatsu, T. Kobayashi, E. Yoshida, Y. Miyamoto, S. Matsuoka, Y. Takatori, M. Mizoguchi, K. Okada, K. Hagimoto, T. Yamada, and S. Kamei, “13.5-Tb/s (135 ×111-Gb/s/ch) no-guard-interval coherent OFDM transmission over 6,248 km using SNR maximized second-order DRA in the extended L-band,” in *Proc. Opt. Fiber Commun. Conf. (OFC)*, San Diego, CA, Mar. 2009, p. PDPB5.

[14] G. Charlet, M. Salsi, P. Tran, M. Bertolini, H. Mardoyan, J. Renaudier, O. Bertran-Pardo, and S. Bigo, “72 ×100Gb/s transmission over transoceanic distance, using large effective area fiber, hybrid Raman-Erbium amplification and coherent detection,” in *Proc. Opt. Fiber Commun. Conf. (OFC)*, San Diego, CA, Mar. 2009, p. PDPB6.

[15] J.-X. Cai, H. G. Batshon, M. Mazurczyk, O. V. Sinkin, D. Wang, M. Paskov, W. Patterson, C. Davidson, P. Corbett, G. wolter, T. Hammon, M. A. Bolshtyansky, D. Foursa, and A. Pilipetskii, “70.4 Tb/s Capacity over 7,600 km in C+L Band Using Coded Modulation with Hybrid

Constellation Shaping and Nonlinearity Compensation," in *Proc. Opt. Fiber Commun. Conf. (OFC)*, Los Angeles, CA, Mar. 2017, p. Th5B.2.

[16] J. X. Cai, Y. Cai, Y. Sun, C. R. Davidson, D. G. Foursa, A. Lucero, O. Sinkin, W. Patterson, A. Pilipetskii, G. Mohs, and N. S. Bergano, "112x112 Gb/s Transmission over 9,360 km with Channel Spacing Set to the Baud Rate (360% Spectral Efficiency)," in *Proc. 36th Eur. Conf. Opt. Commun. (ECOC)*, Torino, Italy, Sept. 2010, p. PD2.1.

[17] J. X. Cai, Y. Cai, C. R. Davidson, A. Lucero, H. Zhang, D. G. Foursa, O. V. Sinkin, W. W. Patterson, A. Pilipetskii, G. Mohs, and N. S. Bergano, "20 Tbit/s capacity transmission over 6,860 km," in *Proc. Opt. Fiber Commun. Conf. (OFC)*, Los Angeles, CA, Mar. 2011, p. PDPB4.

[18] D. Qian, M. F. Huang, S. Zhang, P. N. Ji, Y. Shao, F. Yaman, E. Mateo, T. Wang, Y. Inada, T. Ogata, and Y. Aoki, "Transmission of 115 ×100G PDM-8QAM-OFDM channels with 4bits/s/Hz spectral efficiency over 10,181km," in *Proc. 37th Eur. Conf. Opt. Commun. (ECOC)*, Geneva, Switzerland, 2011, p. Th.13.K.3.

[19] J.-X. Cai, Y. Cai, C. Davidson, D. Foursa, A. Lucero, O. Sinkin, W. Patterson, A. Pilipetskii, G. Mohs, and N. Bergano, "Transmission of 96x100G Pre-Filtered PDM-RZ-QPSK Channels with 300% Spectral Efficiency over 10,608km and 400% Spectral Efficiency over 4,368km," in *Proc. Opt. Fiber Commun. Conf. (OFC)*, San Diego, CA, Mar. 2010, p. PDPB10.

[20] J. X. Cai, H. G. Batshon, M. Mazurczyk, H. Zhang, Y. Sun, O. V. Sinkin, D. G. Foursa, and A. Pilipetskii, "64QAM based coded modulation transmission over transoceanic distance with >60 Tb/s capacity," in *Proc. Opt. Fiber Commun. Conf. (OFC)*, Los Angeles, CA, Mar. 2015, p. Th5C.8.

[21] D. G. Foursa, H. G. Batshon, H. Zhang, M. Mazurczyk, J. X. Cai, O. Sinkin, A. Pilipetskii, G. Mohs, and N. S. Bergano, "44.1 Tb/s transmission over 9,100 km using coded modulation based on 16QAM signals at 4.9 bits/s/Hz spectral efficiency," in *Proc. 39th Eur. Conf. Opt. Commun. (ECOC)*, London, UK, Sept 2013, p. PD3.E.1.

[22] M. Salsi, R. Rios-Muller, J. Renaudier, P. Tran, L. Schmalen, A. Ghazisaeidi, H. Mardoyan, P. Brindel, G. Charlet, and S. Bigo, "38.75 Tb/s transmission experiment over transoceanic distance," in *Proc. 39th Eur. Conf. Opt. Commun. (ECOC)*, London, UK, Sept. 2013, p. PD3.E.2.

[23] M. Salsi, H. Mardoyan, P. Tran, C. Koebele, E. Dutisseuil, G. Charlet, and S. Bigo, "155x100Gbit/s coherent PDM-QPSK transmission over 7.200km," in *Proc.35th Eur. Conf. Opt. Commun. (ECOC)*, Vienna, Austria, Sept. 2009, p. PD2.5.

[24] A. Ghazisaeidi, L. Schmalen, I. F. de Jauregui, P. Tran, C. Simonneau, P. Brindel, and G. Charlet, "52.9 Tb/s transmission over transoceanic distances using adaptive multi-rate FEC," in *Proc. 40th Eur. Conf. Opt. Commun. (ECOC)*, Cannes, France, Sept 2014, p. PD.3.4.

[25] J. X. Cai, Y. Sun, H. G. Batshon, M. Mazurczyk, H. Zhang, D. G. Foursa, and A. N. Pilipetskii, "54 Tb/s transmission over 9,150 km with optimized hybrid Raman-EDFA amplification and coded modulation," in *Proc. 40th Eur. Conf. Opt. Commun. (ECOC)*, Cannes, France, Sept. 2014, p. PD.3.3.

[26] J.-X. Cai, H. Zhang, H. G. Batshon, M. Mazurczyk, O. V. Sinkin, Y. Sun, A. Pilipetskii, and D. G. Foursa, "Transmission over 9,100 km with a Capacity of 49.3 Tb/s Using Variable Spectral Efficiency 16 QAM Based Coded Modulation," in *Proc. Opt. Fiber Commun. Conf. (OFC)*, San Francisco, CA, Mar. 2014, p. Th5B4.

[27] J. X. Cai, H. Batshon, H. Zhang, M. Mazurczyk, O. Sinkin, D. Foursa, A. Pilipetskii, G. Mohs, and N. Bergano, "30.4 Tb/s transmission over transpacific distance using 200 Gb/s and

dual wavelength 400 Gb/s 16QAM at 6.0 b/s/Hz spectral efficiency," *Opt. Express*, vol. 22, no. 8, pp. 9116–9122, 2014.

[28] S. Zhang, F. Yaman, Y. K. Huang, J. D. Downie, D. Zou, W. A. Wood, A. Zakharian, R. Khrapko, S. Mishra, V. Nazarov, J. Hurley, I. B. Djordjevic, E. Mateo, and Y. Inada, "Capacity-approaching transmission over 6375 km at spectral efficiency of 8.3 bit/s/Hz," in *Proc. Opt. Fiber Commun. Conf. (OFC)*, Anaheim, CA, Mar. 2016, p. Th5C.2.

[29] A. Ghazisaeidi, I. F. d. Jauregui Ruiz, R. Rios-Muller, L. Schmalen, P. Tran, P. Brindel, A. C. Meseguer, Q. Hu, F. Buchali, G. Charlet, and J. Renaudier, "65Tb/s Transoceanic Transmission Using Probabilistically-Shaped PDM-64QAM," in *Proc. 42th Eur. Conf. Opt. Commun. (ECOC)*, 2016, p. Th.3.C.4.

[30] A. Napoli, M. Bohn, D. Rafique, A. Stavdas, N. Sambo, L. Poti, M. Nölle, J. K. Fischer, E. Riccardi, A. Pagano, A. D. Giglio, M. S. Moreolo, J. M. Fabrega, E. Hugues-Salas, G. Zervas, D. Simeonidou, P. Layec, A. D'Errico, T. Rahman, and J. P. F. P. Giménez, "Next generation elastic optical networks: The vision of the European research project IDEALIST," *IEEE Commun. Mag.*, vol. 53, pp. 152–162, Feb. 2015.

[31] O. Gerstel, M. Jinno, A. Lord, and S. J. B. Yoo, "Elastic optical networking: a new dawn for the optical layer?" *IEEE Commun. Mag.*, vol. 50, pp. s12–s20, Feb. 2012.

[32] J. K. Fischer, S. Alreesh, R. Elschner, F. Frey, M. Nölle, C. Schmidt-Langhorst, and C. Schubert, "Bandwidth-Variable Transceivers based on Four-Dimensional Modulation Formats," *J. Lightw. Technol.*, vol. 32, pp. 2886–2895, Aug. 2014.

[33] S. Benedetto and E. Biglieri, *Principles of Digital Transmission: With Wireless Applications*, ser. Information Technology Series. Springer US, 1999.

[34] M. Seimetz, *High-Order Modulation for Optical Fiber Transmission*, 1st ed., ser. 143. Springer-Verlag Berlin Heidelberg, 2009.

[35] G. P. Agrawal, *Nonlinear Fiber Optics*, 4, Ed. Academic Press, 2006.

[36] ——, *Fiber-Optic Communication Systems*, 3rd ed. John Wiley & Sons, 2002.

[37] K. Roberts, A. Borowiec, and C. Laperle, "Technologies for optical systems beyond 100G," *Opt. Fiber Technol.*, vol. 17, p. 387–394, Oct. 2011.

[38] S. Ten, "Ultra low-loss optical fiber technology," in *Proc. Opt. Fiber Commun. Conf. (OFC)*, Anaheim, CA, Mar. 2016, p. Th4E.5.

[39] E. Desurvire, *Erbium-Doped Fiber Amplifiers: Principles and Applications*. New York: Wiley, 2002.

[40] P. Becker, A. Olsson, and J. Simpson, *Erbium-Doped Fiber Amplifiers: Fundamentals and Technology*. San Diego, CA: Academic Press, 1999.

[41] E. Ip and J. Kahn, "Digital Equalization of Chromatic Dispersion and Polarization Mode Dispersion," *J. Lightw. Technol.*, vol. 25, pp. 2033–2043, Aug 2007.

[42] ——, "Fiber Impairment Compensation Using Coherent Detection and Digital Signal Processing," *J. Lightw. Technol.*, vol. 28, no. 4, pp. 502–519, 2010.

[43] L. N. Binh, *Advanced Digital Optical Communications*, 2nd ed. CRC Press, 2015.

[44] D. Rafique, "Fiber Nonlinearity Compensation: Commercial Applications and Complexity Analysis," *J. Lightw. Technol.*, vol. 34, no. 2, pp. 544–553, Jan 2016.

[45] A. Carena, G. Bosco, V. Curri, P. Poggiolini, M. T. Taiba, and F. Forghieri, "Statistical Characterization of PM-QPSK Signals after Propagation in Uncompensated Fiber Links," in *Proc. 36th Eur. Conf. Opt. Commun. (ECOC)*, 2010, p. P.4.07.

[46] A. Splett, C. Kurtzke, and K. Petermann, “Ultimate transmission capacity of amplified fiber communication systems taking into account fiber nonlinearities,” in *Proc. 19th Eur. Conf. Opt. Commun. (ECOC)*, 1993, p. MoC2.4.

[47] K.-P. Ho, *Phase-Modulated Optical Communication Systems*, 1st ed. Springer US, 2005.

[48] S. Tsukamoto, D. S. Ly-Gagnon, K. Katoh, and K. Kikuchi, “Coherent demodulation of 40-Gbit/s polarization-multiplexed QPSK signals with 16-GHz spacing after 200-km transmission,” in *Proc. Opt. Fiber Commun. Conf. (OFC)*, Anaheim, CA, 2005, p. PDP29.

[49] K. Kikuchi, “Phase-diversity homodyne detection of multilevel optical modulation with digital carrier phase estimation,” *IEEE J. Sel. Topics Quantum Electron.*, vol. 12, no. 4, pp. 563–570, July 2006.

[50] K. Roberts, S. H. Foo, M. Moyer, M. Hubbard, A. Sinclair, J. Gaudette, and C. Laperle, “High Capacity Transport—100G and Beyond,” *J. Lightw. Technol.*, vol. 33, no. 3, pp. 563–578, 2015.

[51] S. Savory, “Digital Coherent Optical Receivers: Algorithms and Subsystems,” *IEEE J. Sel. Topics Quantum Electron.*, vol. 16, no. 5, pp. 1164–1179, Sept.-Oct. 2010.

[52] S. Alexander, “Design of wide-band optical heterodyne balanced mixer receivers,” *J. Lightw. Technol.*, vol. 5, no. 4, pp. 523–537, Apr. 1987.

[53] K. Kikuchi, “Fundamentals of coherent optical fiber communications,” *J. Lightw. Technol.*, vol. 34, no. 1, pp. 157–179, 2016.

[54] ——, *Coherent Optical Communications: Historical Perspectives and Future Directions*. Springer Berlin Heidelberg, 2010, pp. 11–49.

[55] J. Kahn and K.-P. Ho, “Spectral efficiency limits and modulation/detection techniques for DWDM systems,” *IEEE J. Sel. Topics Quantum Electron.*, vol. 10, no. 2, pp. 259 – 272, march-april 2004.

[56] F. Derr, “Optical QPSK transmission system with novel digital receiver concept,” *Electron Lett.*, vol. 27, no. 23, pp. 2177–2179, 1991.

[57] L. Kazovsky, R. Welter, A. F. Elrefaie, and W. Sessa, “Wide-linewidth phase diversity homodyne receivers,” *J. Lightw. Technol.*, vol. 6, no. 10, pp. 1527–1536, Oct. 1988.

[58] M. Seimetz and C. M. Weinert, “Options, feasibility, and availability of 2×4 90° hybrids for coherent optical systems,” *J. Lightw. Technol.*, vol. 24, no. 3, pp. 1317–1322, Mar. 2006.

[59] B. Glance, “Polarization independent coherent optical receiver,” *J. Lightw. Technol.*, vol. 5, no. 2, pp. 274–276, Feb. 1987.

[60] L. G. Kazovsky, “Phase- and polarization-diversity coherent optical techniques,” *J. Lightw. Technol.*, vol. 7, no. 2, pp. 279–292, Feb. 1989.

[61] I. Fatadin, S. J. Savory, and D. Ives, “Compensation of Quadrature Imbalance in an Optical QPSK Coherent Receiver,” *IEEE Photon. Technol. Lett.*, vol. 20, no. 20, pp. 1733–1735, Oct. 2008.

[62] Q. Sui, A. P. T. Lau, and C. Lu, “Fast and Robust Blind Chromatic Dispersion Estimation Using Auto-Correlation of Signal Power Waveform for Digital Coherent Systems,” *J. Lightw. Technol.*, vol. 31, no. 2, pp. 306–312, Jan 2013.

[63] H. Wymeersch and P. Johannisson, “Maximum-Likelihood-Based Blind Dispersion Estimation for Coherent Optical Communication,” *J. Lightw. Technol.*, vol. 30, no. 18, pp. 2976–2982, Sept 2012.

[64] M. Kuschnerov, F. Hauske, K. Piyawanno, B. Spinnler, M. Alfiad, A. Napoli, and B. Lankl, “DSP for Coherent Single-Carrier Receivers,” *J. Lightw. Technol.*, vol. 27, no. 16, pp. 3614–3622, Aug 2009.

[65] D. Godard, “Self-Recovering Equalization and Carrier Tracking in Two-Dimensional Data Communication Systems,” *IEEE Trans. Inf. Theory*, vol. 28, no. 11, pp. 1867–1875, Nov 1980.

[66] K. Kikuchi, “Polarization-demultiplexing algorithm in the digital coherent receiver,” in *IEEE/LEOS Summer Topical Meetings*, July 2008, p. MC2.2.

[67] S. J. Savory, “Digital filters for coherent optical receivers,” *Opt. Express*, vol. 16, no. 2, pp. 804–817, Jan 2008.

[68] I. Fatadin, D. Ives, and S. J. Savory, “Blind Equalization and Carrier Phase Recovery in a 16-QAM Optical Coherent System,” *J. Lightw. Technol.*, vol. 27, no. 15, pp. 3042–3049, Aug 2009.

[69] R. Johnson, P. Schniter, T. J. Endres, J. D. Behm, D. R. Brown, and R. A. Casas, “Blind equalization using the constant modulus criterion: a review,” *Proc. IEEE*, vol. 86, no. 10, pp. 1927–1950, Oct 1998.

[70] J. Yang, J. J. Werner, and G. A. Dumont, “The multimodulus blind equalization and its generalized algorithms,” *IEEE J. Sel. Areas Commun.*, vol. 20, no. 5, pp. 997–1015, Jun 2002.

[71] M. J. Ready and R. P. Gooch, “Blind equalization based on radius directed adaptation,” in *Proc. Int. Conf. Acoust., Speech, Signal Process.*, vol. 3, Apr 1990, p. 1699–1702.

[72] P. J. Winzer, A. H. Gnauck, C. R. Doerr, M. Magarini, and L. L. Buhl, “Spectrally Efficient Long-Haul Optical Networking Using 112-Gb/s Polarization-Multiplexed 16-QAM,” *J. Lightw. Technol.*, vol. 28, no. 4, pp. 547–556, Feb 2010.

[73] S. U. H. Qureshi, “Adaptive equalization,” *Proc. IEEE*, vol. 73, no. 9, p. 1349–1387, Sep. 1985.

[74] Y. Mori, C. Zhang, and K. Kikuchi, “Novel configuration of finite-impulse-response filters tolerant to carrier-phase fluctuations in digital coherent optical receivers for higher-order quadrature amplitude modulation signals,” *Opt. Express*, vol. 20, no. 24, pp. 26236–26251, Nov. 2012.

[75] R. Elschner, F. Frey, C. Meuer, S. A. J. Fischer, C. Schmidt-Langhorst, L. Molle, T. Tanimura, and C. Schubert, “Experimental demonstration of a format-flexible single-carrier coherent receiver using data-aided digital signal processing,” *opt. Express*, vol. 20, pp. 28786–28791, 2012.

[76] E. Ip and J. Kahn, “Feedforward Carrier Recovery for Coherent Optical Communications,” *J. Lightw. Technol.*, vol. 25, no. 9, pp. 2675 –2692, sept 2007.

[77] A. J. Viterbi and A. M. Viterbi, “Nonlinear Estimation of PSK-modulated Carrier Phase with Application to Burst Digital Transmission,” *IEEE Trans. Inf. Theor.*, vol. 29, no. 4, pp. 543–551, July 1983.

[78] M. Taylor, “Phase Estimation Methods for Optical Coherent Detection Using Digital Signal Processing,” *J. Lightw. Technol.*, vol. 27, no. 7, pp. 901 –914, april 2009.

[79] F. Rice, M. Rice, and B. Cowley, “A New Algorithm for 16QAM Carrier Phase Estimation Using QPSK Partitioning,” *Dig. Signal Process.*, vol. 12, no. 1, pp. 77–86, 2002.

[80] M. Seimetz, “Laser Linewidth Limitations for Optical Systems with High-Order Modulation Employing Feed Forward Digital Carrier Phase Estimation,” in *Proc. Opt. Fiber Commun. Conf. (OFC)*, San Diego, CA, Feb. 2008, p. OTuM2.

[81] I. Fatadin, D. Ives, and S. J. Savory, “Laser Linewidth Tolerance for 16-QAM Coherent Optical Systems Using QPSK Partitioning,” *IEEE Photon. Technol. Lett.*, vol. 22, no. 9, pp. 631–633, May 2010.

[82] T. Pfau, S. Hoffmann, and R. Noé, "Hardware-Efficient Coherent Digital Receiver Concept With Feedforward Carrier Recovery for M-QAM Constellations," *J. Lightw. Technol.*, vol. 27, no. 8, pp. 989–999, Apr 2009.

[83] Q. Zhuge, C. Chen, and D. V. Plant, "Low computation complexity two-stage feedforward carrier recovery algorithm for M-QAM,," in *Proc. Opt. Fiber Commun. Conf. (OFC)*, Los Angeles, CA, Mar. 2011, p. OMJ5.

[84] J. Li, L. Li, Z. Tao, T. Hoshida, and J. C. Rasmussen, "Laser-Linewidth-Tolerant Feed-Forward Carrier Phase Estimator With Reduced Complexity for QAM," *J. Lightw. Technol.*, vol. 29, no. 16, pp. 2358–2364, Aug. 2011.

[85] H. Cheng, Y. Li, F. Zhang, J. Wu, J. Lu, G. Zhang, J. Xu, and J. Lin, "Pilot-symbols-aided cycle slip mitigation for DP-16QAM optical communication systems," *Opt. Express*, vol. 21, no. 19, pp. 22166–22172, 2013.

[86] H. Zhang, Y. Cai, D. G. Foursa, and A. N. Pilipetskii, "Cycle Slip Mitigation in POLMUX-QPSK Modulation," in *Proc. Opt. Fiber Commun. Conf. (OFC)*, Los Angeles, CA, 2011, p. OMJ7.

[87] S. Alreesh, C. Schmidt-Langhorst, R. Emmerich, P. W. Berenguer, C. Schubert, and J. K. Fischer, "Four-Dimensional Trellis Coded Modulation for Flexible Optical Communications," *J. Lightw. Technol.*, vol. 35, no. 2, 2016.

[88] A. Bisplinghoff, N. Beck, M. Ene, M. Danninger, and T. Kupfer, "Phase Slip Tolerant, Low Power Multi-Level Coding for 64QAM with 12.9 dB NCG," in *Proc. Opt. Fiber Commun. Conf. (OFC)*, Anaheim, CA, 2016, p. M3A.2.

[89] C. E. Shannon, "Communication in the Presence of Noise," *Proc. IRE*, vol. 37, no. 1, pp. 10–21, Jan 1949.

[90] D. Costello and J. Forney, G.D., "Channel Coding: The Road to Channel Capacity," *Proceedings of the IEEE*, vol. 95, no. 6, pp. 1150–1177, June 2007.

[91] *ITU-T recommendation G.975: Forward error correction for submarine systems*, Int. Telecommun. Union Std., 2000.

[92] *ITU-T recommendation G.709/Y.1331: Interfaces for the optical transport network (OTN)*, Int. Telecommun. Union Std., Dec. 2009.

[93] J. Forney, G.D., "Concatenated codes," *Cambridge, MA: MIT Press*, 1966.

[94] *ITU-T recommendation G.975.1: Forward error correction for high bit-rate DWDM submarine systems*, Int. Telecommun. Union Std., 2004.

[95] P. Elias, "Error-free Coding," *IRE Trans. Inform. Theory*, vol. IT-4, no. 4, pp. 29– 37, 1954.

[96] A. Leven and L. Schmalen, "Status and recent advances on forward error correction technologies for lightwave systems," *J. Lightw. Technol.*, vol. 32, no. 16, pp. 2735–2750, 2014.

[97] S. Dave, L. Esker, F. Mo, W. Thesling, J. Keszenheimer, and R. Fuerst, "Soft-decision forward error correction in a 40-nm ASIC for 100-Gbps OTN applications," in *Proc. Opt. Fiber Commun. Conf. (OFC)*, Los Angeles, CA, 2011, p. JWA14.

[98] R. G. Gallager, "Low-Density Parity-Check Codes," *Cambridge, MA, USA: MIT Press*, 1963.

[99] T. Mizuochi, Y. Konishi, Y. Miyata, T. Inoue, K. Onohara, S. Kametani, T. Sugihara, K. Kubo, H. Yoshida, T. Kobayashi, and T. Ichikawa, "Experimental demonstration of concatenated ldpc and rs codes by fpgas emulation," *Photonics Technology Letters, IEEE*, vol. 21, no. 18, pp. 1302–1304, 2009.

[100] D. Chang, F. Yu, Z. Xiao, Y. Li, N. Stojanovic, C. Xie, X. Shi, X. Xu, and Q. Xiong, "FPGA verification of a single QC-LDPC code for 100 Gb/s optical systems without error floor

down to BER of 10^{-15}," in *Proc. Opt. Fiber Commun. Conf. (OFC)*, Los Angeles, CA, Mar. 2011, p. OTuN2.

[101] F. Chang, K. Onohara, and T. Mizuochi, "Forward error correction for 100 G transport networks," *IEEE Commun. Mag.*, vol. 48, no. 3, pp. S48–S55, 2010.

[102] G. Tzimpragos, C. Kachris, I. Djordjevic, M. Cvijetic, D. Soudris, and I. Tomkos, "A Survey on FEC Codes for 100G and Beyond Optical Networks," *IEEE Commun. Surveys Tuts.*, vol. 18, no. 1, pp. 209–221, 2014.

[103] B. Smith and F. Kschischang, "Future Prospects for FEC in Fiber-Optic Communications," *IEEE J. Sel. Topics Quantum Electron.*, vol. 16, no. 5, pp. 1245–1257, 2010.

[104] A. Tychopoulos, O. Koufopaulou, and I. Tomkos, "FEC in optical communications - A tutorial overview on the evolution of architectures and the future prospects of outband and inband FEC for optical communications," *IEEE Circuits Devices Mag.*, vol. 22, pp. 79–86, 2006.

[105] T. Mizuochi, "Recent progress in forward error correction and its interplay with transmission impairments," *IEEE J. Sel. Topics Quantum Electron.*, vol. 12, no. 4, pp. 544–554, 2006.

[106] J. G. Proakis and M. Salehi, *Digital Communications*, 5th ed. McGraw-Hill, 2008.

[107] "I.3 40G BCH Encoder/Decoder IP Core Specification," Iprium, Dec. 2016.

[108] "FEC IP Cores," Viasat, Cuyahoga Heights, OH, USA, ECC66100 Series.

[109] Z. Wang, C.-J. Chen, K. Xiao, H. Jiang, J. R. Fife, and S. Bhoja, "Communication device employing binary product coding with selective additional Cyclic Redundancy Check (CRC) therein," US Patent US20100241926 A1, 2010.

[110] Z. Wang, "Super-FEC Codes for 40/100 Gbps Networking," *IEEE Commun. Lett.*, vol. 16, no. 12, pp. 2056–2059, Dec. 2012.

[111] M. Scholten, T. Coe, and J. Dillard, "Continuously-interleaved bch (ci-bch) fec delivers best-in-class necg for 40g and 100g metro applications," in *Nat. Fiber Optic Engineers Conf.*, San Diego, CA, USA, Mar. 2010, p. NTuB3.

[112] D. Chang, F. Yu, Z. Xiao, N. Stojanovic, F. Hauske, Y. Cai, C. Xie, L. Li, X. Xu, and Q. Xiong, "LDPC convolutional codes using layered decoding algorithm for high speed coherent optical transmission," in *Proc. Opt. Fiber Commun. Conf. (OFC)*, Los Angeles, CA, Mar. 2012, p. OW1H.4.

[113] L. Schmalen, V. Aref, J. Cho, D. Suikat, D. Rösener, and A. Leven, "Spatially Coupled Soft-Decision Error Correction for Future Lightwave Systems," *J. Lightw. Technol.*, vol. 33, no. 5, pp. 1109–1116, Mar. 2015.

[114] J. Conway and N. J. A. Sloane, *Sphere Packings, Lattices and Groups*, 3rd ed. Springer-Verlag, New York, 1999.

[115] A. Calderbank and N. Sloane, "New Trellis Codes Based on Lattices and Cosets," *Information Theory, IEEE Transactions on*, vol. 33, no. 2, pp. 177–195, Mar 1987.

[116] G. Forney, R. Gallager, G. Lang, F. Longstaff, and S. Qureshi, "Efficient Modulation for Band-Limited Channels," *IEEE J. Sel. Areas Commun.*, vol. 2, no. 5, pp. 632 – 647, Sep 1984.

[117] G. Foschini, R. Gitlin, and S. Weinstein, "Optimization of Two-Dimensional Signal Constellations in the Presence of Gaussian Noise," *IEEE Trans. Commun.*, vol. 22, no. 1, pp. 28–38, 1974.

[118] R. L. Graham and N. J. A. Sloane, "Penny-packing and two-dimensional codes," *Discrete & Computational Geometry*, vol. 5, no. 1, pp. 1–11, 1990.

[119] E. Biglieri, *Advanced modulation formats for satellite communications*. Springer Berlin Heidelberg, 1992, ch. Advanced Methods for Satellite and Deep Space Communications, pp. 61–80.

[120] M. Karlsson and E. Agrell, "Which is the most power-efficient modulation format in optical links?" *Opt. Express*, vol. 17, no. 13, pp. 10814–10819, Jun 2009.

[121] J. Forney, G.D., "Coset codes. I. Introduction and geometrical classification," *IEEE Trans. Inf. Theory*, vol. 34, no. 5, pp. 1123–1151, Sep 1988.

[122] J. Forney, G.D. and L.-F. Wei, "Multidimensional constellations. I. Introduction, figures of merit, and generalized cross constellations," *IEEE J. Sel. Areas Commun.*, vol. 7, no. 6, pp. 877–892, 1989.

[123] J. Forney, G.D. and G. Ungerboeck, "Modulation and coding for linear Gaussian channels," *IEEE Trans. Inf. Theory*, vol. 44, no. 6, pp. 2384–2415, Oct 1998.

[124] S. G. Wilson, H. A. Sleeper, and N. K. Srinath, "Four-dimensional modulation and coding - An alternate to frequency-reuse," in *IEEE International Conference on Communications ICC*, Amsterdam, Netherlands, 1984, pp. 919–923.

[125] N. J. A. Sloane, R. H. Hardin, T. D. S. Duff, and J. H. Conway, "Minimal-energy clusters," http://neilsloane.com/cluster/, accessed: 2016-08-25.

[126] J. E. Porath and T. Aulin, "Design of multidimensional signal constellations," *IEE Proceedings - Communications*, vol. 150, no. 5, pp. 317–323, Oct 2003.

[127] T. Koike-Akino and V. Tarokh, "Sphere packing optimization and exit chart analysis for multi-dimensional qam signaling," in *IEEE ICC, Dresden, Germany*, 2009, pp. 3888–3892.

[128] L. Zetterberg and H. Brandstrom, "Codes for Combined Phase and Amplitude Modulated Signals in a Four-Dimensional Space," *IEEE Trans. Commun.*, vol. 25, no. 9, pp. 943–950, Sep 1977.

[129] G. Welti and J. Lee, "Digital transmission with coherent four-dimensional modulation," *IEEE Trans. Inf. Theory*, vol. 20, no. 4, p. 497/502, Jul 1974.

[130] E. Agrell and M. Karlsson, "Power-Efficient Modulation Formats in Coherent Transmission Systems," *J. Lightw. Technol.*, vol. 27, no. 22, pp. 5115–5126, Nov 2009.

[131] E. Agrell, "Database of sphere packings," https://codes.se/packings/, accessed: 2016-08-25.

[132] M. Karlsson and E. Agrell, *Power-Efficient Modulation Schemes*. New York, NY: Springer New York, 2011, pp. 219–252.

[133] ——, "Spectrally efficient four-dimensional modulation," in *Proc. Opt. Fiber Commun. Conf. (OFC)*, Los Angeles, CA, 2012, p. OTu2C.1.

[134] C. Campopiano and B. Glazer, "A Coherent Digital Amplitude and Phase Modulation Scheme," *IRE Transactions on Communications Systems*, vol. 10, no. 1, pp. 90–95, 1962.

[135] B. Krongold, T. Pfau, N. Kaneda, and S. C. J. Lee, "Comparison Between PS-QPSK and PDM-QPSK With Equal Rate and Bandwidth," *IEEE Photon. Technol. Lett.*, vol. 14, pp. 203–205, Feb 2012.

[136] D. Saha and T. Birdsall, "Quadrature-quadrature phase-shift keying," *Communications, IEEE Transactions on*, vol. 37, no. 5, pp. 437 –448, may 1989.

[137] S. Betti, F. Curti, G. De Marchis, and E. Iannone, "A novel multilevel coherent optical system: 4-quadrature signaling," *J. Lightw. Technol.*, vol. 9, no. 4, pp. 514–523, 1991.

[138] M. Sjödin, B. J. Puttnam, P. Johannisson, S. Shinada, N. Wada, P. A. Andrekson, and M. Karlsson, "Transmission of PM-QPSK and PS-QPSK with different fiber span lengths," *Opt. Express*, vol. 20, no. 7, pp. 7544–7554, Mar 2012.

[139] L. E. Nelson, X. Zhou, N. M. Suibhne, A. D. Ellis, and P. Magill, "Experimental comparison of coherent polarization-switched QPSK to polarization-multiplexed QPSK for 10 100 km WDM transmission," *Opt. Express*, vol. 19, no. 11, pp. 10849–10856, May 2011.

[140] D. S. Millar, D. Lavery, S. Makovejs, C. Behrens, B. C. Thomsen, P. Bayvel, and S. J. Savory, "Generation and long-haul transmission of polarization-switched QPSK at 42.9 Gb/s," *Opt. Express*, vol. 19, no. 10, pp. 9296–9302, May 2011.

[141] D. Lavery, C. Behrens, S. Makovejs, D. S. Millar, R. I. Killey, S. J. Savory, and P. Bayvel, "Long-Haul Transmission of PS-QPSK at 100 Gb/s Using Digital Backpropagation," *IEEE Photon. Technol. Lett.*, vol. 24, no. 3, pp. 176–178, 2012.

[142] J. K. Fischer, L. Molle, M. Nölle, D.-D. Groß, C. Schmidt-Langhorst, and C. Schubert, "Experimental investigation of 84-Gb/s and 112-Gb/s polarization-switched quadrature phase-shift keying signals," *Opt. Express*, vol. 19, no. 26, pp. B667–B672, Dec 2011.

[143] M. Nölle, J. K. Fischer, L. Molle, C. Schmidt-Langhorst, D. Peckham, and C. Schubert, "Comparison of 8 112 Gb/s PS-QPSK and PDM-QPSK signals over transoceanic distances," *Opt. Express*, vol. 19, no. 24, pp. 24370–24375, Nov 2011.

[144] P. Serena, A. Vannucci, and A. Bononi, "The performance of polarization switched-QPSK (PS-QPSK) in dispersion managed WDM transmissions," in *Proc. 36th Eur. Conf. Opt. Commun. (ECOC)*, 2010, p. Th.10.E.2.

[145] P. Poggiolini, G. Bosco, A. Carena, V. Curri, and F. Forghieri, "Performance evaluation of coherent WDM PS-QPSK (HEXA) accounting for non-linear fiber propagation effects," *Opt. Express*, vol. 18, no. 11, pp. 11360–11371, May 2010.

[146] G. Bosco and A. Carena, "Performance Evaluation of Coherent PS-QPSK (HEXA) Modulation," in *Signal Processing in Photonic Communications (SPPCom) Toronto, Canada*, 2011, p. SPTuB2.

[147] E. Dutisseuil, J. M. Tanguy, A. Voicila, J. Renaudier, and G. Charlet, "21 Gb/s Polarization Switched-QPSK Real-Time Coherent FPGA-based Receiver," in *Proc. Opt. Fiber Commun. Conf. (OFC)*, Anaheim, CA, 2013, p. OW1E.2.

[148] "The photonic service engine 2," http://resources.alcatel-lucent.com/?cid=194079, 2016, accessed: 2016-09-01.

[149] G. Taricco, E. Biglieri, and V. Castellani, "Applicability of four-dimensional modulations to digital satellites: a simulation study," in *Global Telecommunications Conference*, vol. 4, 1993, pp. 28 –34.

[150] H. Bülow, "Polarization QAM modulation (POL-QAM) for coherent detection schemes," in *Proc. Opt. Fiber Commun. Conf. (OFC)*, San Diego, CA, USA, Mar. 2009, p. OWG2.

[151] E. Agrell and M. Karlsson, "On the Symbol Error Probability of Regular Polytopes," *IEEE Trans. Inf. Theory*, vol. 57, no. 6, pp. 3411–3415, 2011.

[152] R. Laroia, N. Farvardin, and S. A. Tretter, "On optimal shaping of multidimensional constellations," *IEEE Trans. Inf. Theory*, vol. 40, no. 4, pp. 1044–1056, Jul. 1994.

[153] F. Buchali and H. Bülow, "Experimental transmission with POLQAM and PS-QPSK modulation format using a 28-Gbaud 4-D transmitter," in *Proc. 38th Eur. Conf. Opt. Commun. (ECOC)*, 2012, p. We.3.A.1.

[154] J. K. Fischer, S. Alreesh, R. Elschner, F. Frey, C. Meuer, L. Molle, C. Schmidt-Langhorst, T. Tanimura, and C. Schubert, "Experimental Investigation of 126-Gb/s 6PolSK-QPSK Signals," in *Proc. 38th Eur. Conf. Opt. Commun. (ECOC)*, 2012, p. We.1.C.4.

[155] H. Bülow, X. Lu, and L. Schmalen, “Experimental analysis of single carrier POLQAM (6Pol-QPSK) transmission with soft-decoding,” in *Proc. 39th Eur. Conf. Opt. Commun. (ECOC)*, Sept. 2013, p. Mo.4.D.2.

[156] J. K. Fischer, S. Alreesh, R. Elschner, F. Frey, C. Meuer, L. Molle, C. Schmidt-Langhorst, T. Tanimura, and C. Schubert, “Experimental Investigation of 126-Gb/s 6PolSK-QPSK signals,” *Opt. Express*, vol. 20, no. 26, pp. B232–B237, Dec 2012.

[157] H. Bülow, “Ideal POL-QAM Modulation for Coherent Detection Schemes,” in *Signal Processing in Photonic Communications*, 2011, p. SPTuB1.

[158] H. Bülow, U. Abay, A. Schenk, and J. Huber, “Coded modulation of polarization- and space-multiplexed signals,” in *Proc. Asia Commun. & Photonics Conf. (ACP)*, Shanghai, China, Nov. 2011, p. 83090W.

[159] T. Tanimura, S. Alreesh, J. K. Fischer, C. Schmidt-Langhorst, F. Frey, C. Meuer, R. Elschner, L. Molle, and C. Schubert, “Nonlinear transmission of 6PolSK-QPSK signals using coded modulation and digital back propagation,” in *Proc. Opt. Fiber Commun. Conf. (OFC)*, Anaheim, CA, 2013, p. OTu3B.3.

[160] G. Ungerboeck, “Channel coding with multilevel/phase signals,” *IEEE Trans. Inf. Theory*, vol. 28, no. 1, pp. 55 – 67, Jan. 1982.

[161] L. Coelho and N. Hanik, “Global Optimization of Fiber-Optic Communication Systems using Four-Dimensional Modulation Formats,” in *Proc. 37th Eur. Conf. Opt. Commun. (ECOC)*, Geneva, Switzerland, 2011, p. Mo.2.B.4.

[162] S. Gringeri, N. Bitar, and T. J. Xia, “Extending software defined network principles to include optical transport,” *IEEE Commun. Mag.*, vol. 51, no. 3, pp. 32–40, Mar. 2013.

[163] D. A. Morero, M. A. Castrillón, A. Aguirre, M. R. Hueda, and O. E. Agazzi, “Design tradeoffs and challenges in practical coherent optical transceiver implementations,” *J. Lightw. Technol.*, vol. 34, no. 1, pp. 121–136, Jan. 2016.

[164] J. Renaudier, A. Voicila, O. Bertran-Pardo, O. Rival, M. Karlsson, G. Charlet, and S. Bigo, “Comparison of Set-Partitioned Two-Polarization 16QAM Formats with PDM-QPSK and PDM-8QAM for Optical Transmission Systems with Error-Correction Coding,” in *Proc. 38th Eur. Conf. Opt. Commun. (ECOC)*, Amsterdam, Netherlands, 2012, p. We.1.C.5.

[165] J. K. Fischer, C. Schmidt-Langhorst, S. Alreesh, R. Elschner, F. Frey, P. W. Berenguer, L. Molle, M. Nölle, and C. Schubert, “Transmission of 512SP-QAM Nyquist-WDM signals,” in *Proc. 40th Eur. Conf. Opt. Commun. (ECOC)*, Sept. 2014, p. Tu.3.3.2.

[166] J. K. Fischer, C. Schmidt-Langhorst, S. Alreesh, R. Elschner, F. Frey, P. W. Berenguer, L. Molle, M. Nölle, and C. Schubert, “Generation, Transmission, and Detection of 4-D Set-Partitioning QAM Signals,” *J. Lightwave Technol.*, vol. 33, no. 7, pp. 1445–1451, Apr 2015.

[167] J. Conway and N. Sloane, “Fast quantizing and decoding and algorithms for lattice quantizers and codes,” *IEEE Trans. Inf. Theory*, vol. 28, no. 2, pp. 227–232, Mar 1982.

[168] M. Sjödin, P. Johannisson, J. Li, E. Agrell, P. A. Andrekson, and M. Karlsson, “Comparison of 128-SP-QAM with PM-16-QAM,” *Opt. Express*, vol. 20, no. 8, pp. 8356–8366, 2012.

[169] T. A. Eriksson, M. Sjödin, P. Johannisson, P. A. Andrekson, and M. Karlsson, “Comparison of 128-SP-QAM and PM-16QAM in long-haul WDM transmission,” *Opt. Express*, vol. 21, no. 16, pp. 19269–19279, Aug 2013.

[170] J. Renaudier, O. Bertran-Pardo, A. Ghazisaeidi, P. Tran, H. Mardoyan, P. Brindel, A. Voicila, G. Charlet, and S. Bigo, “Experimental Transmission of Nyquist Pulse Shaped 4-D

Coded Modulation using Dual Polarization 16QAM Set-Partitioning Schemes at 28 Gbaud," in *Proc. Opt. Fiber Commun. Conf. (OFC)*, Anaheim, CA, March 2013, p. OTu3B.1.

[171] R. Rios-Muller, J. Renaudier, O. Bertran-Pardo, A. Ghazisaeidi, P. Tran, G. Charlet, and S. Bigo, "Experimental comparison between Hybrid-QPSK/8QAM and 4D-32SP-16QAM formats at 31.2 GBaud using Nyquist pulse shaping," in *Proc. 39th Eur. Conf. Opt. Commun. (ECOC)*, London, United Kingdom, 2013, p. Th.2.D.2.

[172] H. Sun, R. Egorov, B. Basch, J. McNicol, and K.-T. Wu, "Comparison of two modulation formats at spectral efficiency of 5 bits/dual-pol symbol," in *Optical Communication (ECOC 2013), 39th European Conference and Exhibition on*, 2013, p. Th.2.D.3.

[173] H. Zhang, J.-X. Cai, H. G. Batshon, C. R. Davidson, Y. Sun, M. Mazurczyk, D. G. Foursa, A. Pilipetskii, G. Mohs, and N. S. Bergano, "16QAM transmission with 5.2 bits/s/Hz spectral efficiency over transoceanic distance," *Opt. Express*, vol. 20, no. 11, pp. 11688–11693, May 2012.

[174] S. Alreesh, C. Schmidt-Langhorst, F. Frey, P. W. Berenguer, C. Schubert, and J. K. Fischer, "Transmission Performance of 4D 128SP-QAM With Forward Error Correction Coding," *IEEE Photon. Technol. Lett.*, vol. 27, no. 7, pp. 744–747, Apr. 2015.

[175] S. Alreesh, C. Schmidt-Langhorst, R. Elschner, F. Frey, P. W. Berenguer, L. Molle, M. Noelle, C. Schubert, and J. K. Fischer, "Transmission of 2048SP-QAM Nyquist-WDM signals," in *Proc. 16. ITG-Fachtagung Photonische Netze*, Leipzig, May 2015, pp. 88–91.

[176] H. Zhang, H. G. Batshon, D. G. Foursa, M. Mazurczyk, J. X. Cai, C. R. Davidson, A. Pilipetskii, G. Mohs, and N. S. Bergano, "30.58 Tb/s Transmission Over 7,230 Km Using PDM Half 4D-16QAM Coded Modulation with 6.1 B/s/Hz Spectral Efficiency," in *Proc. Opt. Fiber Commun. Conf. (OFC)*, Anaheim, CA, March 2013, p. OTu2B.3.

[177] M. Karlsson and E. Agrell, *Power-Efficient Modulation Schemes*. New York, NY: Springer New York, 2011, ch. 5, pp. 219–252.

[178] ——, "Four-dimensional optimized constellations for coherent optical transmission systems," in *Proc. 36th Eur. Conf. Opt. Commun.*, Torino, Italy, Sept. 2010, p. We.8.C.3.

[179] J. Karout, X. Liu, C. Sethumadhavan, E. Agrell, M. Karlsson, and R.-J. Essiambre, "Experimental Demonstration of an Optimized 16-ary Four-Dimensional Modulation Format Using Optical OFDM," in *Proc. Opt. Fiber Commun. Conf. (OFC)*, Anaheim, CA, USA, Mar. 2013, p. OW3B.4.

[180] H. Bülow, T. Rahman, F. Buchali, W. Idler, and W. Kuebart, "Transmission of 4-D modulation formats at 28-Gbaud," in *Proc. Opt. Fiber Commun. Conf. (OFC)*, Anaheim, CA, Mar. 2013, p. JW2A.39.

[181] J. Conway and N. Sloane, "A fast encoding method for lattice codes and quantizers," *IEEE Trans. Inf. Theory*, vol. 29, no. 6, pp. 820–824, 1983.

[182] T. A. Eriksson, S. Alreesh, C. Schmidt-Langhorst, F. Frey, P. W. Berenguer, C. Schubert, J. K. Fischer, P. A. Andrekson, M. Karlsson, and E. Agrell, "Experimental investigation of a four-dimensional 256-ary lattice-based modulation format," in *Proc. Opt. Fiber Commun. Conf. (OFC)*, Los Angeles, CA, Mar. 2015, p. W4K.3.

[183] A. R. Calderbank and L. H. Ozarow, "Nonequiprobable signaling on the Gaussian channel," *IEEE Transactions on Information Theory*, vol. 36, no. 4, pp. 726–740, 1990.

[184] H. Bülow, X. Lu, L. Schmalen, A. Klekamp, and F. Buchali, "Experimental Performance of 4D Optimized Constellation Alternatives for PM-8QAM and PM-16QAM," in *Proc. Opt. Fiber Commun. Conf. (OFC)*, San Francisco, CA, 2014, p. M2A.6.

[185] J. Forney, G.D., "Coset codes. II. Binary lattices and related codes," *IEEE Trans. Inf. Theory*, vol. 34, no. 5, pp. 1152–1187, 1988.

[186] D. Millar, T. Koike-Akino, R. Maher, D. Lavery, M. Paskov, K. Kojima, K. Parsons, B. Thomsen, S. J. Savory, and P. Bayvel, "Experimental Demonstration of 24-Dimensional Extended Golay Coded Modulation with LDPC," in *Proc. Opt. Fiber Commun. Conf. (OFC)*, San Francisco, CA, Mar. 2014, p. M3A.5.

[187] T. Koike-Akino, D. Millar, K. Kojima, and K. Parsons, "Eight-Dimensional Modulation for Coherent Optical Communications," in *Proc. 39th Eur. Conf. Opt. Commun. (ECOC)*, London, United Kingdom, Sept. 2013, p. Tu.3.C.3.

[188] D. S. Millar, T. Koike-Akino, S. O. Arik, K. Kojima, K. Parsons, T. Yoshida, and T. Sugihara, "High-dimensional modulation for coherent optical communications systems," *Opt. Express*, vol. 22, no. 7, pp. 8798–8812, Apr 2014.

[189] P. Johannisson, M. Sjödin, M. Karlsson, H. Wymeersch, E. Agrell, and P. A. Andrekson, "Modified constant modulus algorithm for polarization-switched QPSK," *Opt. Express*, vol. 19, pp. 7734–7741, 2011.

[190] D. Milar and S. Savory, "Blind adaptive equalization of polarization-switched QPSK modulation," *Opt. Express*, vol. 19, pp. 8533–8538, 2011.

[191] J. Renaudier, O. B. Pardo, H. Mardoyan, M. Salsi, P. Tran, E. Dutisseuil, G. Charlet, and S. Bigo, "Experimental comparison of 28gbaud polarization switched- and polarization division multiplexed- qpsk in wdm long-haul transmission system," in *Proc. 37th Eur. Conf. Opt. Commun. (ECOC)*, Geneva, Switzerland, 2011, p. Mo.2.B.3.

[192] M. Sjödin, P. Johannisson, H. Wymeersch, P. A. Andrekson, and M. Karlsson, "Comparison of polarization-switched QPSK and polarization-multiplexed QPSK at 30 Gbit/s," *Opt. Express*, vol. 19, pp. 7839–7846, 2011.

[193] J. Renaudier, P. Serena, A. Bononi, M. Salsi, O. Bertran-Pardo, H. Mardoyan, P. Tran, E. Dutisseuil, G. Charlet, and S. Bigo, "Generation and Detection of 28 Gbaud Polarization Switched-QPSK in WDM Long-Haul Transmission Systems," *J. Lightw. Technol.*, vol. 30, no. 9, pp. 1312–1318, 2012.

[194] S. Alreesh, J. K. Fischer, M. Nölle, and C. Schubert, "Joint-Polarization Carrier Phase Estimation for PS-QPSK Signals," *IEEE Photon. Technol. Lett.*, vol. 24, no. 15, pp. 1282– 1284, Aug 2012.

[195] M. Kuschnerov, D. van den Borne, K. Piyawanno, F. N. Hauske, C. R. S. Fludger, T. Duthel, T. Wuth, J. C. Geyer, C. Schulien, B. Spinnler, E. D. Schmidt, and B. Lankl, "Joint-polarization carrier phase estimation for XPM-limited coherent polarization-multiplexed QPSK transmission with OOK-neighbors," in *Proc. 34th Eur. Conf. Opt. Commun. (ECOC)*, Brussels, Belgium, Sept. 2008, p. Mo.4.D.2.

[196] M. Nölle, J. K. Fischer, L. Molle, C. Schmidt-Langhorst, and C. Schubert, "Influence of Channel Spacing on Ultra Long-Haul WDM Transmission of 8×112 Gb/s PS-QPSK Signals," in *Proc. Opt. Fiber Commun. Conf. (OFC)*, Los Angeles, CA, Mar. 2012, p. OTh3A.4.

[197] F. Vacondio, C. Simonneau, L. Lorcy, J. C. Antona, A. Bononi, and S. Bigo, "Experimental characterization of Gaussian-distributed nonlinear distortions," in *Proc. 37th Eur. Conf. Opt. Commun. (ECOC)*, Geneva, Switzerland, Sept. 2011, p. We.7.B.1.

[198] J. K. Fischer and S. Alreesh, "Phase noise estimation for 6-ary polarization-shift keying quadrature phase-shift keying," Jul. 24 2014, WO Patent App. PCT/EP2013/050,848.

[199] S. Alreesh, J. K. Fischer, P. W. Berenguer, and C. Schubert, "Blind adaptive equalization for 6PolSK-QPSK signals," in *Proc. 39th Eur. Conf. Opt. Commun. (ECOC)*, London, United Kingdom, 2013, p. Mo.4.D.3.

[200] S. Lin and D. J. Costello, *Error Control Coding, Second Edition*. Prentice-Hall, Inc., 2004.

[201] G. Ungerboeck and I. Csajka, “On improving data-link performance by increasing the channel alphabet and introducing sequence coding,” in *Proc. IEEE Int Symp. Information Theory (ISIT)*, Ronneby, Sweden, June 1976, p. 53, Books of Abstracts.

[202] E. Biglieri, D. Divsalar, M. K. Simon, and P. J. McLane, *Introduction to Trellis-Coded Modulation with Applications*, J. Griffin, Ed. Prentice-Hall, Inc., 1991.

[203] A. Viterbi, “Error bounds for convolutional codes and an asymptotically optimum decoding algorithm,” *IEEE Trans. Inf. Theory*, vol. 13, no. 2, pp. 260–269, Apr. 1967.

[204] G. Ungerboeck, “Trellis-coded modulation with redundant signal sets Part I: Introduction,” *IEEE Commun. Mag.*, vol. 25, no. 2, pp. 5–11, February 1987.

[205] T. K. Moon, *“Error Correction Coding: Mathematical Methods and Algorithms”*. Hoboken, NJ: Wiley, 2005.

[206] G. Ungerboeck, “Trellis-coded modulation with redundant signal sets Part II: State of the art,” *IEEE Commun. Mag.*, vol. 25, no. 2, pp. 12–21, February 1987.

[207] A. R. Calderbank and N. J. A. Sloane, “Four-dimensional modulation with an eight-state trellis code,” *AT&T Tech. J.*, vol. 64, pp. 1005–1018, May 1985.

[208] ——, “An eight-dimensional trellis code,” *Proc. IEEE*, vol. 74, no. 5, pp. 757–759, 1986.

[209] L.-F. Wei, “Trellis-coded modulation with multidimensional constellations,” *IEEE Trans. Inf. Theory*, vol. 33, no. 4, pp. 483–501, 1987.

[210] G. D. Forney, L. Brown, M. V. Eyuboglu, and J. L. Moran, “The V.34 high speed modem standard,” *IEEE Commun. Mag.*, vol. 34, no. 12, pp. 28–33, 1996.

[211] International Telecommunication Union, Telecommunication Standardization Sector (ITU-T), recommendation G.993.2, “Very High Speed Digital Subscriber Line Transceivers 2 (VDSL2),” Feb. 2006.

[212] H. Imai and S. Hirakawa, “A new multilevel coding method using error-correcting codes,” *IEEE Trans. Inf. Theory*, vol. 23, no. 3, pp. 371– 377, 1977.

[213] E. Cusack, “Error control codes for QAM signalling,” *Electron Lett.*, vol. 20, no. 2, pp. 62–63, 1984.

[214] S. Sayegh, “A Class of Optimum Block Codes in Signal Space,” *IEEE Trans. Commun.*, vol. 34, no. 10, pp. 1043–1045, Oct 1986.

[215] E. Biglieri, “Parallel demodulation of multidimensional signals,” *IEEE Trans. Commun.*, vol. 40, no. 10, pp. 1581–1587, Oct 1992.

[216] S. Pietrobon, R. Deng, A. Lafanechere, G. Ungerboeck, and J. Costello, D.J., “Trellis-coded multidimensional phase modulation,” *IEEE Trans. Inf. Theory*, vol. 36, no. 1, pp. 63–89, 1990.

[217] C. B. Schlegel and L. C. Pérez, *Trellis and Turbo Coding*. John Wiley & Sons, Inc., 2004, pp. 51–94.

[218] S. Lin, T. Kasami, T. Fujiwara, and M. Fossorier, *Trellises and Trellis-Based Decoding Algorithms for Linear Block Codes*. Boston, MA: Springer US, 1998, pp. 5–22.

[219] V. V. Ginzburg, “Multidimensional Signals for a Continuous Channel,” *Probl. Peredachi Inf.*, vol. 20, p. 28–46, 1984.

[220] S. Pietrobon and J. Costello, D.J., “Trellis coding with multidimensional QAM signal sets,” *IEEE Trans. Inf. Theory*, vol. 39, no. 2, pp. 325–336, Mar. 1993.

[221] L. F. Wei, “Rotationally invariant trellis-coded modulations with multidimensional M-PSK,” *IEEE J. Sel. Areas Commun.*, vol. 7, no. 9, pp. 281–1295, Dec. 1989.

[222] L.-F. Wei, “Rotationally Invariant Convolutional Channel Coding with Expanded Signal Space - Part II: Nonlinear Codes,” *IEEE J. Sel. Areas Commun.*, vol. 2, no. 5, pp. 672–686, Sept. 1984.

[223] C. Berrou, A. Glavieux, and P. Thitimajshima, “Near Shannon limit error-correcting coding and decoding: Turbo-codes,” in *Proc. ICC*, vol. 2, May 1993, pp. 1064–1070.

[224] P. Robertson and T. Wörz, “Bandwidth-efficient turbo trellis-coded modulation using punctured component codes,” *IEEE J. Sel. Areas Commun.*, vol. 16, no. 2, pp. 206–218, Feb 1998.

[225] L. Bahl, J. Cocke, F. Jelinek, and J. Raviv, “Optimal decoding of linear codes for minimizing symbol error rate,” *IEEE Trans. Inf. Theory*, vol. 20, no. 2, pp. 284–287, Mar. 1974.

[226] L. Hanzo, T. H. Liew, and B. L. Yeap, *Turbo Coding, Turbo Equalisation and Space-Time Coding for Transmission over Fading Channels*. New York, USA: Wiley, 2002.

[227] *Digital Video Broadcasting (DVB); Second generation framing structure, channel coding and modulation systems for Broadcasting, Interactive Services, News Gathering and other broadband satellite applications (DVB-S2).*, ETSI EN 302 307 V1.2.1 (2009-08) Std., 2009.

[228] R. Pyndiah, “Near-optimum decoding of product codes: block turbo codes,” *IEEE Trans. Commun.*, vol. 46, no. 8, pp. 1003– 1010, 1998.

[229] T. Tanimura, Y. Koganei, H. Nakashima, T. Hoshida, and J. C. Rasmussen, “Soft decision forward error correction over nonlinear transmission of 1-Tb/s superchannel,” in *Proc. 40th Eur. Conf. Opt. Commun. (ECOC)*, Sept 2014, p. Th.1.3.4.

[230] E. L. T. de Gabory, T. Nakamura, H. Noguchi, W. Maeda, S. Fujita, J. Abe, and K. Fukuchi, “Experimental Demonstration of the Improvement of System Sensitivity Using Multiple State Trellis Coded Optical Modulation with QPSK and 16QAM Constellations,” in *Proc. Opt. Fiber Commun. Conf. (OFC)*, Los Angeles, CA, 2015, p. W3K.3.

[231] S. Ishimura and K. Kikuchi, “Eight-state trellis-coded optical modulation with signal constellations of four-dimensional M-ary quadrature-amplitude modulation,” *Opt. Express*, vol. 23, no. 5, pp. 6692–6704, Mar 2015.

[232] E. Sillekens, R. G. H. van Uden, J. J. A. van Weerdenburg, M. Kuschnerov, H. de Waardt, A. M. J. Koonen, and C. M. Okonkwo, “Experimental demonstration of 8 state Turbo Trellis coded modulation employing 8 phase shift keying,” in *Proc. 41th Eur. Conf. Opt. Commun. (ECOC)*, Valencia, Spain, Sep. 2015, p. Tu.3.4.1.

[233] Bhoja, V. Parthasarathy, and Z. Wang, “FEC Codes for 400 Gbps 802.3bs,” *IEEE P802.3bs 400 Gb/s Ethernet Task Force, San Antonio*, 2014.

[234] *ITU-T recommendation G.694.1: Spectral grids for WDM applications: DWDM frequency grid*, Int. Telecommun. Union Std., Feb. 2012.

[235] P. W. Berenguer, M. Nölle, L. Molle, T. Raman, A. Napoli, C. Schubert, and J. K. Fischer, “Nonlinear Digital Pre-distortion of Transmitter Components,” *J. Lightw. Technol.*, vol. 34, no. 8, pp. 1739–1745, Apr. 2016.

[236] E. Agrell, A. Alvarado, G. Durisi, and M. Karlsson, “Capacity of a Nonlinear Optical Channel With Finite Memory,” *J. Lightw. Technol.*, vol. 32, no. 16, pp. 2862–2876, Aug. 2014.

[237] I. B. Djordjevic, *Codes on Graphs, Coded Modulation and Compensation of Nonlinear Impairments by Turbo Equalization*, 1st ed. Springer-Verlag New York, 2011, vol. 7, ch. 12.

[238] L. Beygi, E. Agrell, and M. Karlsson, “Adaptive coded modulation for nonlinear fiber-optical channels,” in *IEEE Globecom Workshops*, Dec, 2012, pp. 331–335.

[239] A. D. Shiner, M. Reimer, A. Borowiec, S. O. Gharan, J. Gaudette, P. Mehta, D. Charlton, K. Roberts, and M. O’Sullivan, “Demonstration of an 8-dimensional modulation format with

reduced inter-channel nonlinearities in a polarization multiplexed coherent system," *Opt. Express*, vol. 22, no. 17, pp. 20366–20374, Aug 2014.

[240] L. Beygi, E. Agrell, P. Johannisson, and M. Karlsson, "A Novel Multilevel Coded Modulation Scheme for Fiber Optical Channel with Nonlinear Phase Noise," in *IEEE Global Commun. Conf.*, Miami, Dec 2010.

[241] P. J. Winzer and G. J. Foschini, "MIMO capacities and outage probabilities in spatially multiplexed optical transport systems," *Opt. Express*, vol. 19, no. 17, pp. 16680–16696, Aug 2011.

A Acronyms

6PolSK-QPSK	6-ary Polarization-Shift keying Quadrature Phase-Shift Keying
ACS	Add-Compare-Select
ASE	Amplified Spontaneous Emission
ASIC	Application-Specific Integrated Circuit
AWGN	Additive White Gaussian Noise
b2b	back-to-back
BCH	Bose-Chaudhuri-Hocquenghem
BD	Balanced Detector
BER	Bit Error Rate
CMA	Constant Modulus Algorithm
CPE	Carrie Phase Estimation
Cycle Slip	CS
DA	Data-aided
DFE	Decision Feedback Equalizer
DSL	digital subscriber line
DSP	Digital Signal Processing
ECL	External Cavity Laser
EDFA	Erbium-doped fiber amplifier
EON	Elastic Optical Network
FDE	Frequency Domain Equalizer
FOE	Frequency Offset Estimation
FPGA	Field-Programmable Gate Array
FWM	Four-Wave Mixing
ID	Iterative Demapping
IF	Intermediate Frequency
IP	Intellectual Property
LDPC	Low Density Parity Check
MLC	Multilevel coding
MLD	Maximum Likelihood Decision
MSD	Minimum subset distance
MSSD	Minimum squared subset distance
MZM	Mach–Zehnder modulator
NLC	Nonlinearity Compensation
NWDM	Nyquist Wavelength Division Multiplexing
OH	overhead
OSNR	Optical signal-to Noise Ratio
PBS	Polarization Beam Splitters
PDL	Polarization-Dependent Loss
PDM	Polarization Division Multiplexing

PolSK	Polarization Shift Keying
QAM	Quadrature Amplitude Modulation
QPSK	Quadrature Phase-Shift Keying
RS	Reed-Solomon
SBS	Stimulated Brillouin Scattering
SDM	Space Division Multiplexing
SDON	software defined optical networks
SE	Spectral Efficiency
SER	Symbol Error Rate
SIHO	Soft-Input Hard-Output
SISO	Soft-Input Sard-Output
SNR	Signal-to-Noise Ratio
SOP	State Of Polarization
SPM	Self-Phase Modulation
SRC	Stimulated Raman Scattering
SSMF	Standard Single Mode Fiber
TDE	Time Domain Equalizer
TPC	Turbo Product Code
WDM	Wavelength Division Multiplexing
XPM	Cross-Phase Modulation

B Publications of the author

Peer-reviewed Journal Publications

[1] **S. Alreesh**, C. Schmidt-Langhorst, R. Emmerich, P. W. Berenguer, C. Schubert, and J. K. Fischer, "Four-Dimensional Trellis Coded Modulation for Flexible Optical Communications," *J. Lightw. Technol.*, vol. 35, no. 2, pp. 152-158, Jan. 2017.

[2] I. G. Lopez, A. Aimone, **S. Alreesh**, P. Rito, T. Brast, V. Hohns, G. Fiol, M. Gruner, J. K. Fischer, J. Honecker, A. G. Steffan, D. Kissinger, A. C. Ulusoy, and M. Schell, "DAC-free Ultra-Low-Power Dual-Polarization 64-QAM Transmission at 32 GBd with Hybrid InP IQ SEMZM and BiCMOS Drivers Module," *J. Lightw. Technol.*, vol. 35, no. 3, pp. 404-410, Feb. 2017.

[3] I. G. López, A. Aimone, P. Rito, **S. Alreesh**, T. Brast, V. Höhns, G. Fiol, M. Gruner, J. K. Fischer, J. Honecker, A. G. Steffan, M. Schell, A. Awny, A. C. Ulusoy, and D. Kissinger, "High-Speed Ultralow-Power Hybrid Optical Transmitter Module With InP I/Q-SEMZM and BiCMOS Drivers With 4-b Integrated DAC," *IEEE Trans. Microw. Theory Techn.*, vol. 64, no. 12, pp. 4598–4610, Dec 2016.

[4] J. K. Fischer, C. Schmidt-Langhorst, **S. Alreesh**, R. Elschner, F. Frey, P. W. Berenguer, L. Molle, M. Nölle, and C. Schubert, "Generation, Transmission, and Detection of 4-D Set-Partitioning QAM Signals," *J. Lightwave Technol.*, vol. 33, no. 7, pp. 1445–1451, Apr 2015.

[5] **S. Alreesh**, C. Schmidt-Langhorst, F. Frey, P. W. Berenguer, C. Schubert, and J. K. Fischer, "Transmission Performance of 4D 128SP-QAM With Forward Error Correction Coding," *IEEE Photon. Technol. Lett.*, vol. 27, no. 7, pp. 744–747, Apr. 2015.

[6] J. K. Fischer, **S. Alreesh**, R. Elschner, F. Frey, M. Nölle, C. Schmidt-Langhorst, and C. Schubert, "Bandwidth-Variable Transceivers based on Four-Dimensional Modulation Formats," *J. Lightw. Technol.*, vol. 32, pp. 2886–2895, Aug. 2014.

[7] **S. Alreesh**, J. K. Fischer, M. Nölle, and C. Schubert, "Joint-Polarization Carrier Phase Estimation for PS-QPSK Signals," *IEEE Photon. Technol. Lett.*, vol. 24, no. 15, pp. 1282– 1284, Aug 2012.

[8] J. K. Fischer, **S. Alreesh**, R. Elschner, F. Frey, C. Meuer, L. Molle, C. Schmidt-Langhorst, T. Tanimura, and C. Schubert, "Experimental Investigation of 126-Gb/s 6PolSK-QPSK signals," *Opt. Express*, vol. 20, no. 26, pp. B232–B237, Dec 2012.

Peer-reviewed Conference Papers

[9] **S. Alreesh**, C. Schmidt-Langhorst, R. Emmerich, P. W. Berenguer, C. Schubert, and J. K. Fischer, "Four-Dimensional Trellis Coded Modulation for Flexible Optical Transponders," in *Proc. 42th Eur. Conf. Opt. Commun. (ECOC)*, Düsseldorf, Germany, 2016, p. W.1.C.4.

[10] **S. Alreesh**, C. Schmidt-Langhorst, R. Elschner, F. Frey, P. W. Berenguer, L. Molle, M. Noelle, C. Schubert, and J. K. Fischer, "Transmission of 2048SP-QAM Nyquist-WDM signals," in *Proc. 16. ITG-Fachtagung Photonische Netze*, Leipzig, May 2015, pp. 88–91.

[11] T. A. Eriksson, **S. Alreesh**, C. Schmidt-Langhorst, F. Frey, P. W. Berenguer, C. Schubert, J. K. Fischer, P. A. Andrekson, M. Karlsson, and E. Agrell, "Experimental investigation of a four-dimensional 256-ary lattice-based modulation format," in *Proc. Opt. Fiber Commun. Conf. (OFC)*, Los Angeles, CA, Mar. 2015, p. W4K.3.

[12] J. K. Fischer, C. Schmidt-Langhorst, **S. Alreesh**, R. Elschner, F. Frey, P. W. Berenguer, L. Molle, M. Nölle, and C. Schubert, "Transmission of 512SP-QAM Nyquist-WDM signals," in *Proc. 40th Eur. Conf. Opt. Commun. (ECOC)*, Sept. 2014, p. Tu.3.3.2.

[13] J. K. Fischer, **S. Alreesh**, R. Elschner, F. Frey, M. Nölle and C. Schubert, "Bandwidth-variable transceivers based on 4D modulation formats for future flexible networks," *Proc. 39th Eur. Conf. Opt. Commun. (ECOC)*, London, United Kingdom, 2013, p. Tu.3.C.1.

[14] T. Tanimura, **S. Alreesh**, J. K. Fischer, C. Schmidt-Langhorst, F. Frey, C. Meuer, R. Elschner, L. Molle, and C. Schubert, "Nonlinear transmission of 6PolSK-QPSK signals using coded modulation and digital back propagation," in *Proc. Opt. Fiber Commun. Conf. (OFC)*, Anaheim, CA, 2013, p. OTu3B.3.

[15] J. Fischer, **S. Alreesh**, T. Tanimura, R. Elschner, F. Frey, C. Meuer, L. Molle, C. Schmidt-Langhorst, and C. Schubert, "Four-dimensional coded modulation: 6POLSK-QPSK," in *Proc. 14. ITG-Fachtagung Photonische Netze*, Leipzig, Germany, May 2013.

[16] R. Elschner, F. Frey, C. Meuer, J. K. Fischer, **S. Alreesh**, C. Schmidt-Langhorst, L. Molle, T. Tanimura, and C. Schubert, "Data-Aided Digital Signal Processing for Format-Flexible Transponders," in *Proc. 14. ITG-Fachtagung Photonische Netze*, Leipzig, Germany, May 2013.

[17] **S. Alreesh**, J. K. Fischer, P. W. Berenguer, and C. Schubert, "Blind adaptive equalization for 6PolSK-QPSK signals," in *Proc. 39th Eur. Conf. Opt. Commun. (ECOC)*, London, United Kingdom, 2013, p. Mo.4.D.3.

[18] J. K. Fischer, **S. Alreesh**, R. Elschner, F. Frey, C. Meuer, L. Molle, C. Schmidt-Langhorst, T. Tanimura, and C. Schubert, "Experimental Investigation of 126-Gb/s 6PolSK-QPSK Signals," in *Proc. 38th Eur. Conf. Opt. Commun. (ECOC)*, 2012, p. We.1.C.4.

Post-deadline Papers

[19] A. Aimone, I. G. Lopez, **S. Alreesh**, P. Rito, T. Brast, V. Höhns, G. Fiol, M. Gruner, J. K. Fischer, J. Honecker, A. G. Steffan, D. Kissinger, A. C. Ulusoy, and M. Schell, "DAC-free ultra-low-power dual-polarization 64-QAM transmission with InP IQ segmented MZM module," in *Proc. Opt. Fiber Commun. Conf. (OFC)*, Anaheim, CA, Mar. 2016, p. Th5C.6.

[20] T. Richter, C. Schmidt-Langhorst, R. Elschner, L. Molle, **S. Alreesh,** T. Kato, T. Tanimura, S. Watanabe, J. K. Fischer, and C. Schubert, "Distributed 1-Tb/s all-optical aggregation capacity in 125-GHz optical bandwidth by frequency conversion in fiber," in *Proc. 41th Eur. Conf. Opt. Commun. (ECOC)*, Valencia, Spain, 2015, p. PDP.2.5.

Patent

[21] J. K. Fischer and **S. Alreesh**, "Phase noise estimation for 6-ary polarization-shift keying quadrature phase-shift keying," Jul. 24 2014, WO Patent App. PCT/EP2013/050,848.